

12-2016

# Artificial Quantum Many-Body States in Complex Oxide Heterostructures at Two-Dimensional Limit

Xiaoran Liu

*University of Arkansas, Fayetteville*

Follow this and additional works at: <http://scholarworks.uark.edu/etd>



Part of the [Condensed Matter Physics Commons](#)

---

## Recommended Citation

Liu, Xiaoran, "Artificial Quantum Many-Body States in Complex Oxide Heterostructures at Two-Dimensional Limit" (2016). *Theses and Dissertations*. 1767.

<http://scholarworks.uark.edu/etd/1767>

This Dissertation is brought to you for free and open access by ScholarWorks@UARK. It has been accepted for inclusion in Theses and Dissertations by an authorized administrator of ScholarWorks@UARK. For more information, please contact [scholar@uark.edu](mailto:scholar@uark.edu), [ccmiddle@uark.edu](mailto:ccmiddle@uark.edu).

Artificial Quantum Many-Body States in Complex Oxide Heterostructures at  
Two-Dimensional Limit

A dissertation submitted in partial fulfillment  
of the requirements for the degree of  
Doctor of Philosophy in Physics

by

Xiaoran Liu  
Nanjing University  
Bachelor of Science in Materials Science and Engineering, 2011  
University of Arkansas  
Master of Science in Physics, 2013

December 2016  
University of Arkansas

This dissertation is approved for recommendation to the Graduate Council.

---

Prof. Jak Chakhalian  
Dissertation Director

---

Prof. Laurent Bellaiche  
Committee Member

---

Prof. Surendra P. Singh  
Committee Member

---

Prof. Huaxiang Fu  
Committee Member

---

Prof. Ryan Tian  
Committee Member

## ABSTRACT

As the representative family of complex oxides, transition metal oxides, where the lattice, charge, orbital and spin degrees of freedom are tightly coupled, have been at the forefront of condensed matter physics for decades. With the advancement of state-of-the-art heteroepitaxial deposition techniques, it has been recognized that combining these oxides on the atomic scale, the interfacial region offers great opportunities to discover emergent phenomena and tune materials' functionality. However, there still lacks general guiding principles for experimentalists, following which one can design and fabricate artificial systems on demand. The main theme of this dissertation is to devise and propose some basic rules for heterostructure engineering.

Towards this goal, I first report the growth of high quality  $\text{YTiO}_3/\text{CaTiO}_3$  superlattices by pulsed laser deposition. Electrical transport measurements reveal that a novel, non- $\text{SrTiO}_3$  based two-dimensional electron gas system has formed at the interface. What is more, these studies add solid evidences that interface engineering via charge modulation is an effective approach to realizing exotic many-body phenomena.

Secondly, a new concept, denoted as "geometrical lattice engineering" is proposed with pioneering experimental efforts. Aiming at designing magnetically frustrated systems, (111)-oriented  $\text{CoCr}_2\text{O}_4$  thin films and  $\text{CoCr}_2\text{O}_4/\text{Al}_2\text{O}_3$  heterostructures have been fabricated for the first time. Comprehensive structural and electronic characterizations reveal that no disorder in the cation distribution or multivalency issue is present. As a result, unique quasi-two dimensional geometrically frustrated lattices composed of alternating kagomé and triangular lattices, are naturally established via this topological approach.

These  $\text{CoCr}_2\text{O}_4/\text{Al}_2\text{O}_3$  heterostructures have been found to exhibit remarkably different behaviors from the bulk compounds. Towards the two dimensional limit, the ground state of the ultrathin superlattices transforms from the bulk-like nonlinear ferrimagnetic phase, into an emergent collinear ferrimagnetic phase, and finally into an exotic magnetically disordered phase with an extensively large frustration parameter, which is a hallmark of quantum spin liquid. These findings corroborate geometrical lattice engineering has excellent potential in achieving novel electronic, magnetic, and topological phases.

## ACKNOWLEDGEMENTS

The journey finally comes to the end. I must express my sincere acknowledgements to all my colleagues, collaborators, and advisors. Without your great assistance, I can never reach this point.

First, I would like to acknowledge the team members in laboratory of artificial quantum materials at the University of Arkansas. Derek Meyers kindly trained me on the operations of all the apparatus when I just joined in the group. His sense of humor and sense of responsibility always encourage me and help me to pass the initial time fluently. This is the same with Michael Kareev, who is sophisticated in sample fabrications, sharing with me a lot of his precious experiences. Likewise, thanks to Srimanta Middey, his miscellaneous background sometimes offers another interesting way of thinking. Moreover, I would like to thank Yanwei Cao, a very talented person and an order brother to me. Discussing and “arguing” with him usually sparkled with new ideas. I will never forget the time that we did experiments together, ran beam times together and went to conferences together. Also, I want to acknowledge Jian Liu and Ben Gray for their constructive suggestions about how to enjoy the Ph.D. life.

Besides, I would like to thank the beamline scientists for their professional guidance when performing measurements at the national laboratories. This includes Dr. John W. Freeland, Dr. Daniel Haskel, Dr. Yongseong Choi, Dr. Philip Ryan, and Dr. Jong-woo Kim at Argonne National Laboratory; Dr. Elke Arenholz, Dr. Padraic Shafer, and Dr. Alpha N'Diaye at Lawrence Berkeley National Laboratory; Dr. Brian Kirby at National Institute of Standards and Technology. Without the assistance from these brilliant faculties, this dissertation cannot be completed. In addition, allow me to express special acknowledgements to Dr. Daniel Khomskii, Dr. Gregory Fiete, Dr. Dipankar D. Sarma and Dr. Priya Mahadevan for their beneficial comments on my research projects.

I also would like to acknowledge the funding support from Department of Energy for a two-year research assistantship, as well as the Raymond H. Hughes Graduate Fellowship from the University of Arkansas.

In the end, I would like to express my sincerest thanks to my advisor, Dr. Jak Chakhalian. Because of him, this five years journey is full of passion and expectation. He is extremely enthusiastic and knowledgeable on researches, which motivates me to catch up on his train. In the mean while, he is always generous to offer helps and create opportunities for me. It

is my fortune and honor to be his graduate student. These precious memories will always stay in my heart and last for the rest of my life.

## DEDICATION

To my greatest parents for their eternal love and endless support

## TABLE OF CONTENTS

1	Introduction . . . . .	1
1.1	Transition metal oxides . . . . .	1
1.1.1	Crystal structures . . . . .	1
1.1.2	Electronic properties . . . . .	6
1.1.3	Magnetic interactions . . . . .	17
1.2	Interface engineering . . . . .	19
1.3	Geometrical lattice engineering . . . . .	22
2	Experimental techniques . . . . .	25
2.1	Epitaxial thin film growth . . . . .	25
2.1.1	Pulsed laser deposition . . . . .	25
2.1.2	Reflection high energy electron diffraction . . . . .	30
2.2	High-resolution X-ray diffraction . . . . .	32
2.3	Resonant X-ray absorption spectroscopy . . . . .	37
2.3.1	Basic principles . . . . .	38
2.3.2	Polarization dependence . . . . .	40
2.3.3	Sum rules . . . . .	42
2.3.4	Synchrotron radiation . . . . .	43
2.4	Polarized neutron reflectometry . . . . .	45
2.4.1	Theory of neutron scattering in reflection geometry . . . . .	45
2.4.2	Instrumentation . . . . .	46
3	Metallic interface in non-SrTiO <sub>3</sub> based titanate superlattice . . . . .	49
3.1	Introduction . . . . .	49
3.2	Experiment . . . . .	51
3.3	Results and Discussions . . . . .	52
3.4	Summary . . . . .	57
4	Epitaxial growth of (111)-oriented spinel oxide thin films and heterostructures . . . . .	58
4.1	Introduction . . . . .	58
4.2	Growth and characterizations of (111) CoCr <sub>2</sub> O <sub>4</sub> thin films . . . . .	60
4.3	Establishment of (111) CoCr <sub>2</sub> O <sub>4</sub> /Al <sub>2</sub> O <sub>3</sub> superlattices . . . . .	65
4.4	Summary . . . . .	70
5	Emergent magnetism of quasi-two-dimensional frustrated lattices by geometric design . . . . .	72
5.1	Introduction . . . . .	72
5.2	Experimental methods . . . . .	73
5.2.1	Sample fabrication . . . . .	73
5.2.2	Polarized X-ray absorption and scattering characterizations . . . . .	74
5.2.3	Polarized neutron reflectometry . . . . .	74
5.3	Results and discussions . . . . .	74
5.3.1	Structure and local environment . . . . .	74

5.3.2	Overall magnetization characterizations . . . . .	75
5.3.3	Temperature-dependent XMCD and hysteresis loops . . . . .	76
5.3.4	XMCD fitting . . . . .	78
5.3.5	Discussion on the magnetic ground state . . . . .	82
5.3.6	Phase diagram . . . . .	83
5.4	Summary . . . . .	84
6	Conclusions and future prospects . . . . .	86
6.1	Conclusions . . . . .	86
6.2	Future prospects . . . . .	87
	Bibliography . . . . .	91



## LIST OF FIGURES

Figure 1.1:	Periodic table of elements. Besides oxygen, TMOs contain at least one of the elements in the black box. . . . .	2
Figure 1.2:	Coordination number and type of polyhedral geometry determined by the cation-anion radius ratio in TMOs. The central cation is displayed with small blue cycle while oxygen ions are with big red cycle. The black rod between each cation and oxygen represents the ionic bonding.	3
Figure 1.3:	Shapes of the $d$ orbitals. The notion of $x$ , $y$ , and $z$ refer to the wave-function variables written in the Cartesian coordinate system. . . . .	7
Figure 1.4:	Energy splitting of the $d$ orbitals under different crystal field symmetry. The notions of $e_g$ , $t_{2g}$ , $t_2$ , and $e$ are defined following the notions in group theory. . . . .	8
Figure 1.5:	(a) High-spin configuration and low-spin configuration in a $d^4$ system. (b) Jahn-Teller effect in systems with one $e_g$ electron. . . . .	10
Figure 1.6:	(a) - (e) Evolution of the electronic energy levels of TMOs in ionic model. O and M refer to oxygen and transition metal ion, respectively. Figure is adapted from Ref. [1]. . . . .	11
Figure 1.7:	$p$ - $d$ hybridization and molecular orbitals of a $MO_6$ cluster. M refers to the central transition metal ion in an octahedron of six oxygens. . . . .	13
Figure 1.8:	Schematic illustration of the $d$ band in Hubbard model. For a half-filling band, the electron correlation (Hubbard $U$ ) is able to open a gap when its strength reaches the critical point. The two new split bands are called upper Hubbard band (empty) and lower Hubbard band (occupied). Figure adapted from [2]. . . . .	14
Figure 1.9:	(a) Energy level diagram of the Mott-Hubbard insulator. In this case, the gap $E_g$ is determined by the correlation Hubbard $U$ . (b) Energy level diagram of the charge-transfer insulator. In this case, the gap $E_g$ is determined by the charge-transfer $\Delta$ . (c) Zaanen-Sawatzky-Allen phase diagram. Note, $U$ and $\Delta$ represent the electron-electron correlation and charge-transfer energy, respectively. $t$ is the electron hopping strength. . . . .	15
Figure 1.10:	(a) Superexchange interaction paradigm in Ni ( $3d^7$ ) configuration. (b) Double exchange interaction paradigm in mixed valency Mn <sup>3+/4+</sup> ( $3d^4/3d^3$ ) configuration. . . . .	18
Figure 1.11:	Mismatches at complex oxide interfaces, reproduced from Ref. [3]. . . . .	20
Figure 1.12:	Schematic illustration of the idea about geometrical lattice engineering, which has three control parameters named as orientation, stacking, and superlattice throughout its entire process. . . . .	23
Figure 2.1:	(a) A schematic of the environment inside a PLD main chamber. (b) Photograph of the PLD system used in this dissertation. . . . .	26
Figure 2.2:	Various growth modes in PLD. (a) Step-flow mode; (b) Layer-by-layer mode; (c) Stranski-Krastanov mode; (d) Volmer-Weber mode. . . . .	28

Figure 2.3:	(a) Geometrical representation of Ewald sphere and Laue condition. (b) Schematic of RHEED and the normal pattern exhibited on a camera screen. (c) A typical RHEED image of (001) SrTiO <sub>3</sub> substrate taken from our machine. . . . .	30
Figure 2.4:	Schematic of high-resolution X-ray diffractometer in triple-axis geometry. The sample cradle has six motorized movements $x, y, z, \omega, \Phi, \Psi$ , and the detector has another independent movement $2\theta$ . $\omega$ is the angle between incident beam and sample surface; $2\theta$ is the angle between incident and diffracted beams; $\Psi$ is the sample tilt angle; $\Phi$ is the azimuthal rotation angle around surface normal. The lines drawn in red, purple, and green colors in the monochromator represent X-rays with various wavelengths within the incident beam. . . . .	33
Figure 2.5:	Epitaxial strain status in both real and reciprocal space. (a) Tensile strain; (b) Compressive strain. In each case, the relaxed state is expressed on the left panel while the fully strained state is expressed on the right panel. Blue color stands for the substrate and red color stands for the film. . . . .	35
Figure 2.6:	Interpretation of resonant X-ray absorption on the L <sub>2,3</sub> edges. (a) Single-electron picture and (b) Configuration picture. . . . .	37
Figure 2.7:	(a) Illustration of X-ray magnetic circular dichroism at the L <sub>2,3</sub> edges of a 3d transition metal compound. (b) Polarization dependence of the transition probabilities from 2p core states to the spin-up 3d valence states (reproduced from Ref. [4]). The + and - sign refer to the circularly polarized photon with helicity +1 and -1, whereas 0 refers to linearly polarized light. . . . .	41
Figure 2.8:	An example of (a) XAS ( $\mu_+ + \mu_-$ ) and (b) XMCD ( $\mu_+ - \mu_-$ ) spectra of the L edge of Co <sup>2+</sup> ions, together with their integrated curves over energy. The symbols $r, p$ , and $q$ labeled on the figures are the three definite integrals involved in the sum rule expressions. . . . .	42
Figure 2.9:	Sketch of the polarized neutron reflectometry station. The incident monochromatic unpolarized beam is polarized by the first supermirror in transmission mode. The spin flippers can switch the neutron polarization from down to up and vice versa. The second supermirror is used to analyze the polarization state of neutrons after scattering. . . . .	47
Figure 3.1:	Schematic of the YTO/CTO superlattices along the [001] pseudocubic growth direction. The crystal structure at one of the interface is highlighted. . . . .	50
Figure 3.2:	(a) RHEED intensity of the specular reflection as a function of deposition time. (b)–(d) <i>In-situ</i> RHEED patterns of (b) NGO (110) substrate, (c) CTO layers and (d) YTO layers. The observed half orders indicated by white arrows are from the orthorhombic (001) reflections. . . . .	51

Figure 3.3:	(a) X-ray reflectivity data of the $[3\text{YTO}/6\text{CTO}]_7$ superlattice. Total thickness of the superlattice calculated according to the Kiessig fringes is about 24 nm. (b) X-ray diffraction $2\theta$ - $\omega$ scan. The film (002) peak and the superlattice satellite peak are labeled on the graph. (c) Reciprocal space mapping around the $(\bar{1}03)$ reflection of the sample. $q_x$ and $q_z$ represent the in-plane and out-of-plane reciprocal lattice vectors, respectively. . . . .	52
Figure 3.4:	Temperature dependence of the resistance of a 3YTO/6CTO superlattice (purple curve) and a 10 nm thick CTO film (black curve). Inset: Sheet resistance of the superlattice vs. temperature in the log scale. Note, temperature is plotted in the log scale to show the absence of any upturn behavior down to 2 K. . . . .	54
Figure 3.5:	Sheet carrier density and mobility of 3YTO/6CTO superlattices as a function of temperature. . . . .	55
Figure 3.6:	Temperature dependence of the sheet resistance of $[\text{mYTO}/\text{nCTO}]_N$ superlattices. m and n represent the pseudocubic unit cell of YTO and CTO, respectively. N stands for the total number of superlattice periodicity. . . . .	56
Figure 4.1:	The conventional unit cell of a normal spinel structure. The corresponding (111) ionic planes are marked on the figure. Note, the A ionic planes only form the triangular planes, while the B ionic planes form both the triangular and the kagome planes. . . . .	59
Figure 4.2:	<i>In-situ</i> RHEED patterns. (a) AIO (0001) substrate. (b)-(d) CCO films grown at different conditions. Note, the incident electron beam of RHEED is fixed along the $[1\bar{1}00]$ direction of the substrate. . . . .	61
Figure 4.3:	(a) X-ray diffraction of CCO thin films and the AIO substrate. Film peaks are labeled on the graph. The sharp peaks belong to the AIO (0001) substrate. Note, the lattice constant obtained is 8.34 Å, which equals the bulk value. (b) X-ray reflectivity data of the same sample. Film thickness calculated according to the Kiessig fringes is about 25 nm. (c) Atomic force microscopy scan of the film surface. . . . .	62
Figure 4.4:	(a)-(b) Core level XPS data (Mg anode) of (a) Cr 2p and (b) Co 2p. (c)-(d) X-ray scattering spectra measured at 15 K and 80 K on the L edge of (c) Cr and (d) Co. . . . .	63
Figure 4.5:	Temperature-dependent magnetization curves of CCO in an applied field of 0.2 T along the $[1\bar{1}00]$ direction of the substrate. The inset is a magnified plot in the vicinity of the second transition point. (b)-(c) XRMS data on the L edge of (b) Co and (c) Cr measured with different applied magnetic fields at 15 K. The color series of red, green, blue and pink stands for field strength of 5 T, 3 T, 1 T and 0.1 T, respectively. (d) Absolute values of Co and Cr XRMS main peaks as a function of applied field and temperature. . . . .	64

Figure 4.6:	(111)-oriented CCO/AlO heterostructures. (a) Epitaxial relationship between CCO and AlO. The hexagonal close packing of AlO oxygen sublattice is labeled as AB in black, while the cubic close packing of CCO oxygen sublattice is labeled as ABC in brown. (b)-(d) RHEED images during the growth of each component. The half-order reflections (marked by pink solid circles) observed on CCO layer is due to the double expansion of the in-plane unit cell. . . . .	66
Figure 4.7:	(a) XRR and (b) XRD curves of 2CCO/nAlO (n = 1 and 2) superlattices with distinct repeat periodicity. Both the thickness fringes and the superlattice satellite peaks are clearly seen on the graphs. The incident wavelength for XRR is $\lambda = 1.5406 \text{ \AA}$ whereas for XRD, $\lambda = 1.4932 \text{ \AA}$ . . . . .	67
Figure 4.8:	Core-level XPS data of the Co and the Cr 2p levels of the samples. The red arrows represent the $\text{Co}^{2+}$ shake-up satellites. The binding-energy separations of the Co 2p peaks, Cr 2p peaks and the energy difference between Co $2p_{3/2}$ and its corresponding satellite peak, are denoted as $\Delta_{\text{Co},2p}$ , $\Delta_{\text{Cr},2p}$ , and $\Delta_{\text{Co},\text{Sat}}$ , respectively on the graph. . . . .	70
Figure 5.1:	Overview of the structural and electronic properties of the superlattices. (a) Schematic of the $(\text{CCO})_n/(\text{AlO})_3$ superlattices. (b) The basic repeating unit (n = 1) of the (111)-oriented CCO, which includes four geometrically frustrated planes: kagome Cr plane (K), triangle Co plane (T), triangle Cr plane (T'), and triangle Co plane (T). Oxygen ions are omitted for clarity. (c) High-angle annular dark-field scanning transmission electron micrograph of a n = 2 sample. The substrate AlO has the $\alpha$ phase whereas the AlO forms the $\gamma$ phase in the film. The enlarged image (right panel) exhibits the interface between the substrate and the film. The relative positions of the oxygen (red dot) layers with respect to the cation layers are shown on the figure. . . . .	73
Figure 5.2:	Co (a) and Cr (b) L edge X-ray absorption spectra of the superlattices with n = 1, 2, and 4. The bulk spectra are plotted as references taken from measurements on CCO powders [5] with normal spinel structure. . . . .	75
Figure 5.3:	(a) PNR data with model fitting on the nCCO/3AlO superlattices. (b) Net magnetization and the nuclear scattering length density (SLD) depth profiles of the superlattices. Data was recored at 10 K with 0.7 T in-plane external field. . . . .	76
Figure 5.4:	Temperature dependence of magnetization of both the nCCO/3AlO superlattices and the substrate. The measurements were performed using the Superconducting Quantum Interference Devices (SQUID) from quantum design. . . . .	77

Figure 5.5:	(a) and (b) XMCD spectra on the L edge of Co and Cr at 15 K, respectively. (c) and (d) Temperature dependence of the XMCD $L_3$ intensity for Co and Cr, respectively. Measurements were recorded during the warming up process, after field-cooling the samples in a 0.1 T field from room temperature to 10 K. The onset of the para- to ferri-magnetic transition temperature is $\sim 70$ K for $n = 4$ and $\sim 50$ K for $n = 2$ samples. The insets show the results of a 50 nm thick CCO films with (111) orientation, indicating bulk-like behaviors with an onset of the transition temperature at $\sim 97$ K. . . . .	78
Figure 5.6:	Magnetic hysteresis loops of the XMCD $L_3$ intensity for Co (a) and Cr (b), respectively. For all the superlattices, the scans were performed by sweeping the external magnetic field up to 0.5 T after zero-field-cooling from room temperature to 15 K. . . . .	79
Figure 5.7:	Brillouin function fittings on the field-dependent XMCD data of (a) Co and (b) Cr at 15 K (below their corresponding transition temperatures) for $n = 2$ (circle) and $n = 4$ (square) samples. The Brillouin function is modified based on a two-sublattice collinear ferrimagnetic model [6, 7]. . . . .	81
Figure 5.8:	Curie-Weiss fitting on the temperature-dependent net XMCD for $n = 1$ sample. The net XMCD data is obtained by summing the individual signal of Co and Cr XMCD together. When adding the signals, the sign of Co is denoted as positive (along the external field) whereas it is negative for Cr (opposite to the external field). The fitted Curie-Weiss temperature $\Theta_{CW}$ is $\sim -142$ K. Fitting was performed using data in the higher temperature region to avoid deviation induced by the formation of short-range orderings at lower temperature. . . . .	82
Figure 5.9:	Phase diagram as a function of frustration parameter. Definition of the symbols: PM — paramagnet, SL — spin liquid, cFiM — collinear ferrimagnet, ncFiM — non-collinear ferrimagnet, AFM — antiferromagnet, QSL — quantum spin liquid. The dotted line crossing the circle points represents the fitted Curie-Weiss temperature $\Theta_{CW}$ . Data for $M\text{Cr}_2\text{O}_4$ with different A sites are taken from literatures ( $M = \text{Cu}$ [8], $\text{Mn}$ [9], $\text{Fe}$ [10], $\text{Co}$ [11], $\text{Ni}$ [8, 12], $\text{Cd}$ [13], $\text{Zn}$ [13], $\text{Mg}$ [13]). Data for the superlattices with $n = 1, 2$ and $4$ are displayed in diamond. The red arrow on the top represents the evolution of the frustration effect in (111)-oriented CCO towards the two-dimensional limit. Experimental results of possible QSL candidates with various types of lattice are plotted for comparison. ( $\text{EtMe}_3\text{Sb}[\text{Pd}(\text{admit})_2]_2$ [14] and $\kappa - \text{H}_3(\text{Cat-EDT-TTF})_2$ [15] with triangle lattice; $\text{Na}_4\text{Ir}_3\text{O}_8$ [16] with hyperkagome lattice; $\text{BaCu}_3\text{V}_2\text{O}_8(\text{OH})_2$ [17] and $\text{ZnCu}_3(\text{OH})_6\text{Cl}_2$ [18] with kagome lattice) . . . . .	85
Figure 6.1:	(a) - (f) Temperature dependence of sheet resistance of ATO/RTO interfaces ( $A = \text{Ca}, \text{Sr}, \text{Ba}$ ; $R = \text{La}, \text{Y}$ ). . . . .	88

Figure 6.2: Summary and outlook on GLE. The upper panel displays other possible routines to topological phase and frustrated magnetism by applying pure GLE. The bottom panel presents the combination of GLE with IE or SE to establish new systems with intriguing physics such as quasi-particle excitation and emergent phenomena. . . . . 89

## LIST OF TABLES

Table 1.1:	A few structural families of TMOs. M, A and B refer to the transition metal ions in binary and ternary compounds. . . . .	4
Table 1.2:	Tolerance factor and perovskite crystal structures. . . . .	5
Table 3.1:	Lattice parameters of bulk CTO, YTO and NGO. The $a$ , $b$ and $c$ represent the values of the orthorhombic unit cell while the $a_c$ , $b_c$ and $c_c$ stand for the pseudocubic unit cell. . . . .	50
Table 4.1:	Fitting parameters of the reflectivity curves of CCO/AIO superlattices. . . . .	68

## Chapter 1

### Introduction

In this chapter, a brief introduction will be given on the basics of structural, electronic, and magnetic properties of transition metal oxides, which serve as the fundamental knowledge throughout this dissertation. Secondly, the idea of interface engineering will be described in a broad scope, showing the unique roles that complex oxide interfaces play in exploring and tuning intriguing phenomena in condensed matter physics. In the end, the general principles and the control parameters of a new designer concept, namely, geometrical lattice engineering, will be discussed.

#### 1.1 Transition metal oxides

As the prototypical family of complex oxides, transition metal oxides (TMOs) are a class of materials which exhibit extraordinarily fruitful physical and chemical features. In these compounds, besides oxygen, the central element belongs to the three *d*-series in the periodic table, as shown in Fig. 1.1, normally known as the transition metal elements. In general, it is the variation of the outmost *d* shell configuration of these elements that gives rise to a great complexity in the crystal structures, electronic properties, and magnetic interactions in TMOs. For a comprehensive review of this field, there are a few representative references [1, 2, 4, 6, 19, 20].

##### 1.1.1 Crystal structures

TMOs can have numerous types of structures, covering all of the seven crystal systems. Although the most rigorous language of determining a crystal structure is by identifying its conventional unit cell and the corresponding space group, going over the entire 230 space groups is certainly not the purpose of this dissertation. Alternatively, since TMOs are predominately regarded as ionic crystals, the driving force of stabilizing a certain structure is the lattice energy: namely, for an ion *i* located in a lattice, it experiences an overall electrostatic potential from the other ions (both cations and anions), which is the so-called




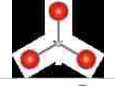
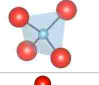
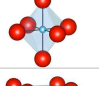
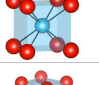
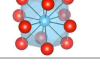
Group→	1	2	3	4	5	6	7	8	9	10	11	12	13	14	15	16	17	18
↓Period																		
1	1 H																	2 He
2	3 Li	4 Be											5 B	6 C	7 N	8 O	9 F	10 Ne
3	11 Na	12 Mg											13 Al	14 Si	15 P	16 S	17 Cl	18 Ar
4	19 K	20 Ca	21 Sc	22 Ti	23 V	24 Cr	25 Mn	26 Fe	27 Co	28 Ni	29 Cu	30 Zn	31 Ga	32 Ge	33 As	34 Se	35 Br	36 Kr
5	37 Rb	38 Sr	39 Y	40 Zr	41 Nb	42 Mo	43 Tc	44 Ru	45 Rh	46 Pd	47 Ag	48 Cd	49 In	50 Sn	51 Sb	52 Te	53 I	54 Xe
6	55 Cs	56 Ba	* 71 Lu	72 Hf	73 Ta	74 W	75 Re	76 Os	77 Ir	78 Pt	79 Au	80 Hg	81 Tl	82 Pb	83 Bi	84 Po	85 At	86 Rn
7	87 Fr	88 Ra	* 103 Lr	104 Rf	105 Db	106 Sg	107 Bh	108 Hs	109 Mt	110 Ds	111 Rg	112 Cn	113 Uut	114 Fl	115 Uup	116 Lv	117 Uus	118 Uuo
			* 57 La	58 Ce	59 Pr	60 Nd	61 Pm	62 Sm	63 Eu	64 Gd	65 Tb	66 Dy	67 Ho	68 Er	69 Tm	70 Yb		
			* 89 Ac	90 Th	91 Pa	92 U	93 Np	94 Pu	95 Am	96 Cm	97 Bk	98 Cf	99 Es	100 Fm	101 Md	102 No		

**Figure 1.1:** Periodic table of elements. Besides oxygen, TMOs contain at least one of the elements in the black box.

“Madelung potential  $V_i$ ”,

$$V_i = \frac{1}{4\pi\epsilon_0} \sum_{i \neq j} \frac{Q_j}{r_{ij}} \quad (1.1)$$

where  $Q_j$  is the net charges of the  $j^{\text{th}}$  ion and  $r_{ij}$  is the ionic distance between  $i$  and  $j$  ions. The associated electrostatic energy of ion  $i$  is the product of its net charges with its Madelung potential. And the summation over all the ions will give rise to the magnitude of the lattice energy. Broadly speaking, the estimation of the minimal value of the lattice energy is the object of structure determination. On the one hand, since the Coulomb interaction between cation and anion is attractive, it is natural to assume that the lattice energy will be dramatically decreased when a cation is surrounded by as many anions as possible. But on the other hand, as more anions are accumulated near one cation, the repulsive interaction between anions will reversely increase the lattice energy. Moreover, if the anions are packed such that the cation is rattling inside the void formed by the anions, this event will also increase the amount of lattice energy. As a result, in order to reach a balance between these competing effects and rationalize the ionic crystal structure, Li-

Radius Ratio ( $r_C/r_A$ )	Coordination number	Type of geometry	
< 0.155	2	Linear	
0.155 - 0.225	3	Triangular	
0.225 - 0.414	4	Tetrahedral	
0.414 - 0.732	6	Octahedral	
0.732 - 1.000	8	Cubic	
1.000	12	Cuboctahedral	

**Figure 1.2:** Coordination number and type of polyhedral geometry determined by the cation-anion radius ratio in TMOs. The central cation is displayed with small blue cycle while oxygen ions are with big red cycle. The black rod between each cation and oxygen represents the ionic bonding.

nus Pauling summarized five famous principles, known as the “Pauling’s rules” [21, 22]. According to these rules, the structure of a complex ionic compound is mainly associated with two factors: the local coordination number (CN) together with the polyhedral geometry of a cation, and the network of the polyhedra spanning all of the crystal. CN and its polyhedral geometry is determined by first Pauling’s rule: the cation-anion radius ratio rule. Fig. 1.2 gives a brief summary on the typical CN values and the corresponding polyhedrons. As in ionic crystals, the radii of the anions are usually larger than the cations’, the radius ratio stops at 1.000. Note, a specific CN and geometry stabilizes only within a certain range of the radius ratio. The lower limit of the range is derived from the closest packing picture of this geometry — anions are considered as rigid spheres and attaching next to each other. If the ratio is smaller than the lower limit, the cation will not be in contact with surrounding anions in that geometry and lower CN is more energetically favored. However, it has to be mentioned that even though the radius ratio offers a rather general criteria for judging the local coordination of a cation, exceptions still remain. Firstly, one coordination number may have different geometries of polyhedron. For instance, in the case of  $CN = 3$ , the central cation can locate either in or out of the plane formed by three oxygen ions. Also for  $CN = 4$ , apart from the tetrahedral environment as shown in Fig. 1.2, a square cubic geometry is also possible. Secondly, some

**Table 1.1:** A few structural families of TMOs. M, A and B refer to the transition metal ions in binary and ternary compounds.

Chemical formula	MO	M <sub>2</sub> O <sub>3</sub>	MO <sub>2</sub>	ABO <sub>3</sub>	AB <sub>2</sub> O <sub>4</sub>	A <sub>2</sub> B <sub>2</sub> O <sub>7</sub>
Structure name	rock-salt	corundum	rutile	perovskite	spinel	pyrochlore
Typical material	NaCl	Al <sub>2</sub> O <sub>3</sub>	TiO <sub>2</sub>	CaTiO <sub>3</sub>	MgAl <sub>2</sub> O <sub>4</sub>	Y <sub>2</sub> Ti <sub>2</sub> O <sub>7</sub>

unusual local coordination will present in materials with rather complex chemical compositions. For example, in some materials, one of the apical oxygen of an octahedron may sit much further than the other or be entirely removed. As a result, the octahedron is strongly deformed and transformed into a pyramid geometry so that the CN = 5 case occurs.

After having knowledge about the local polyhedra of cations, the next step for identifying the crystal structure of TMOs is to understand how these polyhedra are connected. Among dramatically extended materials, three common polyhedral networks have been observed, known as corner-sharing polyhedron, edge-sharing polyhedron, and face-sharing polyhedron. These frameworks construct the long range arrangement of the polyhedra. A very important principle pointed out by Pauling is that the sharing of edges and especially faces by two polyhedra cost more energy than the sharing of corners. This is due to the fact that in edge-sharing and face-sharing modes, the cations are placed in closer proximity, increasing the electrostatic repulsion between them. In addition, for TMOs including multiple kinds of cations, those of high chemical valency and small coordination number tend not to share polyhedron elements, increasing their distance and thus reducing the repulsive interaction between them. Furthermore, there will not be many different types of polyhedra in a crystal because identical repeating blocks, which are most stable, can effectively reduce the energy.

Inspired by these considerations, the structural complexity and variety of TMOs can be simplified by defining some typical templates so that similar structures are categorized accordingly. A few representative structural families are shown in Table 1.1. Conventionally the name and the structure of a class of compounds is represented by selecting a natural mineral belonging to this class discovered in history. In this dissertation, We mainly focus on two categories: the perovskite family and the spinel family. In the following, we shall give some introductions on the features of these two structures.

The perovskite structure is relatively simple and indeed very common for compounds with

**Table 1.2:** Tolerance factor and perovskite crystal structures.

Tolerance factor ( $t$ )	Detail	Structure
$>1$	A is too large or B is too small	Hexagonal
$0.9 - 1$	A and B have ideal size	Cubic
$0.71 - 0.9$	A is slightly bigger than B	Orthorhombic/Rhombohedral
$< 0.71$	A and B have similar size	Other structures

chemical formula  $ABO_3$ . There are basically two alternative combinations of A and B ions in TMOs. If the A site is a rare-earth ion and the B site is the transition metal ion (such as  $RENiO_3$  with  $RE = La$  to  $Yb$ ), the charge state of each ion is  $A^{3+}B^{3+}O_3^{2-}$ . Or if the A site is an alkaline-earth ion (such as  $ATiO_3$  with  $A = Mg$  to  $Ba$ ) and the B site is the transition metal ion, the charge state is given by  $A^{2+}B^{4+}O_3^{2-}$ . No matter which combination, the A ion must be larger than the transition metal B ion and coordinated by 12 oxygen ions. The B ion is surrounded by 6 oxygen ions forming the octahedral coordination and the network of corner-sharing B octahedra stands for the characteristic frame of perovskite. Thus the ideal conventional unit cell of a perovskite is cubic in which the B–O–B bond angle is  $90^\circ$ . However, depending on the relative size of different ions, the real unit cell can deviate from the cubic structure and stabilize in a lower symmetry. To solve this issue, In 1926, Goldschmidt designated an index, the tolerance factor, to estimate the distortions in a perovskite and predict the possible structure [23]:

$$t = \frac{r_A + r_O}{\sqrt{2}(r_B + r_O)} \quad (1.2)$$

in which  $r_A$ ,  $r_B$ , and  $r_O$  are the radii of A, B, and O ions, respectively. Table 1.2 summarizes the detailed relationship between A and B and indicates the most probable structure in every case.

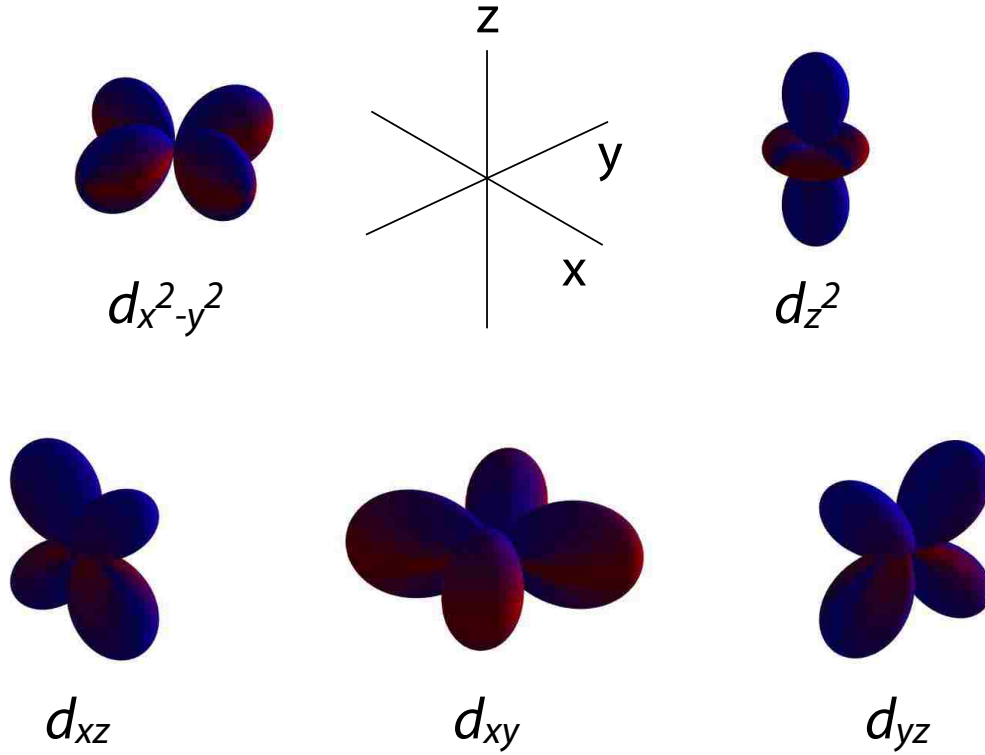
Compared with perovskite, the spinel structure is more complicated. The general chemical formula of the spinel structure can be written as  $A_{1-\delta}B_\delta[A_\delta B_{2-\delta}]O_4$ . When  $\delta = 0$ , it is known as the normal spinel  $AB_2O_4$ , in which all of the A cations are tetrahedrally coordinated, while all B cations are octahedrally coordinated. When  $\delta = 1$ , the chemical formula is  $B[AB]O_4$ , known as the inverse spinel. In this case, the tetrahedral sites are occupied by half of the B cations while the other half of the B cations and all the A cations occupy the octahedral sites. When  $0 < \delta < 1$ , A and B cations mix up in both the tetrahedral and the octahedral sites. Unlike perovskite with several structures and space groups, spinel usually

possesses the cubic structure with space group  $Fd\bar{3}m$ . With regard to the charge state, assuming  $O^{2-}$  as is predominantly valid in TMOs, there are two allowed patterns for A and B ions:  $A^{2+}/B^{3+}$  (common in most cases) or  $A^{4+}/B^{2+}$  (rare but does exist e.g.  $GeZn_2O_4$ ).

### 1.1.2 Electronic properties

TMOs have an extremely wide range of electronic behaviors, including those conventional metals and insulators which are classified according to the band theory, and also a variety of exotic systems such as high temperature superconductors, materials with metal-insulator transitions, and topological states of matters. The very diversity of behaviors of TMOs makes it almost impossible to develop a universal theory to describe their electronic properties. In physics, a generic strategy to simplify the complications is to first pay the most attention to the dominant term and treat others as corrections or perturbations. Following this logic, in practice, the essence of describing the electronic properties lies in how to select the starting point: whether the electrons are localized at their corresponding ions or moving itinerantly over the whole solid. Starting from different aspects, there have been several theoretical models established, which will be briefly introduced below.

**Ionic model.** This is a simple but extensively powerful model treating electrons in a local point of view. When we put a transition metal cation in a solid, besides the Madelung potential, electrons of this cation experience additional Coulomb interactions generated by its surrounding oxygen anions, which is called the crystal field. Serving as a perturbation source, the degenerate energy levels obtained from isolated atoms will be split. Note, since the  $d$  subshell is the outmost shell of a transition metal ion, its energy levels are significantly affected by the crystal field. As a result, the five spherical harmonics labeled by their quantum numbers  $(n, l, m)$  are no longer the eigenfunctions in a crystal field. Instead, the new eigenfunctions are linear combinations of those spherical harmonics as fol-

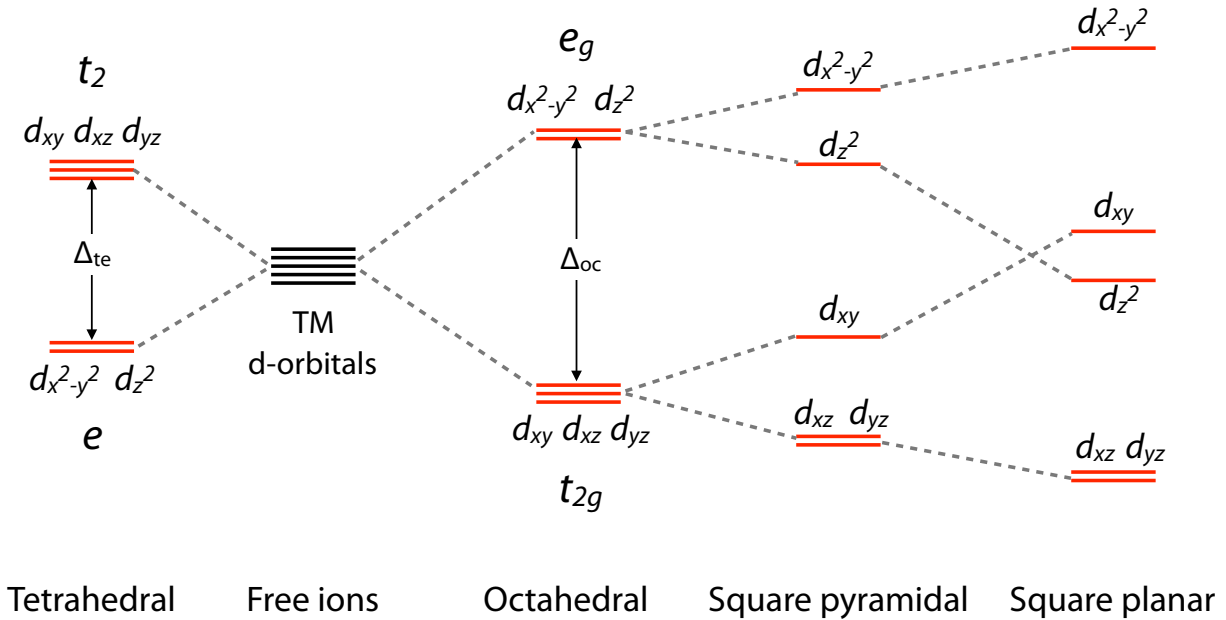


**Figure 1.3:** Shapes of the  $d$  orbitals. The notion of  $x$ ,  $y$ , and  $z$  refer to the wavefunction variables written in the Cartesian coordinate system.

lows:

$$\begin{aligned}
 d_{x^2-y^2} &\propto \sqrt{\frac{2\pi}{5}}(Y_2^2 + Y_2^{-2}) \\
 d_{3z^2-r^2} &\propto \sqrt{\frac{4\pi}{5}}Y_2^0 \\
 d_{xy} &\propto \frac{1}{i}\sqrt{\frac{2\pi}{5}}(Y_2^2 - Y_2^{-2}) \\
 d_{yz} &\propto \sqrt{\frac{2\pi}{5}}(Y_2^{-1} + Y_2^1) \\
 d_{xz} &\propto \frac{1}{i}\sqrt{\frac{2\pi}{5}}(Y_2^{-1} - Y_2^1)
 \end{aligned} \tag{1.3}$$

The shapes (electron density distributions) of these eigenfunctions are plotted in Fig. 1.3. Depending on the local symmetry of the crystal field (in other words, the geometry of the polyhedral coordination), the sequences of splitting can be quite different. Fig. 1.4 displays a few distinct  $d$  orbital splitting patterns under different crystal field symmetry. Specifically in this dissertation, we mainly face two types of crystal field: octahedral and tetrahe-



**Figure 1.4:** Energy splitting of the  $d$  orbitals under different crystal field symmetry. The notions of  $e_g$ ,  $t_{2g}$ ,  $t_2$ , and  $e$  are defined following the notions in group theory.

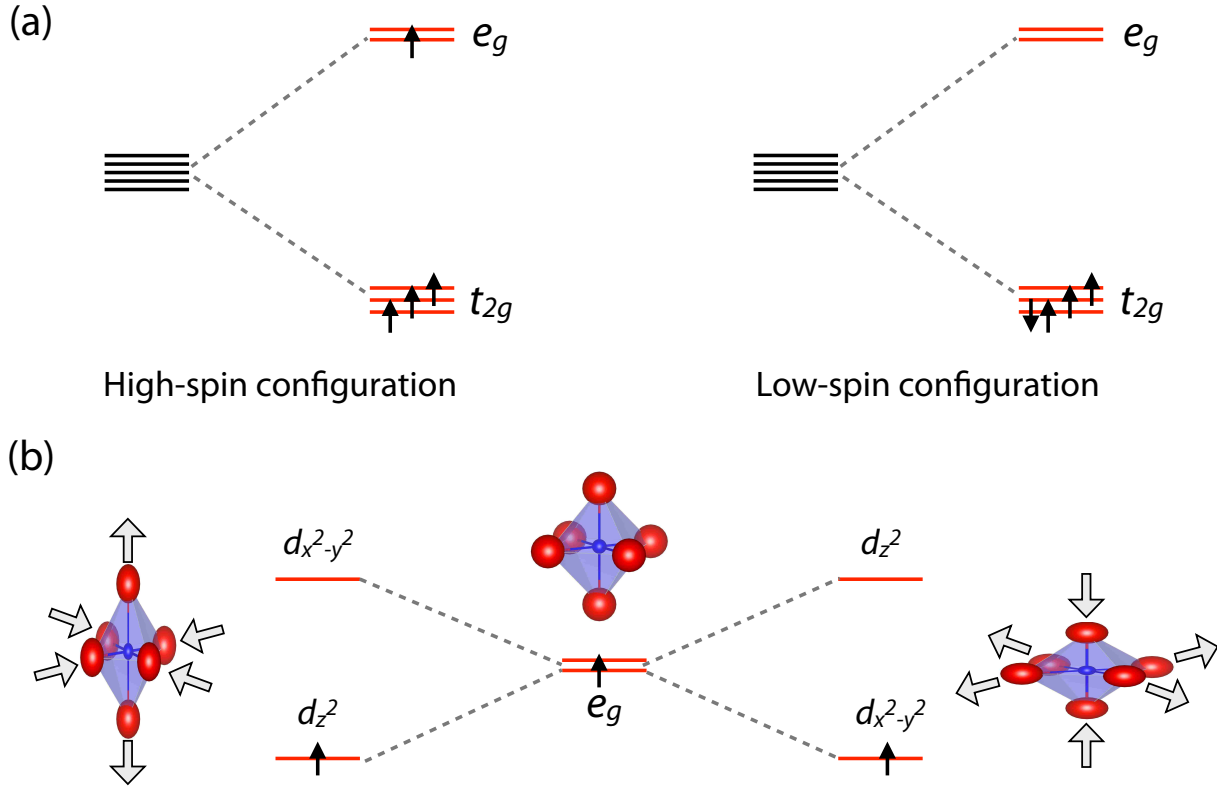
dral. In an octahedral field, the orbitals are split into an upper doublet  $e_g$  group including  $d_{x^2-y^2}$  and  $d_{3z^2-r^2}$  and a lower triplet  $t_{2g}$  group with  $d_{xy}$ ,  $d_{yz}$ , and  $d_{xz}$  states. Recalling the shapes of oxygen  $p$  orbitals versus these two groups, one can intrinsically understand the origin of the splitting. In an octahedral environment, the lobes of  $e_g$  orbitals always point towards those of  $p$  orbitals, effectively increasing the Coulomb repulsions between  $e_g$  and  $p$  electrons and lifting the energy levels. In contrast,  $t_{2g}$  orbitals have lobes pointing away from those of oxygen. Therefore, all  $t_{2g}$  levels are shifted downward. The energy gap between these two states is denoted as  $\Delta_{CF}$ . Similar analysis can be applied in the case of a tetrahedral environment, where the splitting pattern is reversed compared to the octahedral situation. It should be mentioned that further systematic studies on crystal field splitting is a major subject by itself and needs the knowledge of group theory.

Once the fivefold degeneracy of the  $d$  states is removed (or partially removed) due to the crystal field splitting, one can immediately notice that the electron occupation of the  $d$  levels strongly depends on  $\Delta_{CF}$ . For a single free atom, the electron configuration has

been well studied and summarized by the famous Hund’s rules. In short, electrons would like to occupy different degenerate levels to have the maximal total spin. However, now this strategy is challenged with the presence of a splitting energy. For example, let’s consider a  $d^4$  system under octahedral crystal field, as shown in Fig. 1.5 (a). According to the Hund’s rules, the first three electrons will occupy three different  $t_{2g}$  states. However, problem occurs for the fourth electron. The energy gain of occupying the higher  $e_g$  levels is  $-3J_H$  while the energy cost is apparently  $\Delta_{CF}$ . If the crystal field splitting is small ( $\Delta_{CF} - 3J_H < 0$ ), the Hund’s rules overcome the splitting effect. Consequently, the fourth electron will occupy one of the  $e_g$  levels with spin direction parallel to the others. This picture is named as the “high-spin configuration”. On the contrary, if the crystal field splitting is large ( $\Delta_{CF} - 3J_H > 0$ ), the occupation of one of the  $t_{2g}$  state with opposite spin direction (required by the Pauli’s rule) is more energetically favored, which instead decrease the total spin. This picture is called the “low-spin configuration”. The more delicate the  $d$  levels are split, the more complicated the spin configuration can be. Sometimes, as seen in Fig. 1.4, if the crystal field has a lower symmetry or if the spin-orbit coupling of the transition metal ion is not weak, the  $d$  orbitals can split into a few sub-levels with different splitting energies. As a result, the  $\Delta_{CF}$  vs.  $J_H$  comparison needs to be performed several times to determine the proper occupation. In this case, it is possible to have neither a high-spin nor a low-spin configuration, but rather a “intermediate-spin configuration” (e.g. in  $\text{LaCoO}_3$ ).

Another aspect which needs to be specially considered is the  $e_g^1$  part as shown in Fig. 1.5 (a). In this case, the electron can stay in either orbital due to the doublet degeneracy of  $e_g$  levels. However, Jahn and Teller in 1937 proposed a general statement, known as the Jahn-Teller theorem [24], which argues that the only degeneracy allowed in the ground state is the spin degeneracy. The orbital degeneracy is not the energy minimum and the system can further distort into some lower symmetry to lift the degeneracy and reduce its energy. As a result, the real ground state configuration of  $e_g^1$  in octahedral environment is shown in Fig. 1.5 (b). As seen, there are two approaches to lower the octahedral cubic symmetry. If the four in-plane oxygens are compressed and the two out-of-plane ones are elongated, the  $e_g$  levels are further split as displayed on the left panel. Or alternatively the elongation of the in-plane oxygens and compression of the out-of-plane ones will trigger the opposite result, as shown on the right panel. It is true that any distortion costs elastic energy but compared to the relatively large energy gain, this cost will not prevent the

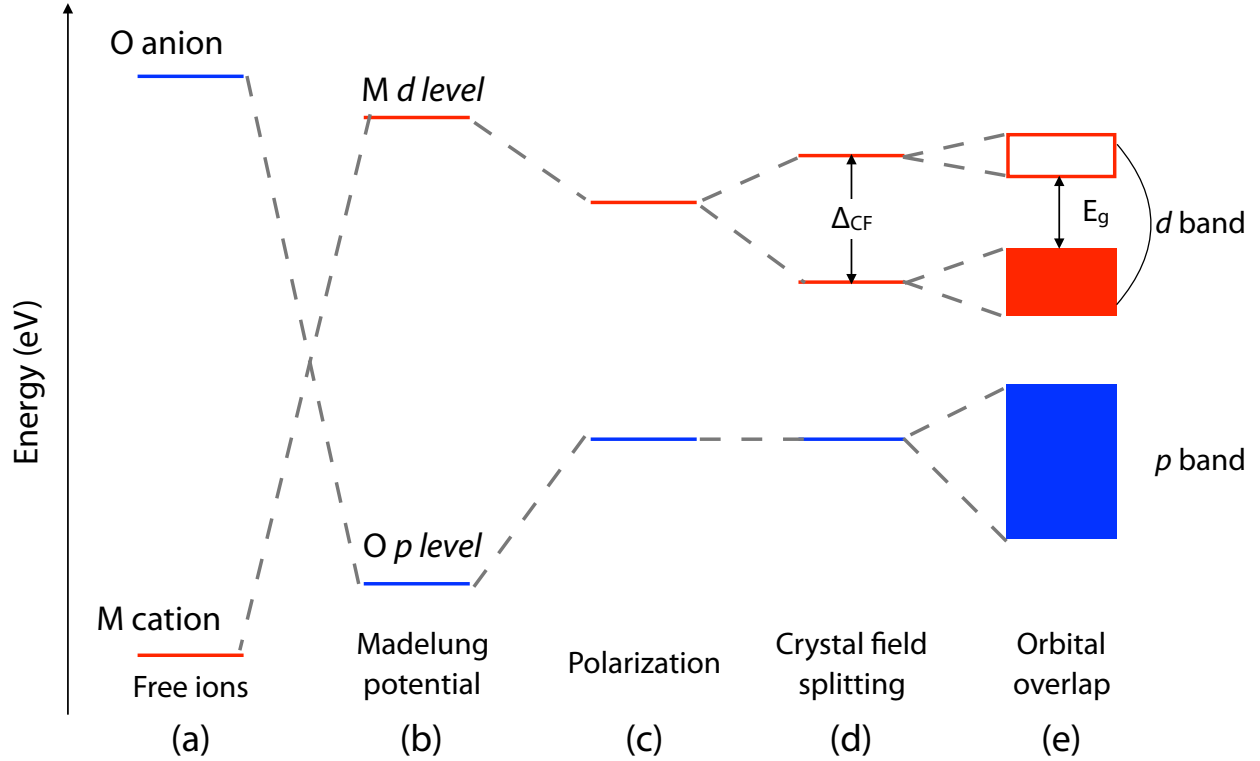




**Figure 1.5:** (a) High-spin configuration and low-spin configuration in a  $d^4$  system. (b) Jahn-Teller effect in systems with one  $e_g$  electron.

Jahn-Teller distortions if necessary. It should be emphasized that Jahn-Teller distortion is very common in systems with orbital degeneracy. An interesting phenomenon is that when the Jahn-Teller distortion takes place collectively all over the crystal lattice in a uniform pattern, the preferentially occupied orbitals of every transition metal site form certain long-range ordering, known as orbital ordering, which is an unusual state of matter. This state can exhibit strong anisotropy in electronic and magnetic behaviors.

The overall evolution of the electronic energy levels in the ionic model is summarized in Fig. 1.6. As seen, the relative energetic positions of O anion and M cation are reversed once they form the solid determined by the first-order correction, the Madelung potential, due to the opposite sign of charges. Then these levels are shifted closer to each other because of the polarization effect among the ions. Furthermore, due to the crystal field effect, the  $d$  levels will be further split. Finally, in each level, the orbital overlap gives rise to the formation of the band structure. Band gap may or may not exist depending on the degree of overlapping and also the strength of crystal field splitting. With respect to this



**Figure 1.6:** (a) - (e) Evolution of the electronic energy levels of TMOs in ionic model. O and M refer to oxygen and transition metal ion, respectively. Figure is adapted from Ref. [1].

diagram, the Jahn-Teller distortion can be inserted between step (d) and (e) as it is another effect to split the levels. But the occurrence of this effect is related to the specific electronic configuration and sometimes is suppressed by other factors.

In the framework of crystal field theory, the transition metal electrons are assumed to be localized at each site. However, in solid, electrons can hop onto neighboring sites as their orbitals overlap. Taking this delocalization process into account, calculations need to be expanded from a single atom to a molecular cluster which contains a central transition metal ion with its surrounding oxygens. The most common approach to deal with this problem is the tight-binding model [1, 2, 25, 26], in which any new set of molecular orbitals is written as a linear combination of the atomic orbitals:

$$\Psi = \sum_i c_i \phi_i \quad (1.4)$$

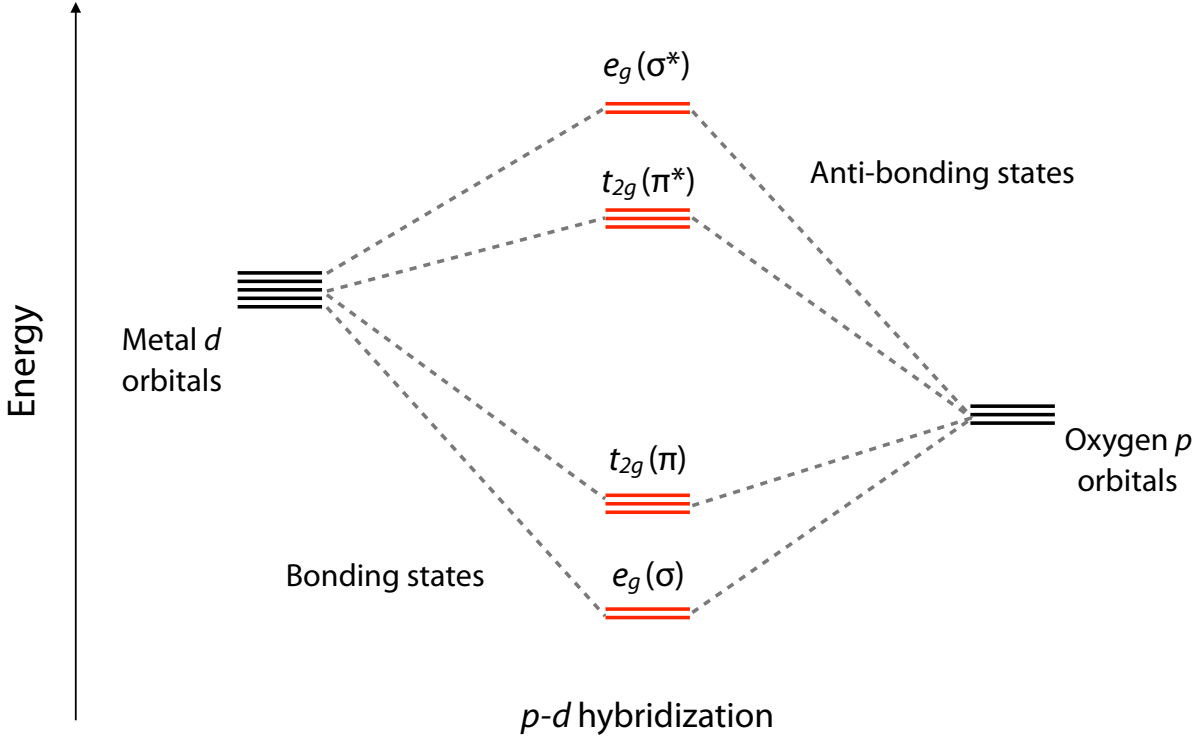
The resultant orbitals are hybridized with both transition metal and oxygen characters. The corresponding energy eigenvalues and eigenstates are extracted by solving the new

Hamiltonian including the overlap interactions as its off-diagonal elements:

$$\hat{H}\Psi = E\hat{S}\Psi \quad (1.5)$$

In which  $\hat{S}$  is the overlap matrices expressed in the basis of atomic orbitals. In TMOs, since transition metal ions' outmost shell are the localized  $d$  levels, of particular interest is the mixing between transition metal  $d$  and oxygen  $2p$  orbitals, the  $p$ - $d$  hybridization, because the oxygen  $2p$  levels are energetically very close to the  $d$  levels of transition. In chemistry, hybridization gives rise to the formation of covalent bonding, in which the electrons are shared by neighboring ions. The specific allowed orbital combinations, nevertheless, are governed by the local symmetry of the cluster. As a prototypical example, the diagram in an octahedral environment ( $\text{MO}_6$ ) is shown in Fig. 1.7 to illustrate this idea. On the one hand, for the doublet  $e_g$  set, since their orbitals have lobes pointing towards those of oxygen, the overlapping is stronger between these orbitals and the related energy modification is larger. They form the  $\sigma$ -type orbitals, as labeled on the diagram. On the other hand, for the triplet  $t_{2g}$  set, their lobes extend in directions away from the lobes of oxygen  $p$  orbitals, so the overlapping is relatively weaker and the energy modification is smaller. They form the  $\pi$ -type orbitals. Note, either the  $\sigma$  or the  $\pi$  type is composed of a pair of states,  $\sigma/\sigma^*$  and  $\pi/\pi^*$  as a result of the linear combination of  $d$  and  $p$  orbitals. Both  $\sigma^*$  and  $\pi^*$  states contain more metal characters with even higher energy than pure  $d$  levels. Therefore these states are unlikely to be occupied and named as "anti-bonding states". In contrast, the  $\sigma$  and  $\pi$  states have more oxygen characters and their energies are shifted beneath the oxygen  $2p$  levels. Therefore these states are preferentially occupied by electrons and named as "bonding states". Compared with crystal field theory, the splitting energy  $\Delta_{CF}$  in this case is the energy gap between  $\sigma$  and  $\pi$  states.

**Hubbard model.** The combination of the ionic model with traditional band theory has succeeded in describing the electronic structures of many TMOs fairly well. However, since 1937, it has been recognized that there are a number of transition metal compounds (e.g.  $\text{CoO}$ ,  $\text{NiO}$ ,  $\text{Fe}_2\text{O}_3$ ), which should be expected to be metallic, indeed possessing an insulating behavior. The failure in predicting these compounds' properties correctly strongly indicate some important factor is missing or neglected. It should be noted that for the sake of simplification, a common approximation has been used in both the ionic model and the band theory, the independent electron approximation, in which the electron-electron Coulomb repulsion is omitted. This interaction, also known as electron correlation, is weak



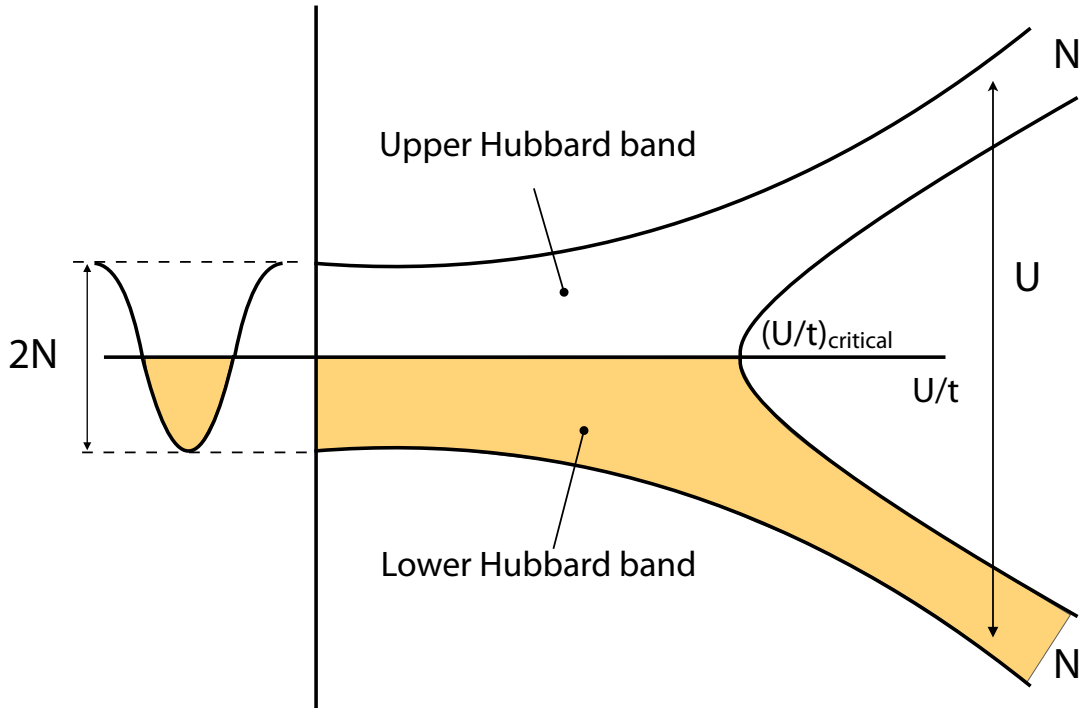
**Figure 1.7:**  $p$ - $d$  hybridization and molecular orbitals of a  $\text{MO}_6$  cluster. M refers to the central transition metal ion in an octahedron of six oxygens.

when the electrons are moving in a wide band. However, in TMOs, the partially filled  $d$  bands are usually very narrow so that the electrons are more localized and closer to each other. In this circumstance, the electron-electron correlations are inevitably turned on, exerting significant influence on the band structures and the overall physical properties of materials.

To quantitatively include this effect into account, the so-called Hubbard model has been proposed as [2, 4]

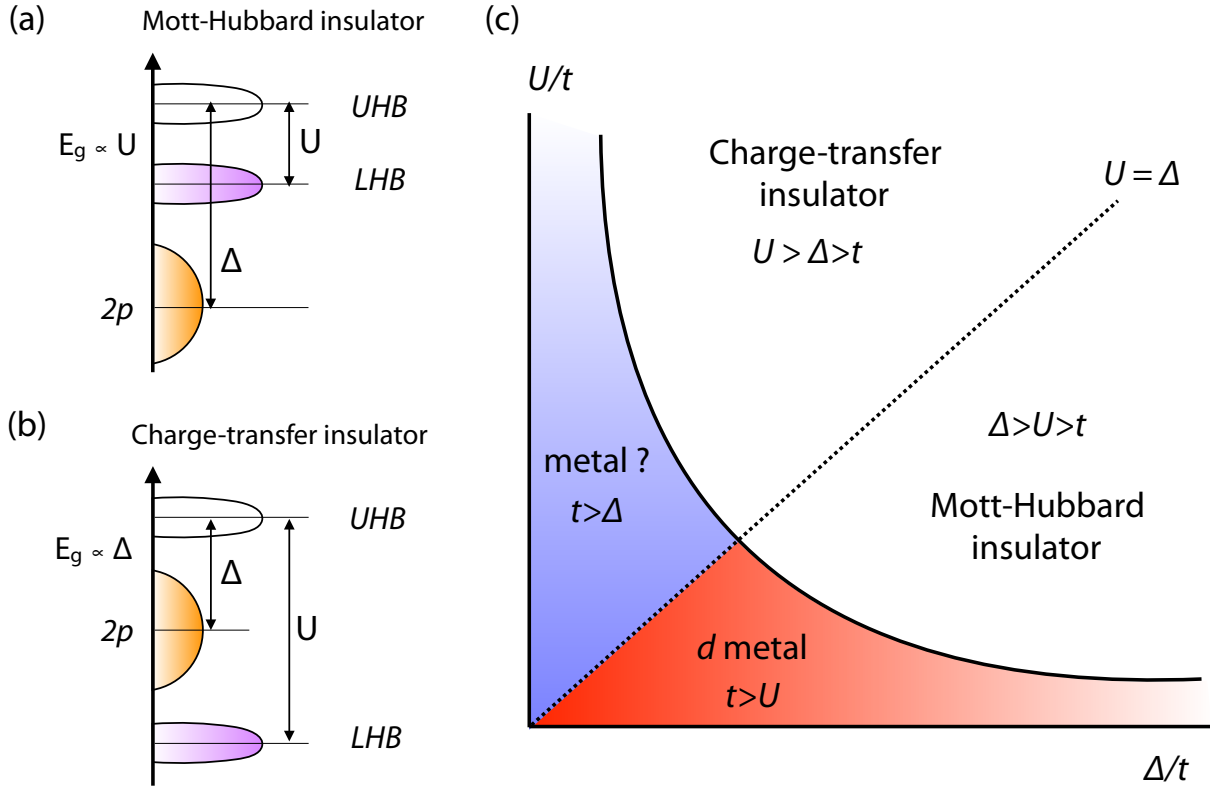
$$\hat{H} = -t \sum_{\langle ij \rangle, \sigma} c_{i\sigma}^\dagger c_{j\sigma} + U \sum_i n_{i\uparrow} n_{i\downarrow} \quad (1.6)$$

In this new Hamiltonian, the first term describes the hopping effect of electrons from a site to its nearest neighboring ones with no spin flip, whereas the second term is the extra repulsive energy cost for double occupation on the same lattice site. In this sense, the Hubbard model includes two competing processes together (localization vs. delocalization) and the true ground state is determined by the relative strength between Hubbard  $U$  and hopping integral  $t$ , which is proportional to the bandwidth  $W$ . The influence of Hubbard



**Figure 1.8:** Schematic illustration of the  $d$  band in Hubbard model. For a half-filling band, the electron correlation (Hubbard  $U$ ) is able to open a gap when its strength reaches the critical point. The two new split bands are called upper Hubbard band (empty) and lower Hubbard band (occupied). Figure adapted from [2].

$U$  on the electronic band structure can be illustrated in Fig. 1.8. According to the original band theory, if the valence band with  $2N$  capacity is half filled, the system is supposed to be a metal. But now electron-electron correlations serve as a new source to potentially open a gap in the valence band. If the correlation effect is weak compared to the bandwidth ( $U/t \ll 1$ ), the band will not be split and the material has metallic behaviors. If the correlation effect is strong ( $U/t \gg 1$ ), a band-gap emerges and separates the  $2N$  valence band into two new bands, called upper Hubbard band (UHB) and lower Hubbard band (LHB), each with  $N$  capacity. For this reason, the material instead is an insulator, which is denoted as a “Mott insulator” or “Mott-Hubbard insulator”. One has to notice the definition of Mott insulator is not trivial and many of the transition metal insulating compounds, which was predicted metallic, actually belong to this new class of materials. Recall that for ordinary band insulators or semiconductors, the energy gap is determined by the periodic potential of the crystal lattice. Here the energy gap arises solely as a result



**Figure 1.9:** (a) Energy level diagram of the Mott-Hubbard insulator. In this case, the gap  $E_g$  is determined by the correlation Hubbard  $U$ . (b) Energy level diagram of the charge-transfer insulator. In this case, the gap  $E_g$  is determined by the charge-transfer  $\Delta$ . (c) Zaanen-Sawatzky-Allen phase diagram. Note,  $U$  and  $\Delta$  represent the electron-electron correlation and charge-transfer energy, respectively.  $t$  is the electron hopping strength.

of electron-electron correlations.

Even more interesting but complicated phenomena can be deduced from Fig. 1.8. If starting from the noninteracting side ( $U = 0$ ) and gradually increasing  $U$ , we should sooner or later reach a critical point  $((U/t)_{critical})$  as shown in the figure, where a metal-to-insulator transition takes place. Similarly, this transition is called Mott transition. Among TMOs, there exists a great number of compounds which undergo such a transition. It has been observed that Mott transition can be triggered by factors such as temperature, pressure, and electronic and magnetic field. And this transition is usually coupled by variations in crystal structures and/or magnetic orderings. Because of this coupling, what is indeed the driving force of the Mott transition and what is the role of electronic correlations in this process, is still not clear.

Up to now, the effect of strongly correlated electrons is only considered on the transition

metal  $d$  bands. But as is known, the oxygen  $2p$  bands are slightly lower in energy to the  $d$  bands. Here we can also ask, once the UHB and LHB are formed, what are the relative positions with respect to the oxygen  $p$  bands? As seen in Fig. 1.9 (a) and (b), there are mainly two cases of energy level diagrams expressing their relative positions. The oxygen  $p$  band can be either lower than both of the Hubbard bands or in these two bands. TMOs belonging to the former case is a standard Mott-Hubbard insulator whereas those belonging to the latter case are given a new name, charge-transfer insulator. In order to explain the difference, firstly it is necessary to introduce a new energy scale, the so-called charge-transfer energy  $\Delta$ . Considering there are  $n$  electrons in the  $d$  levels,  $d^n$  configuration, there exist two types of excitation states. The electrons can either hop onto another already occupied site in the same  $d$  level, say  $d^n d^n \longleftrightarrow d^{n-1} d^{n+1}$ , or electrons of oxygen  $2p$  band can hop onto the empty  $d$  states, say  $d^n p^6 \longleftrightarrow d^{n+1} p^5$ . The first process would cost energy of  $U$ , while the second one would cost a certain amount of energy which is  $\Delta_{CT} = E_d - E_p$ , denoted as the charge-transfer energy  $\Delta_{CT}$ . Depending on the ration of  $U$  to  $\Delta_{CT}$ , the lowest charge-carrier excited state can be different. When  $\Delta_{CT} > U$  [Fig. 1.9 (a)], the oxygen  $p$  band lies lower than the LHB. The band gap is mainly determined by  $U$ . In this case,  $d^n d^n \longleftrightarrow d^{n-1} d^{n+1}$  cost less energy and this is what typically happens in a standard Mott-Hubbard insulator. Nevertheless, when  $\Delta_{CT} < U$  [Fig. 1.9 (b)],  $d^n p^6 \longleftrightarrow d^{n+1} p^5$  cost less energy and would be the lowest excited state. Here the band gap is determined by the charge-transfer energy  $\Delta_{CT}$ . The corresponding materials are called charge-transfer insulator as in this case, the excited electrons are from the oxygen  $p$  levels. And it turns out that following this paradigm, many of the TMOs actually belong not to the Mott-Hubbard but to the charge-transfer family: the prototypical examples are the high temperature superconducting cuprates, e.g.  $\text{La}_2\text{CuO}_4$  or  $\text{YBa}_2\text{Cu}_3\text{O}_{7-\delta}$ .

More complicated situations occur if a third parameter is taken into account, the bandwidth effect which is proportional to the electron hopping strength  $t$ . The discussions above are actually based on the prerequisite that  $\Delta_{CT} \gg t$  and  $U \gg t$  so that an insulating ground state would be expected. However, it could also be possible that the bandwidth is large enough in each case so that the gap is not opened. Then the ground state would be metallic. These ideas have been summarized in the so-called Zaanen-Sawatzky-Allen (ZSA) phase diagram [27], which is shown in Fig. 1.9 (c). For most transition metal compounds, their electronic structures can be qualitatively explained by this phase diagram.

### 1.1.3 Magnetic interactions

As seen from above discussions, when the electron correlation effect is turned on, the electronic properties of materials immediately exhibit great variety and complexity. In this section, we switched to another markedly important product of electron correlation — magnetic exchange interactions. It is known that in a multi-electron system, when their wave functions overlap, apart from the electrostatic Coulomb term, a pure quantum mechanical term  $J$ , called the exchange integral or exchange interaction also emerges. It reflects the energy related to changes of quantum states (both the orbital and the spin states) between two electrons. In general, if this term  $J$  is positive, the spins tend to align in the same direction (parallel). if it is negative, the spins tend to align in opposite directions (antiparallel). For an isotropic system, Heisenberg proposed a general Hamiltonian to quantify such interactions [4, 6]:

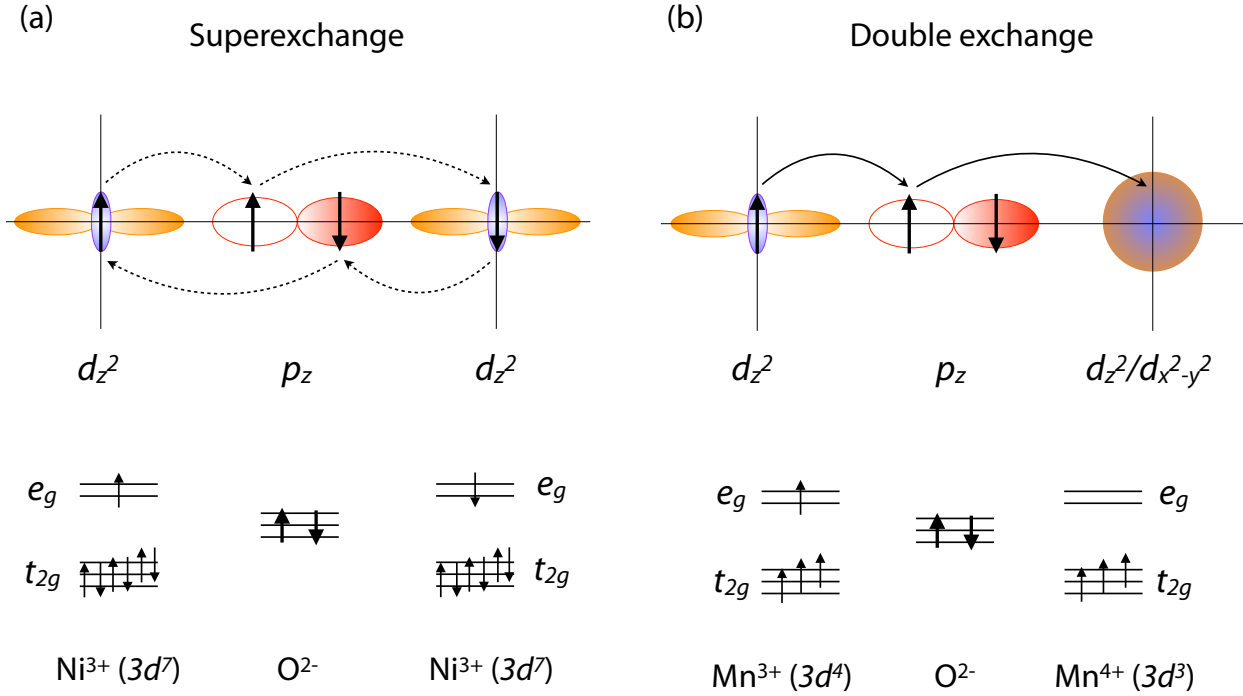
$$\hat{H} = - \sum_{i \neq j}^N J_{ij} \vec{S}_i \cdot \vec{S}_j \quad (1.7)$$

In which  $J_{ij}$  is the inter-atomic exchange coupling constant.  $\vec{S}_i$  and  $\vec{S}_j$  are the spins on the  $i$ -th and  $j$ -th atomic sites.

Based on the definition,  $J$  is obtained from direct orbital overlapping between adjacent atoms. This “direct exchange”, however, is unlikely in the case of transition metal compounds as a result of spacially localized feature of the  $d$  orbitals. But from the other perspective, with the help of the intermediary oxygen atoms, the exchange interaction can proceed in a different scenario: the wavefunction of an magnetic atom overlaps with nearest neighbor oxygen wavefunction, which in turn overlaps with the one from another magnetic atom. The oxygen atom serves as a “bridge” to connect two magnetic atoms which are located rather far away from each other. Thus, such a situation is regarded as “indirect exchange” and basically includes two types of interactions: superexchange and double exchange interactions.

The superexchange interaction plays a dominant role in determining the magnetic ground state of insulating transition metal compounds. As shown in Fig. 1.10 (a), the underlying mechanism can be illustrated by a  $d^7$  electronic configuration. The oxygen  $p$  band is assumed to be fully occupied, with each orbital containing a pair of opposite spins. Since it has an insulating ground state, the real electron hopping process is forbidden and no energy gain can be obtained. But considering the second-order perturbation, the “vir-





**Figure 1.10:** (a) Superexchange interaction paradigm in Ni ( $3d^7$ ) configuration. (b) Double exchange interaction paradigm in mixed valency  $\text{Mn}^{3+/4+}$  ( $3d^4/3d^3$ ) configuration.

tual hopping” process, some extra energy gain could be achieved due to delocalization if the spins on those two transition metal ions align antiparallel. Instead, if those spins are aligned parallel, the virtual hopping process is not allowed due to the Pauli’s exclusion principle. As a result, an antiferromagnetic (AFM) ground state is more favored. In general, the strength of the superexchange interaction mainly depends on three factors: the net magnetic moment of each transition metal ion, the metal-oxygen (M-O) bond strength, and the M-O-M bond angle. Although in most situations, the superexchange interaction would give rise to an AFM coupling, weak ferromagnetic coupling does exist. The detailed analysis on the sign and strength of superexchange has been well studied and summarized in the so called “Goodenough-Kanamori-Anderson” rules [6].

The superexchange paradigm has been applied quite successfully in many TMOs, especially in Mott insulators with integer number of localized  $d$  electrons to explain and predict their magnetic structures. AFM interaction is usually much more favored than ferromagnetic (FM). However, once a Mott insulator is doped by electrons or holes, at some point, a magnetic phase transition may take place and the original AFM insulator would

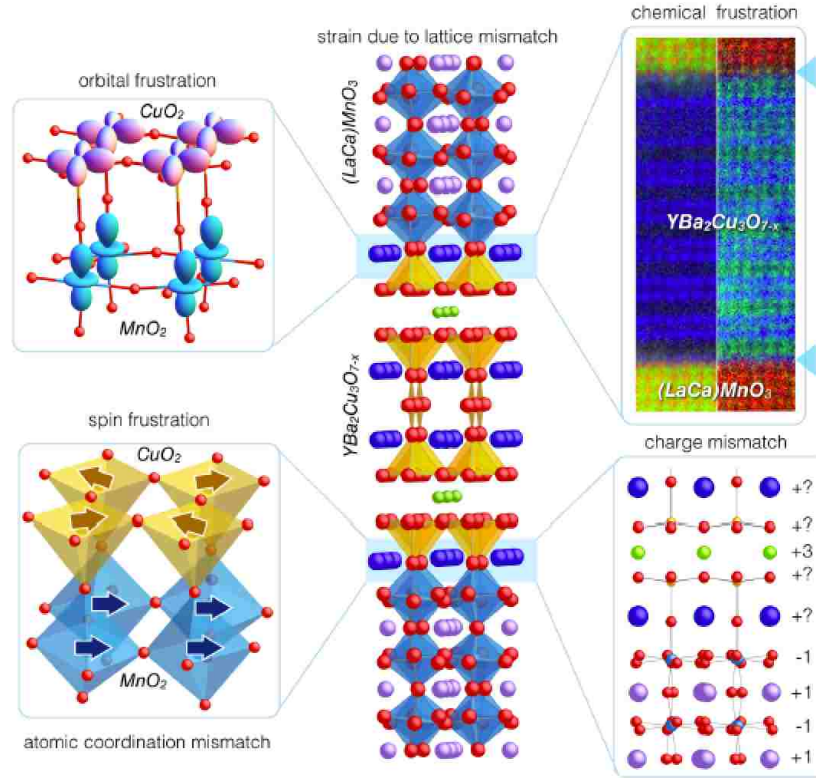
transform into a FM metal, e.g.  $\text{LaMnO}_3$  or  $\text{SrMnO}_3$ . In this case, both localized spins and itinerant charge carriers will coexist. In order to investigate this phenomenon, a novel picture, called “double exchange interaction” is proposed to shed light on what happens when the mobile carriers bypass those localized spins [4].

As shown in Fig. 1.10 (b), the double exchange interaction can be understood with an electron-doped manganite system,  $\text{La}_x\text{Sr}_{1-x}\text{MnO}_3$  ( $x$  is the doping level), in which Mn has a mixed valency of 3+ ( $d^4$ ) and 4+ ( $d^3$ ). The parent compound,  $\text{SrMnO}_3$  with pure  $\text{Mn}^{4+}$  is often AFM insulator following the superexchange interaction logic. When electrons from substitution of  $\text{Sr}^{2+}$  to  $\text{La}^{3+}$ , are doped into the Mn  $d$  levels, they will preferentially occupy the  $e_g$  states and keep the same spin directions as the  $t_{2g}$  electrons to gain Hund’s energy  $J_H$ . With small degree of doping, although the on-site Hubbard repulsion,  $U$  gradually increases, the electrons are still confined locally. However, once the doping exceeds certain threshold value, the electrons in  $e_g$  states tend to delocalize and hop onto neighboring site to reduce the total energy. But this kind of hopping will be quite weak if the background spins on  $t_{2g}$  are aligned antiparallel due to the lost of  $J_H$ . Therefore, to gain this extra kinetic energy, it will be more favorable to change the background magnetic structure from AFM to FM. This is because even though the superexchange energy gain is lost, this is just a second order effect, whereas the real electron hopping can bring large kinetic energy gain. For these reasons, the FM phase transition is often accompanied by the occurrence of conducting electrons, which is also a good signature of the underlying magnetic structural change.

There are also some other types of magnetic interactions which occur only in metallic TMOs such as RKKY (Ruderman-Kittle-Kasuya-Yosida) interaction, or Kondo interaction. More details can be found elsewhere [2, 4, 19] and will not be covered in this dissertation.

## 1.2 Interface engineering

The search and exploration of new collective quantum states are of prime importance and interest in the condensed matter physics. Towards this goal, ultra-thin heterostructures composed of two or more structurally, chemically, and electronically dissimilar constituent oxides have been developed into a powerful approach over the past few decades [3, 28, 29, 30, 31, 32]. The main notion here is that at the interface where the dissimilarities meet,



**Figure 1.11:** Mismatches at complex oxide interfaces, reproduced from Ref. [3].

the frustration caused by mismatches between arrangement of atoms, charges, orbitals, or spins can trigger the emergence of phenomena with electronic and magnetic structures markedly different from the corresponding bulk compositions [3]. As a result, the interface engineering has opened a route to novel material behaviors by means of those mismatches as the control parameters. Especially this method is intimately connected to another popular approach to tailor the properties of materials with epitaxial strain, by effectively altering the bond-length and bond-angle of structural units through the deliberate choice of substrates. The exploration of epitaxial strain due to the lattice mismatch has been thus far successfully used to manipulate the electronic bandwidth, band filling, ferroelectric, and magnetic interactions of many ultrathin films [33, 34, 35].

A good summary about the possible mismatches at oxide interfaces is shown in Fig. 1.11 [3]. Generally speaking, at the oxide interfaces, the following degrees of freedom, which may give rise to intriguing emergent phenomena are capable of being designed: (1) *Epitaxial strain*. Strain is a result of lattice mismatches between the atomic arrangement of two different TMOs. By delicately applying strain, the M-O-M' bond length and bond an-

gle can be effectively tuned, which may potentially trigger electronic and magnetic phase transitions. For instance, using epitaxial strain as the control parameter, ultrathin NdNiO<sub>3</sub> films have been reported to support a very fruitful phase diagram with several novel states not observed before in the bulk [33]; (2) *Local symmetry*. As discussed in the previous section, TMOs have a variety of local symmetry (or coordinate polyhedron). If two components with different local symmetries are managed to grow into a heterostructure, each of them needs to compromise and reach the balance point, an interracial structure deviating dramatically from their bulk counterparts. A robust example in this case is the  $\gamma$ -Al<sub>2</sub>O<sub>3</sub>/SrTiO<sub>3</sub> interface.  $\gamma$ -Al<sub>2</sub>O<sub>3</sub> has a spinel structure with tetrahedral and octahedral local symmetries whereas SrTiO<sub>3</sub> is perovskite with only octahedral symmetry. However, at their interface, an anomalous square pyramid local symmetry was found for Ti ions, which strongly affects the electronic band structures [36]; (3) *Polar mismatch*. Even having the same structure, from the ionic aspect, the net charge of each atomic layers can be distinct. While a heterointerface is made of entities with different net charges, the “polar jump” may occur and the charges near the interface have to be rearranged. This issue has been observed in many oxide heterostructures and was postulated as the origin of the emergent two-dimensional electron gases between two insulating TMOs [28]; (4) *Orbital occupation*. Most of the time, the variation of orbital occupation at oxide interfaces is coupled with the modulations of structures or charges due to their mismatches. Some peculiar orbital configuration can be triggered as a result of the interfacial reconstructions. For example, in ultrathin LaNiO<sub>3</sub>/LaAlO<sub>3</sub> superlattices, it was reported that unlike the bulk LaNiO<sub>3</sub> (Ni<sup>3+</sup>, 3d<sup>7</sup>), where the  $d_{x^2-y^2}$  and  $d_{z^2}$  orbitals are equally occupied,  $d_{x^2-y^2}$  is actually preferentially occupied at the superlattices interfaces [37]; (5) *Magnetic coupling*. Oxide interfaces are indeed an active tool to tune or design the magnetic interactions. One can imagine that if materials with different types of exchange coupling (for instance FM vs. AFM) are attached in close proximity, their incompatible nature may drive them to eventually form a new balanced state. This state could be a microscopical average of each composition. But it is also possible to generate an entirely new state with exotic features. For example, an interesting phenomenon has been discovered at the interface of a high  $T_c$  superconducting cuprate with a colossal magnetoresistance manganite, YBa<sub>2</sub>Cu<sub>3</sub>O<sub>7</sub>/La<sub>2/3</sub>Ca<sub>1/3</sub>MnO<sub>3</sub>, where surprisingly the superconductivity and the ferromagnetism can coexist [38].

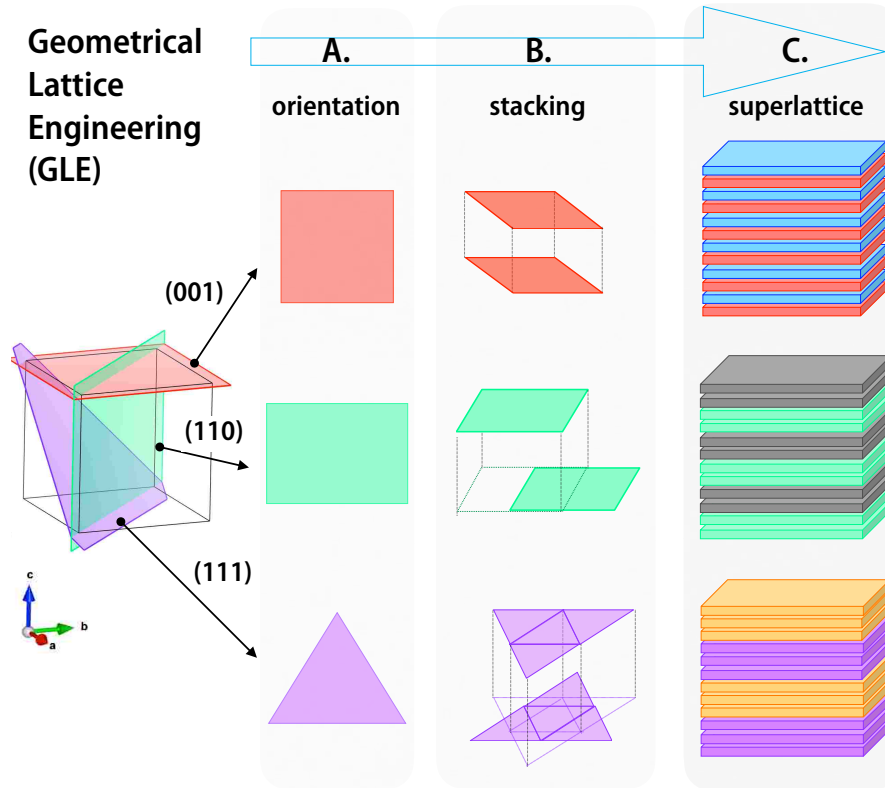
### 1.3 Geometrical lattice engineering

Inspired by the success of those interface engineering methods, very recently another promising venue, collectively known as the “geometrical lattice engineering” (GLE), has been presented as a powerful tool to forge new topological and quantum many-body states [39, 40, 41]. In close synergy with interface engineering and strain engineering where mismatches between layers can induce unusual interactions, the key idea behind the GLE is to design fully epitaxial ultrathin films and heterostructures with an artificial lattice geometry generated by stacking of a very specific number of atomic planes along a specific orientation. This concept can be further illustrated by recognizing that for a three-dimensional (3D) material, the stacking of two-dimensional (2D) atomic planes, the specific arrangement of ions in those planes, their sequence, and the periodicity of layers fulfilling a complete unit cell can exhibit drastic variations depending on the crystallographic direction along which it is projected. Conventionally, for rather thick bulk-like films, the effect of those variations is often negligible (apart from anisotropy), whereas for the ultrathin samples it becomes much more dominant in determining the electronic and magnetic properties. Following this idea, in the pursuit of exotic quantum states many interesting material systems have been proposed theoretically [39, 40, 41, 42, 43, 44, 45, 46, 47, 48, 49, 50, 51], while the experimental work on GLE has been primarily focused on growth of cubic or pseudocubic (111)-oriented artificial lattices [52, 53, 54, 55, 56, 57].

In general, the GLE concept is comprised of three controllable stages throughout the process of hetero-epitaxial fabrication. Here, we use a 3D simple cubic unit cell model to schematically illustrate these control parameters, as shown in Fig. 1.12.

*Growth orientation:* Starting with the same bulk compound, its 3D crystal structure is viewed as a stacking of atomic layers with different in-plane lattice geometries along different directions. For example, as shown in Fig. 1.12, while the (001) planes have square symmetry, the (110) and (111) planes have rectangular and triangular geometries, respectively. The required in-plane lattice geometry by design can be thus determined by selecting the proper structure and orientation of the substrate surface, which acts as a guiding template during the initial stage of nucleation and growth. A typical example for this case is the realization of 2D magnetically frustrated lattices derived from ultra-thin (111)-oriented spinel-type structure  $AB_2O_4$  [53].

*Out-of-plane stacking sequence:* In a bulk crystal, the periodicity of the atomic layers to



**Figure 1.12:** Schematic illustration of the idea about geometrical lattice engineering, which has three control parameters named as orientation, stacking, and superlattice throughout its entire process.

fulfill the requirement of translational symmetry as well as the relative atomic positions in neighboring lattice planes vary dramatically with the specific choice of the crystallographic direction. For instance, the stacking of the adjacent layers can be either right on top of each other [the (001) stacking in Fig. 1.12], or shifted [the (110) stacking], or even entirely reversed [the (111) stacking]. This observation is of paramount importance for the design of artificial heterostructures since by controlling the number of stacking layers within that period one can devise unique quasi-2D lattices that cannot be obtained in the naturally formed crystals. Among the prominent example of GLE we cite the generalized graphene lattice, which can be obtained by digitally tuning the number of atomic layers of (111)-oriented  $ABO_3$  perovskite-type structures for searching potential topological phases with and without spin-orbit active ions [54].

*Isostructural superlattices approach:* Combining isostructural materials together to establish superlattice structures via digital control over the individual number of layers adds another practical dimension to the application of GLE. This approach can be very useful for

the purpose of achieving materials with complex chemical compositions or even thermodynamically unstable phases in the bulk form. A representative test case is the fabrication of (111)-oriented  $1ABO_3/1AB'O_3$  superlattices [here “1” refers to single cubic (or pseudocubic) unit cell], that gives rise to  $A_2BB'O_6$  double perovskite [58].

The above discussions on GLE involved in this section has been published in the review paper [59], for which I am the first author.

The layout of this dissertation is as follows. Chapter 1 introduces the basic aspects about the structural, electronic and magnetic features of complex oxides, and reviews two types of heteroepitaxial engineering approaches: interface engineering and geometrical lattice engineering. Chapter 2 gives brief descriptions on each of the fundamental and essential techniques used in this dissertation. Then in Chapter 3, utilizing the idea of interface engineering, we will report on the recent discovery about a novel all perovskite two-dimensional electron gas system without  $SrTiO_3$ , the  $CaTiO_3/YTiO_3$  interface. In Chapter 4 and 5, selecting a spinel-type oxide,  $CoCr_2O_4$  as the playground, we will concentrate on the idea of geometrical lattice engineering as we, along with several other groups are the pioneering experimentalists in this field. Specifically, in Chapter 4, we will elaborate on the fabrications and basic characterizations on (111)-oriented  $CoCr_2O_4$  epitaxial films and ultrathin  $CoCr_2O_4/Al_2O_3$  superlattices. Details of advanced electronic and magnetic properties of these artificial systems are included in Chapter 5. There we will demonstrate that as the thickness of  $CoCr_2O_4$  is reduced towards the 2D limit, emergent magnetic behaviors appear. Most attractively, a possible quantum spin-liquid phase may have been achieved at this 2D limit. In the end, summary is made in Chapter 6, where we will also present outlooks on each of the topics involved in this dissertation for future works.

## Chapter 2

### Experimental techniques

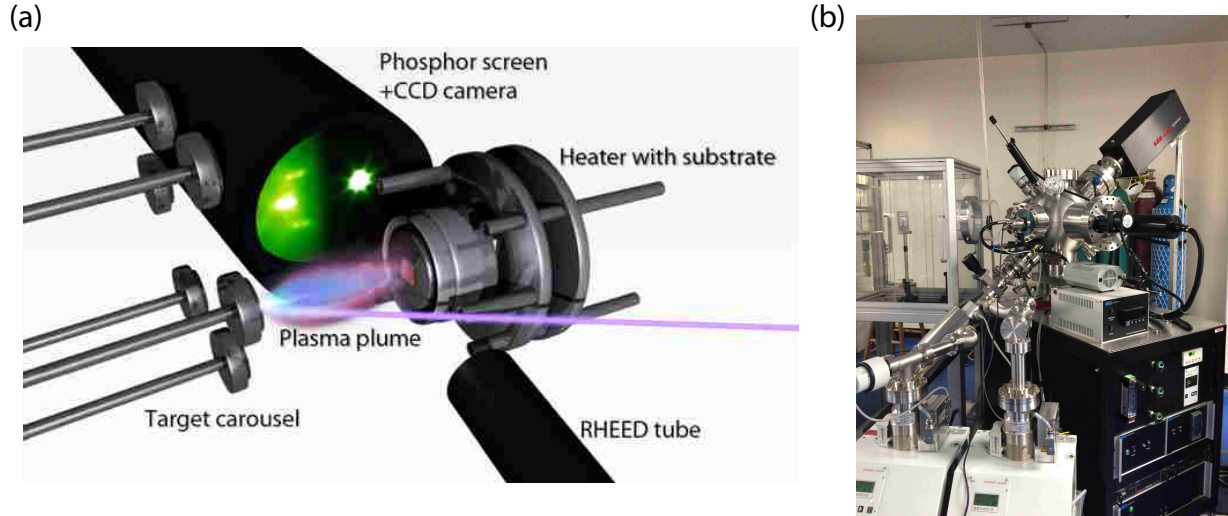
In this chapter we will introduce the experimental techniques used for the development and characterizations of complex oxide thin films and heterostructures in this dissertation. First, we start with the synthesis technique, pulsed laser deposition (PLD), discussing in details about the in-house setup, general principles, control parameters and different growth modes of the thin film deposition process monitored by *in-situ* reflection high energy electron diffraction (RHEED). Then, we will show how to examine the structural properties of our samples by high-resolution X-ray diffraction. Next, we will describe how to achieve microscopic investigations by means of synchrotron-based X-ray absorption spectroscopy (XAS) and Polarized Neutron reflectometry (PNR), which are highly advanced techniques to reveal the underlying electronic and magnetic structures of these designed materials.

#### 2.1 Epitaxial thin film growth

##### 2.1.1 Pulsed laser deposition

During the last two decades, PLD has proven to be a markedly powerful technique for fabricating epitaxial thin films and heterostructures. Comparing with other deposition techniques such as magnetic sputtering or molecular beam epitaxy, there are several advantages that make PLD particularly successful in growing complex oxides films. These include relatively simple instrumentation, stoichiometric transfer of material from the targets, energetic forward-directed plume, and hyperthermal interaction of the ablated species with the background gas (e.g. oxygen). In general, it is a physical vapor deposition process performed in a vacuum system using a laser as the heating source for ablation [60]. A typical schematic inside the growth chamber and a real apparatus setup in our laboratory are shown in Fig. 2.1. During the deposition, a pulsed laser (about 20 nano-second) is focused on a small portion of a ceramic/polycrystalline target, which usually has the same chemical stoichiometry as the desired film. With sufficiently high energy fluency of 1 - 2 J/cm<sup>2</sup>, the ejected materials from the target vaporized by each laser pulse generates a





**Figure 2.1:** (a) A schematic of the environment inside a PLD main chamber. (b) Photograph of the PLD system used in this dissertation.

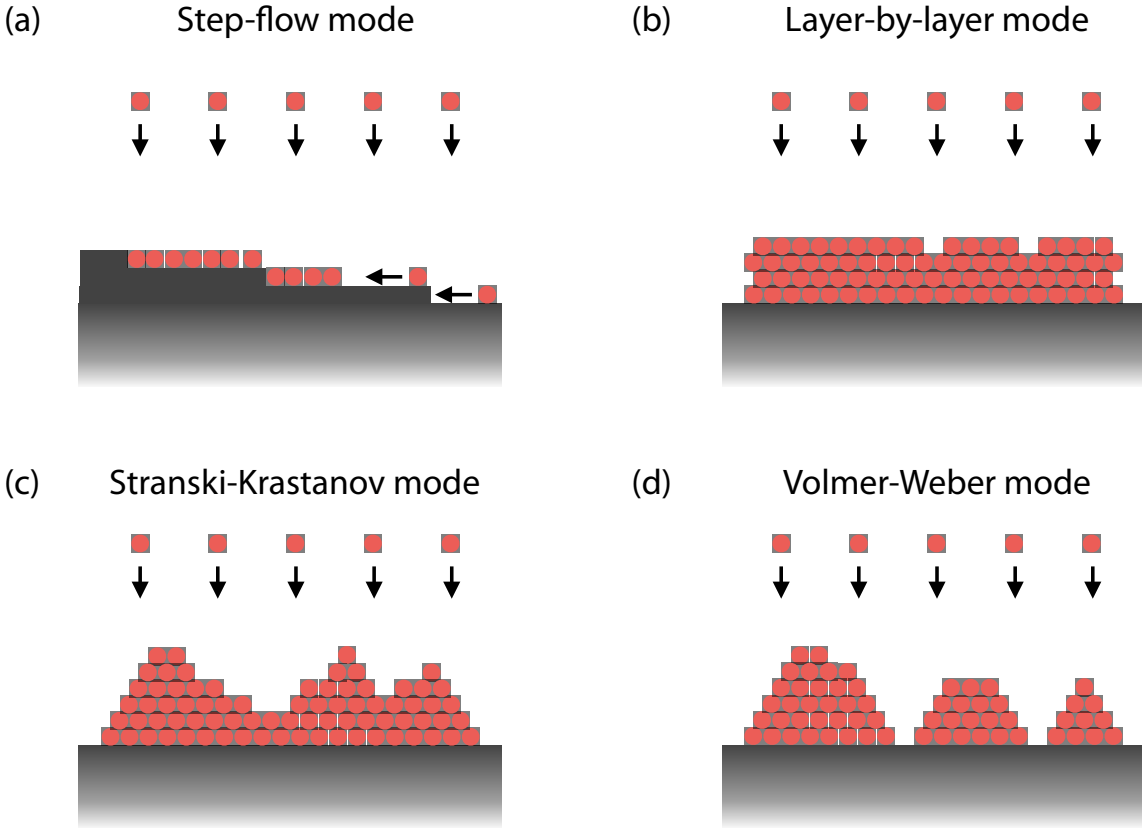
plasma plume consisting primarily of atomic, ionic and other low-mass species. This highly forward-directed plume then transverses to the substrate in a background gas atmosphere ranging from ultrahigh vacuum (for example  $10^{-8}$  Torr) up to 1 Torr [60]. The flux of materials reaching the substrate eventually nucleates and crystallize into epitaxial solid films. In order to obtain high quality epitaxial films using a PLD system, one has to make proper selections on both the targets and the substrates and also optimize a few control parameters [61]. Let's start with the targets. Since a complex oxide compound typically contains two or more types of elements, an appropriate target for PLD should be uniform and highly dense, possessing identical phase or at least identical cation stoichiometry to the desired film. It has been known that if the laser ablates a loose target, the resultant film can exhibit quite rough surface with amounts of molten droplets directly ejected from the target. In the meanwhile, the substrate is chosen such that it has a close lattice parameter and symmetry to the film. This is extremely important in determining the epitaxial orientation of the film since the substrate serves as the template during the nucleation and subsequent growth. In this dissertation, all the targets are fabricated by solid state reactions and pressed into dense pellets with 1 inch (diameter)  $\times$  0.25 inch (thickness), and all the substrates are commercially available single crystals cut into 5 mm  $\times$  5 mm  $\times$  0.5 mm (thickness) pieces with a miscut angle smaller than  $1^\circ$ .

Once the substrate and the target are selected, the remaining factors which can affect the

deposition process are mainly: laser energy and fluency, background gas pressure, target-to-substrate distance, and substrate temperature. Among these factors, we commonly fix the values of laser energy (KrF excimer laser:  $\lambda = 248$  nm) and target-to-substrate distance ( $d = 4 - 6$  cm) as their tuning effects can be realized by the other three parameters. With respect to the laser fluency, when it is low, the result of each laser pulse would be similar to thermal heating. In this case, the ejected flux of materials may possess a deviated stoichiometry off the target due to the differences in vapor pressures among each constituent. To avoid this issue, one has to increase the laser fluence high enough to overcome the ablation threshold of the target, above which the evaporation is independent of the vapor pressure so that the plume maintains its proper stoichiometry. However, running deposition with too high fluence would render the formation of macroscopic droplets or even damage the target. As a result, the typical range of our laser fluence is 1–4 J/cm<sup>2</sup>. When using PLD to grow complex oxide films, molecular oxygen is often required as the background gas for two main reasons. Firstly, the ejected low-mass species needs to assemble with O<sub>2</sub> to get the desired phase. Moreover, the background gas is also used to reduce the kinetic energies of the plume. It is known that the kinetic energies of the atoms and ions in the plume can reach as high as several hundred electron volts [60]. With such high speed, the species will collide with the substrate surface intensely, sputtering off the grown films and creating defects. The background gas can effectively scatter the proceeding species and decrease their energy down to sub-electronvolt range.

Last but not least, the substrate temperature is another critical factor in determining the quality of the films. However, the roles that it indeed plays during the deposition process is considerably complicated. On one hand, high substrate temperature is usually favored since it enhances the mobility of the adatoms so that they can rearrange, forming the flat surface morphology. On the other hand, high temperature could also evaporate constituents with high vapor pressures out of the film, resulting in oxygen vacancy defects or missing of the right stoichiometry. Another issue occurs when growing a superlattice structure composed of various oxide components. The thermally active atoms of each component can diffuse across the interface, destroying the atomic sharpness of the interface. In addition, for many oxides with low crystal symmetries, the epitaxial orientation of the film is very sensitive to the substrate temperature, leaving a rather narrow window for each phase.

All in all, even though we have discussed the general trends of each control parameter of



**Figure 2.2:** Various growth modes in PLD. (a) Step-flow mode; (b) Layer-by-layer mode; (c) Stranski-Krastanov mode; (d) Volmer-Weber mode.

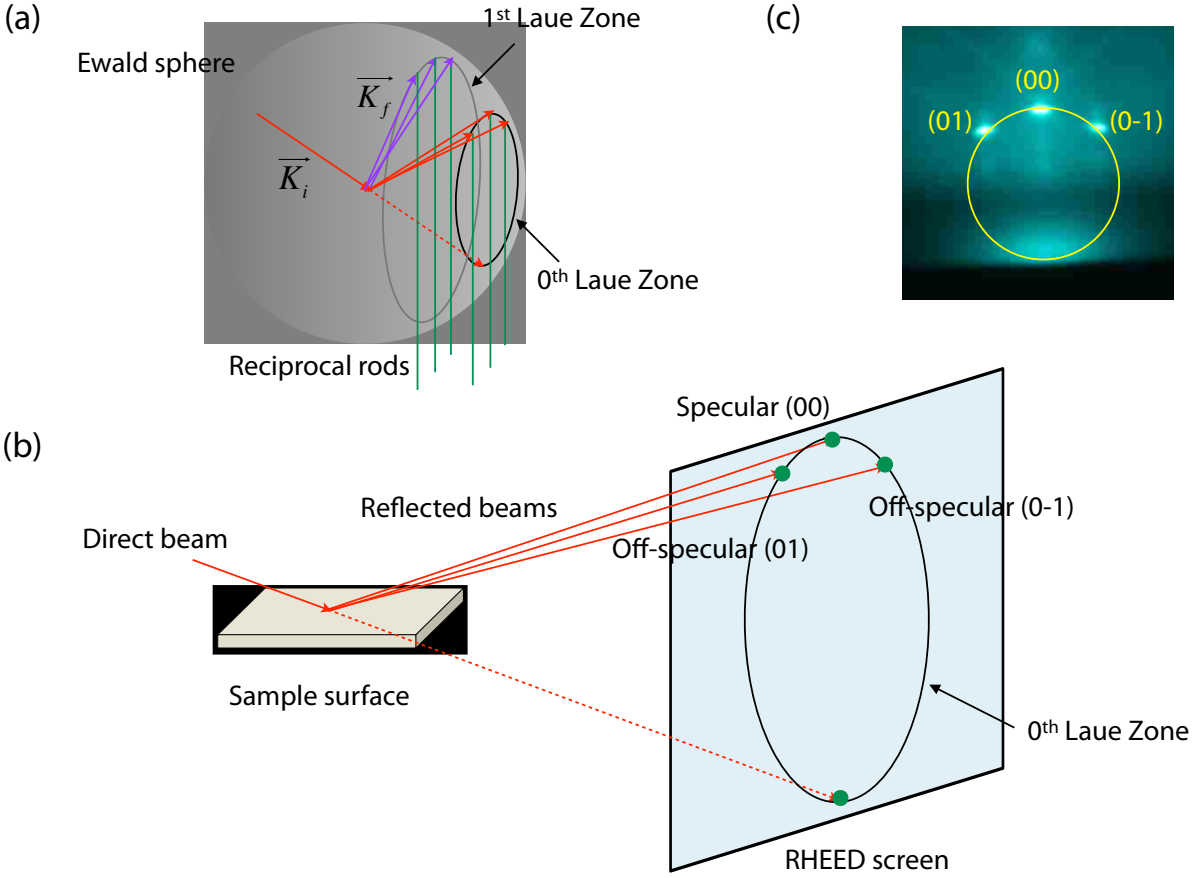
PLD, the specific values of these parameters are truly material- and instrumentation- dependent. In reality, it is usually necessary to explore a comprehensive phase diagram so as to find and optimize the best growth condition. Under typical conditions, the deposition rate varies from a few tenths up to one angstrom per laser pulse. This feature enables the precise control of growth on the level of a submonolayer and makes PLD extremely promising in the fabrications of multilayers and superlattices of complex multi-element materials [60, 61, 62].

After describing the general principles of PLD and its control parameters, the next step is to understand the growth dynamics. Conventionally, the nucleation and growth of thin films is described under the assumption of (near) thermodynamic equilibrium. However, because of the off equilibrium nature of PLD, the kinetics of the arriving species has to be considered as well [62]. Thus, in general, there are four growth modes as shown in Fig. 2.2, which are commonly encountered in PLD: step-flow mode, layer-by-layer mode, Stranski-

Krastanov mode, and Volmer-Weber mode. In the following we will briefly discuss the mechanisms underlying these modes.

As the cut angle of substrate cannot be perfect along the surface orientation, this leads to formation of vicinal substrate with steps and terraces, as seen in Fig. 2.2 (a). As the kinetic species reaching the substrate surface, the adatoms will propagate on the terraces. If the diffusion length  $L_D$  of the adatoms is larger than the width of terraces  $W_T$ , they can freely move to the step edges and then start nucleating there. The overall effect exhibits as if all of the steps are extending stably with constant growing speed. This regime is therefore called “step-flow mode”. However, in situations where  $L_D$  is less than  $W_T$ , nucleation will take place on terraces before the adatoms reach the step edges, forming amounts of isolated monolayer nucleus. The subsequent atoms which fall on these nucleus can either move to the edges and quickly diffuse down to the lower layer, or attach on top to form a second layer. As a result, the former case assures that a second layer will not nucleate until the lower layer has been fully covered, which is displayed in Fig. 2.2 (b) as the “layer-by-layer mode” (also called Frank-van der Merwe mode). The latter, however, represents the formation of 3D islands, corresponding to Fig. 2.2 (d). The intermediate situation is shown in Fig. 2.2 (c): In the initial stage the layer-by-layer growth mode is favored but it gradually transforms into the island growth.

Among these modes, both step-flow and layer-by-layer belong to the family of 2D growth, which is the prerequisite for fabricating high quality epitaxial thin films and heterostructures with smooth surface morphology and sharp interfaces. To achieve this goal for a desired material, one often has to adjust the control parameters (temperature, pressure, laser intensity) until a favorable regime of growth conditions is discovered. However, tuning of the control parameters is limited by both the stability of the desired phases and the specific apparatus. Therefore it may happen that a proper condition can never be reached with the conventional PLD process. A rather generic solution was proposed by Blank *et al*, named as “pulsed laser *interval* deposition” [63]. In this method, instead of running the deposition continuously at a slow laser ablation rate (1 or 2 Hz), it is found that depositing every unit-cell material at a very high laser ablation rate (such as 10 Hz or more) followed by a relaxation interval with no deposition can effectively improve the layer-by-layer growth mode under unfavorable conditions. This is due to the fact that such a fast deposition triggers high supersaturation of material, which promotes the formation of many small islands on the nanoscale, thereby reducing the average size of each



**Figure 2.3:** (a) Geometrical representation of Ewald sphere and Laue condition. (b) Schematic of RHEED and the normal pattern exhibited on a camera screen. (c) A typical RHEED image of (001) SrTiO<sub>3</sub> substrate taken from our machine.

island. As a result, multi-level growth, which would collapse into 3D growth in the end, will be avoided since only very small islands can be generated. It is worth noting that this method is unique for PLD only since no other technique is capable of realizing high deposition rates with long standby intervals at the same time.

### 2.1.2 Reflection high energy electron diffraction

During the deposition process, *in-situ* monitoring the dynamics of growth is of great importance in uncovering the underlying mechanisms and giving feedback to optimize the conditions. RHEED is therefore designed and combined with a PLD system for this purpose. As a diffraction method applied on solids, it follows the basic kinematical theory of

scattering. The possible reflections satisfy:

$$\vec{k}_f - \vec{k}_i = \vec{G} \quad (2.1)$$

Where  $\vec{k}_f$  and  $\vec{k}_i$  are the reflected and incident beams, respectively.  $\vec{G}$  is a reciprocal lattice vector of the solid. If considering only the elastic scattering events, it requires:

$$|\vec{k}_f| = |\vec{k}_i| \quad (2.2)$$

These two conditions together are the so-called Laue conditions, which is geometrically represented in Fig. 2.3 (a). The head of  $\vec{k}_i$  is fixed on a reciprocal lattice point and the sphere around the end of  $\vec{k}_i$  defines the Ewald sphere with radius  $|\vec{k}_i|$ . In this construction, any vector which connects the center to a reciprocal lattice point on the sphere surface is a valid  $\vec{k}_f$ . The distribution of reciprocal lattice points on Ewald sphere is special. Since RHEED is really surface-sensitive (it detects only a few atomic layers beneath the surface of sample) [64], the corresponding reciprocal lattice of the surface is a family of parallel rods, as shown in Fig. 2.3 (a). These rods intersect with the Ewald sphere, giving rise to the allowed reciprocal lattice points distributed on different circles called Laue zones.

A brief schematic of RHEED is displayed in Fig. 2.3 (b). A beam of electrons is incident on the surface of sample at the grazing angle of only a few degrees. The diffractions are sensed by a phosphor camera screen. Neglecting the relativistic correction (this is valid for  $E < 50$  keV), the wavelength  $\lambda$  of the beam is related to the electron energy  $E$  and can be calculated conveniently using the following expression [65]:

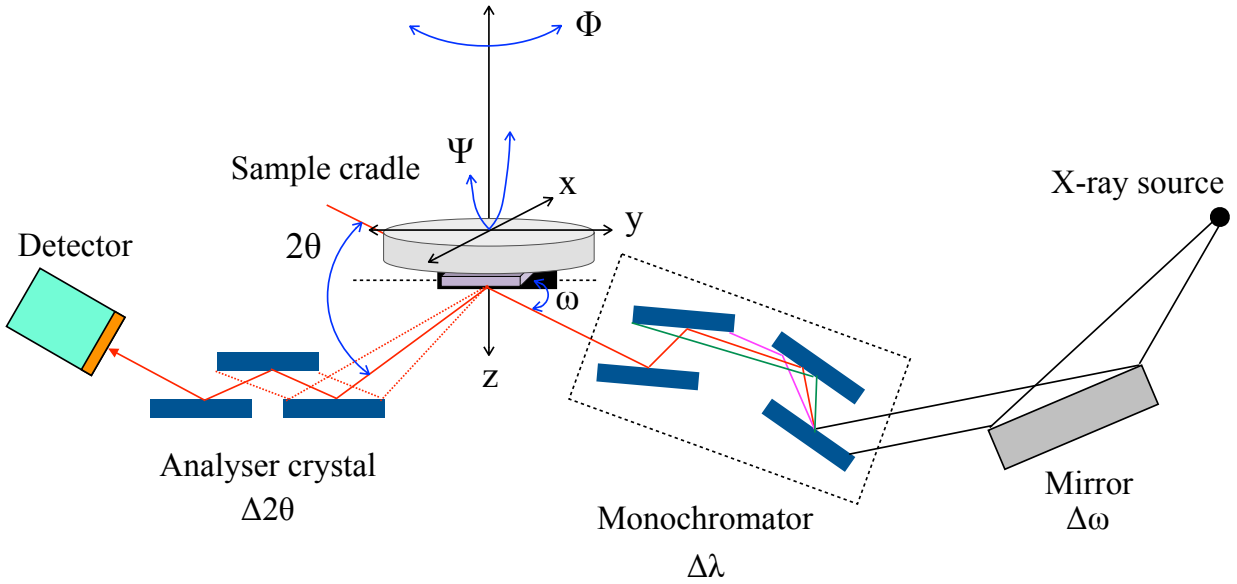
$$\lambda = \sqrt{\frac{150.4}{E}} \quad (2.3)$$

In which the unit of  $\lambda$  and  $E$  are  $\text{\AA}$  and eV, respectively. In this dissertation, we tune  $E = 25$  keV so that  $\lambda = 0.0775$   $\text{\AA}$ . This guarantees the general diffraction condition is satisfied ( $\lambda \ll d$ ) and the radius of Ewald sphere ( $k = 2\pi/\lambda$ ) is large enough to include the first few Brillouin zones. With these settings, a typical RHEED image of a (001)-oriented SrTiO<sub>3</sub> substrate is shown in Fig. 2.3 (c). The 0<sup>th</sup> Laue zone (yellow circle) is clearly seen with both the specular reflection (00) and the off-specular reflections (0 $\pm$ 1) on it. In addition, there also exist some dark but sharp lines crossing these spots, which are known as the Kicuchi lines originating from inelastic multiple scattering events. These observations provide strong evidence on the smooth surface morphology.

The variation of RHEED pattern as well as RHEED intensity is straightforwardly linked to the growth modes. On one hand, for 2D modes (step-flow and layer-by-layer), the distinct specular and off-specular spots, together with the direct beam spot will always be distributed on a ring. As the surface roughness is barely changed in step-flow mode, the coherent scattering condition is preserved so that the intensity almost remains constant during the deposition. This behavior is significantly different from that in layer-by-layer mode, where the roughness is periodically changed by the surface coverage. Therefore the intensity is expected to oscillate as a function of time, with certain number of laser pulses in every oscillation corresponding to the growth of one monolayer. However, it is more common to observe RHEED oscillations with a damping behavior in real experiments. This could happen when the adatoms propagate on a relatively large terrace area, and the insufficient mobility prevents them arriving at the step edges and diffusing down to the lower layer. Consequently nucleation on a second layer takes place before the first layer is 100% completed. Accordingly the surface roughness can never reach the minimal value and the RHEED oscillation no longer recovers back to the previous level. Comparing these two growth modes, it is clear that by counting the number of pulses or oscillations, layer-by-layer mode allows us to digitally control the film thickness with atomic precision. On the other hand, for the Volmer-Weber mode (3D island growth), the reciprocal lattice rods in Fig. 2.3 (a) is replaced by 3D matrix of points. As a result, instead of seeing a ring-like distribution, the RHEED pattern is a 2D grid. Moreover, no RHEED oscillation will be observed. As the intermediate situation (Stranski-Krastanov mode), the RHEED image initially exhibits the ring-like pattern. Then the reflection spots gradually fade and become streaky due to the increasing roughness. In the meanwhile, it is possible to observe several damping oscillations at the initial stage of growth, followed by the disappearance of any oscillation later on and a rather low intensity value.

## 2.2 High-resolution X-ray diffraction

For epitaxial thin films and heterostructures, structural characterization is of primary importance to obtain information on the crystalline status of the samples. This generally includes thickness, polycrystallinity, orientation, surface and/or interface roughness, lattice parameter, epitaxial relationship and strain state, which requires the measurements of Bragg peak positions at a precision of 0.01 degree. This is at least an order of magni-



**Figure 2.4:** Schematic of high-resolution X-ray diffractometer in triple-axis geometry. The sample cradle has six motorized movements  $x$ ,  $y$ ,  $z$ ,  $\omega$ ,  $\Phi$ ,  $\Psi$ , and the detector has another independent movement  $2\theta$ .  $\omega$  is the angle between incident beam and sample surface;  $2\theta$  is the angle between incident and diffracted beams;  $\Psi$  is the sample tilt angle;  $\Phi$  is the azimuthal rotation angle around surface normal. The lines drawn in red, purple, and green colors in the monochromator represent X-rays with various wavelengths within the incident beam.

tude more precise than what is reached by a conventional powder diffractometer. There are mainly three sources that lower the resolution of measurements. First, on the incident beam path, the X-rays emitted from the tube gradually diverge as they are propagating. In addition, several different wavelengths such as  $K_{\alpha 1}$ ,  $K_{\alpha 2}$ ,  $K_{\beta 1}$  and  $K_{\beta 2}$  are contained at the same time in the beams. Moreover, the issue of beam divergence also exists on the diffracted path, which provides a third error source reducing the precision. In order to solve these problems, a high-resolution X-ray diffractometer (HRXRD) equipped with multiple controllable dimensions is needed. This has been established using the so called triple-axis geometry [66], as shown in Fig. 2.4. The three axes are those controlling the incident beams, the samples, and the analyzer, respectively. As displayed in Fig. 2.4, a mirror is inserted after the X-ray tube, followed by a channel-cut beam monochromator. This combination of optical devices allows to narrow the divergence angle of incident beams



down to  $\sim 0.003$  degree and filter out all other wavelengths except for  $K_{\alpha 1}$ . In the meanwhile, a sample cradle with six motorized movements is equipped so that both symmetric and asymmetric reflections can be probed. Angular restriction of the diffracted beams is performed by placing a channel-cut analyzer crystal in front of the detector, which preserves the direction of the beam scattered from the sample and improves the  $2\theta$  precision to several ten-thousands of one degree. It is worth noting that compared to traditional powder diffraction measurements, the intensity of HRXRD is considerably lower due to the collimation and monochromatization process, which can be compensated by prolonging the recording time.

With the help of HRXRD, the structural parameters as mentioned at the beginning of this section become accessible. In the following we will briefly describe three of the most fundamental and useful measurements that are used in this dissertation.

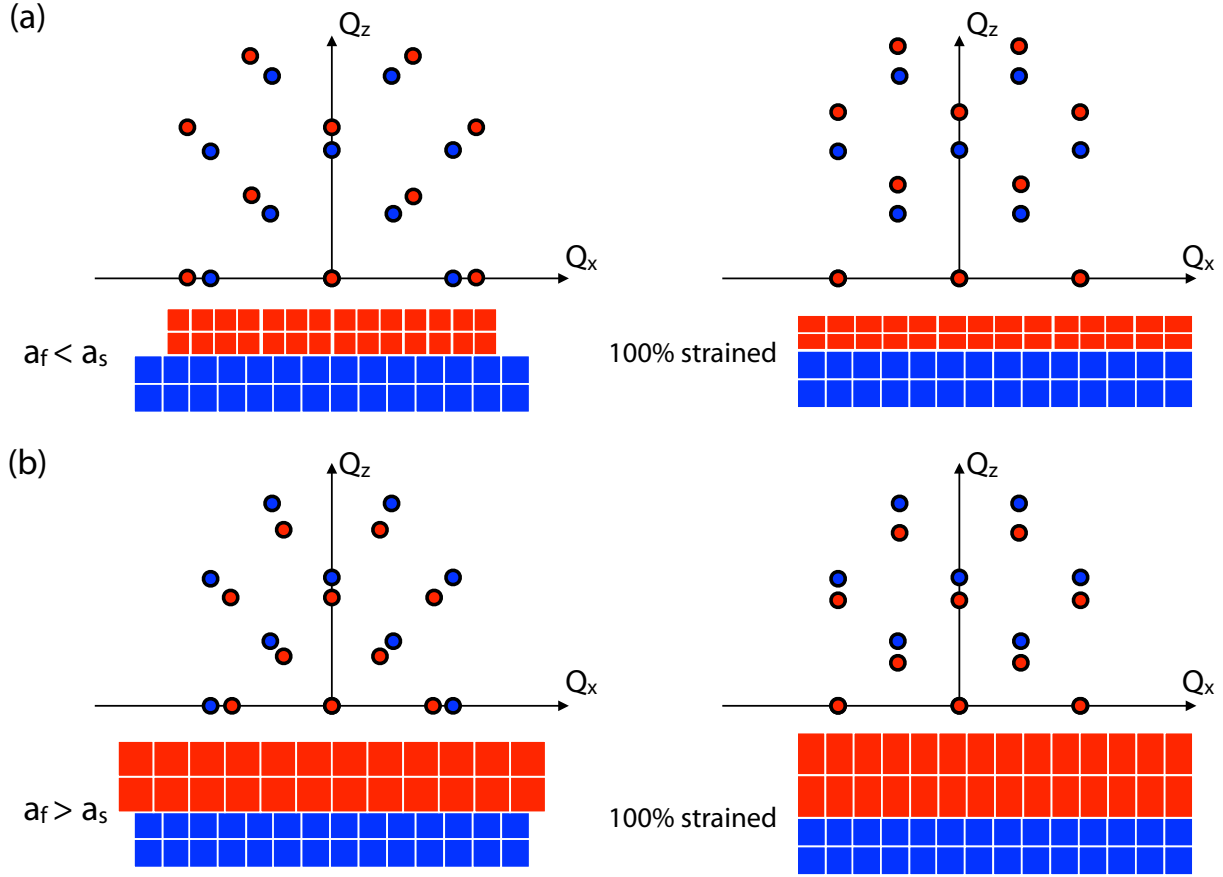
**$2\theta - \omega$  scan.** In this scan mode, the incident angle and the exit angle are maintained equal at all time so that the specular reflection condition is always satisfied, which fixes the direction of the scattering vector and only varies its length. The spacing  $d$  of the lattice planes parallel to the sample surface can be calculated by the Bragg equation:

$$2d \sin \theta = n\lambda \quad (2.4)$$

Where  $\lambda$  is the incident wavelength, and  $\theta$  is the Bragg peak position which equals half of the detector angle. The out-of-plane lattice parameter can be further calculated by choosing the proper Miller index. This technique also provides an indirect way of judging the strain state. By comparing the calculated lattice constant with unstrained bulk value, it is possible to investigate whether the strain is compressive or tensile, or relaxed. More interestingly, for a rather high quality epitaxial thin film, its Bragg peaks are typically surrounded by a series of lower-intensity oscillation peaks, known as the fringes. The total thickness  $t_f$  of the film can be determined from:

$$t_f = \frac{\lambda}{2|\sin \theta_n - \sin \theta_{n-1}|} \quad (2.5)$$

In which  $\theta_n$  and  $\theta_{n-1}$  are the peak positions of two neighboring fringes. In addition, there is a special scan mode where the incident angle is varying within a narrow range ( $\Delta\omega < 1^\circ$ ) while fixing the detector at the Bragg diffraction angle. This  $\omega$  scan, sometimes called “rocking curve” is performed to detect the presence of any mis-orientated or mosaic structure in the film. A FWHM of the rocking curve on the order of arc minute or less usually indicates a good single crystallinity.



**Figure 2.5:** Epitaxial strain status in both real and reciprocal space. (a) Tensile strain; (b) Compressive strain. In each case, the relaxed state is expressed on the left panel while the fully strained state is expressed on the right panel. Blue color stands for the substrate and red color stands for the film.

**Reciprocal space mapping (RSM).** RSM is the most straightforward approach to study the strain status and the in-plane and out-of-plane lattice parameters. In general, for a heteroepitaxial film which possesses the same or similar lattice structure with respect to the substrate, the strain state is expected to be either tensile, in which the in-plane lattice constant of the film is less than that of the substrate ( $a_f < a_s$ ), or compressive, in which the film has a larger in-plane constant than the substrate ( $a_f > a_s$ ). These two cases, together with the corresponding reciprocal space are sketched in Fig. 2.5. As seen, each spot stands for a reciprocal lattice point that can be probed with HRXRD by tuning sample  $\omega$ ,  $\Psi$ ,  $\Phi$ , and detector  $2\theta$  to satisfy the reflection condition. In real experiments, instead of mapping the entire reciprocal space, it is usually sufficient to map a small area around one specific reciprocal lattice vector with both in-plane ( $Q_x$ ) and out-of-plane ( $Q_z$ )

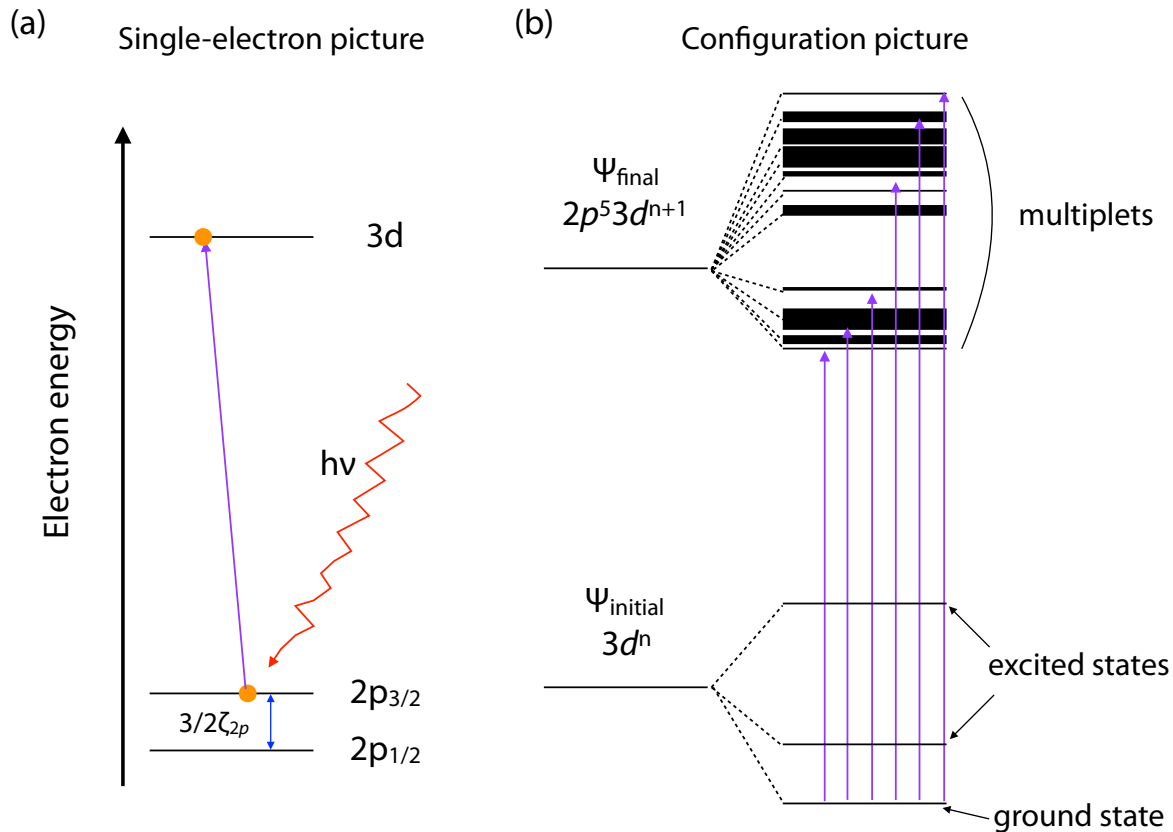
nonzero coordinates. When running the measurements, those parameters are first centered at the reflection condition of the substrate. Then a matrix scan of  $2\theta$  and  $\omega$  is performed, covering a reasonable area so that the reflection of the film is also included into the mapping. The coordinates in the reciprocal space are calculated by:

$$\begin{aligned} Q_z &= \frac{4\pi}{\lambda} \sin \theta \cos(\theta - \omega) = \frac{2\pi}{d_z} \\ Q_x &= \frac{4\pi}{\lambda} \sin \theta \sin(\theta - \omega) = \frac{2\pi}{d_x} \end{aligned} \tag{2.6}$$

And the lattice plane spacings  $d_x$ ,  $d_z$  in the real space can be obtained accordingly, which are proportional to the in-plane and out-of-plane lattice constant, respectively. Therefore RSM provides a quantitative characterizations on the strain states, the lattice parameters, and examines the epitaxial relationship between the film and the substrate.

**X-ray reflectivity (XRR).** Another highly useful technique based on HRXRD is XRR. Unlike other diffraction methods which mostly uncover crystallographic information, this technique is used to evaluate the parameters of thin films and heterostructures including thickness, density, surface and interface roughness. In a XRR experiment, the X-rays are incident on the sample surface at grazing angles. Due to the fact that the refractive index of a material in the X-ray region is slightly less than 1, total external reflection could take place when the incident angle is smaller than the critical angle  $\theta_c$ . The intensity of the reflected beams are identical to the incident beams for  $\theta < \theta_c$  whereas  $\theta > \theta_c$ , since the incident beams become capable of penetrating into the sample, it decays rapidly and is determined by the refractive index of material. In the case of heteroepitaxial thin films, interference occurs between the X-rays reflected from the surface and the interface of film and underlying substrate. This is featured by the presence of oscillations (also called Kiessing fringes) on the intensity decay of a XRR profile. Moreover, for multilayers and superlattices, since there are additional interfaces between different constituent layers, the interference is more complicated, giving rise to a variety of oscillations with individual amplitude and period on the profile.

This kind of measurement is done by recording the intensity of reflection as a function of  $2\theta/\omega$ . The scanning range is taken from below the critical angle to the angle where the reflection intensity drops to the level of background (typically from  $2\theta = 0^\circ \sim 0.2^\circ$  to  $4^\circ \sim 10^\circ$ ). Data analysis of XRR results is normally performed within the slab model fittings, in which the thickness and the density (or scattering length density) of each layer, together with the surface and interface roughness are established as the fitted parameters.



**Figure 2.6:** Interpretation of resonant X-ray absorption on the L<sub>2,3</sub> edges. (a) Single-electron picture and (b) Configuration picture.

Accurate values of these parameters will be achieved once a global best fit with respect to the experimental data is reached.

Apart from these measurements discussed above, some other HRXRD-based techniques such as X-ray pole figure and grazing incident X-ray scattering also play important roles in the structural characterizations of thin films. More details about our results will be given in the next chapter.

### 2.3 Resonant X-ray absorption spectroscopy

After discussing the deposition method and the structural characterizations, we turn to describing how to probe the electronic and magnetic properties. Resonant X-ray absorption spectroscopy (XAS) belongs to one of the most highly advanced approach which has been developed drastically over the last 30 years for this purpose. In this section, we will intro-

duce some of its basic principles and how to use this technique to achieve information such as valence state, orbital occupancy, spin configuration, and magnetic moment of thin film samples.

### 2.3.1 Basic principles

In general, resonant XAS is a type of element-specific core-level spectroscopy. There are two pictures proposed to illustrate its underlying mechanism, as displayed in Fig. 2.6. In the rather simplified “single-electron” picture (Fig. 2.6 (a)), the effect of electron-electron correlation is not taken into account. The photon energy of the incident X-rays is absorbed by a core-level electron and this electron is excited into an unoccupied state. Resonance takes place when the photon energy coincides with the interval between the core-level state and the unoccupied state, which is known as the absorption edge and determined by the specific binding energy in a material. Therefore, one of the great power of XAS is the elemental specificity as the absorption edge varies with different elements. The terminology of the absorption edge is defined according to the initial state of the electron. The main quantum number  $n$  is labeled alphabetically by capital letters starting from K (K, L, M, N ... stand for  $n = 1, 2, 3, 4 \dots$ ). Moreover, considering the spin-orbit splitting effect of the core-level states, the subshell of the electron is numbered from lower to higher energy positions. For example, as displayed in Fig. 2.6, the  $L_{2,3}$  edges represent the electrons excited from  $2p_{1/2}$  and  $2p_{3/2}$  levels, respectively (The  $L_1$  edge which represents the  $2s \rightarrow 3d$  transition, is not shown).

Even though the single-electron picture reveals the most fundamental features of XAS, it encounters troubles when the valence states are not fully empty. This is extremely common for compounds with  $d$  and  $f$  block elements, in which the many-body effects strongly modify the spectra and lead to multiplet structures. To correctly describe the XAS including these factors, the “configuration” picture (Fig. 2.6 (b)) is needed, where the absorption process is regarded as an atom excited from an initial configuration to a final configuration. For instance, the initial configuration  $\Psi_{initial}$  of a  $3d$  transition metal compound with  $n$  electrons ( $n = 1 \sim 9$ ) has an energetically favored ground state, whereas the final configuration  $\Psi_{final}$  contains many possible states, with or without degeneracy depending on the electron-hole interaction (exciton), Hund’s coupling, hybridization with ligands, and electron-electron correlation. As a result, while performing energy scans across the  $L_{2,3}$

edges, all those possible transitions will be detected and recorded on the spectrum. In addition, it is worth noting that temperature is another factor that is able to make the multiplet structure more complicated because at finite temperature, the initial configuration is a combination of the ground state and some low-lying thermal excited states.

According to the energy range under investigation, the absorption spectrum can be further separated into two regions. The wide range from about 50 eV after the absorption edge up to 1000 eV is called Extended X-ray absorption fine structure (EXAFS). In this region the ejected photoelectrons from the absorbing atom have a multiple scattering process with the surrounding atoms and the backscattered electron waves interfere with the forward-propagating waves. This phenomena give rise to a fine structure of oscillations on the spectrum. By analyzing the data with model simulations, one can obtain information about the type and distance of the neighboring atoms with respect to the central absorbing atom. The other region, from the rising edge up to around 100 eV, is called X-ray absorption new edge spectroscopy (XANES). Since this spectrum derives from the excitation of a core-level electron into the unoccupied state, it inversely reflects the electronic structures of the valence shell. The spectral lineshape, the peak position, and the multiplet structure are regarded as the fingerprint to reveal the chemical information of the absorbing atom and to extract effects arising from crystal field, lattice distortion or hybridizations with ligands. In this dissertation, our interest is mainly focused on the XANES region.

The absorption process from an initial state  $\Phi_i$  to a final state  $\Phi_f$  is quantitatively determined by the Fermi's golden rule. The corresponding transition probability  $W_{fi}$  is given by:

$$W_{fi} = \frac{2\pi}{\hbar} |\langle \Phi_f | T | \Phi_i \rangle|^2 \delta(E_f - E_i - \hbar\omega) \quad (2.7)$$

Where  $E_f$ ,  $E_i$ , and  $\hbar\omega$  are the energies of the final state, the initial state and the X-ray photons, respectively. The transition operator  $T$  originates from the interaction of light with an electron in solids. Within the first order approximation,  $T$  can be simplified as an electric dipole term [67]:

$$T \propto \vec{e}_q \cdot \vec{r} \quad (2.8)$$

In this equation,  $\vec{e}_q$  is the unit vector of the polarization direction of the photon electric field and  $\vec{r}$  is the position of electron. Expanding all of the wave functions and the operator in spherical harmonics, it has been noticed that some of the transition matrix ele-

ments vanish due to the orthogonality and parity relationship of spherical harmonics. If the states are written in the decoupled form  $|l, m_l, s, m_s\rangle$ , the difference on each parameter between the initial and the final state has to satisfy peculiar conditions to get non-zero transition probability. These conditions are called dipole selection rules [4]:

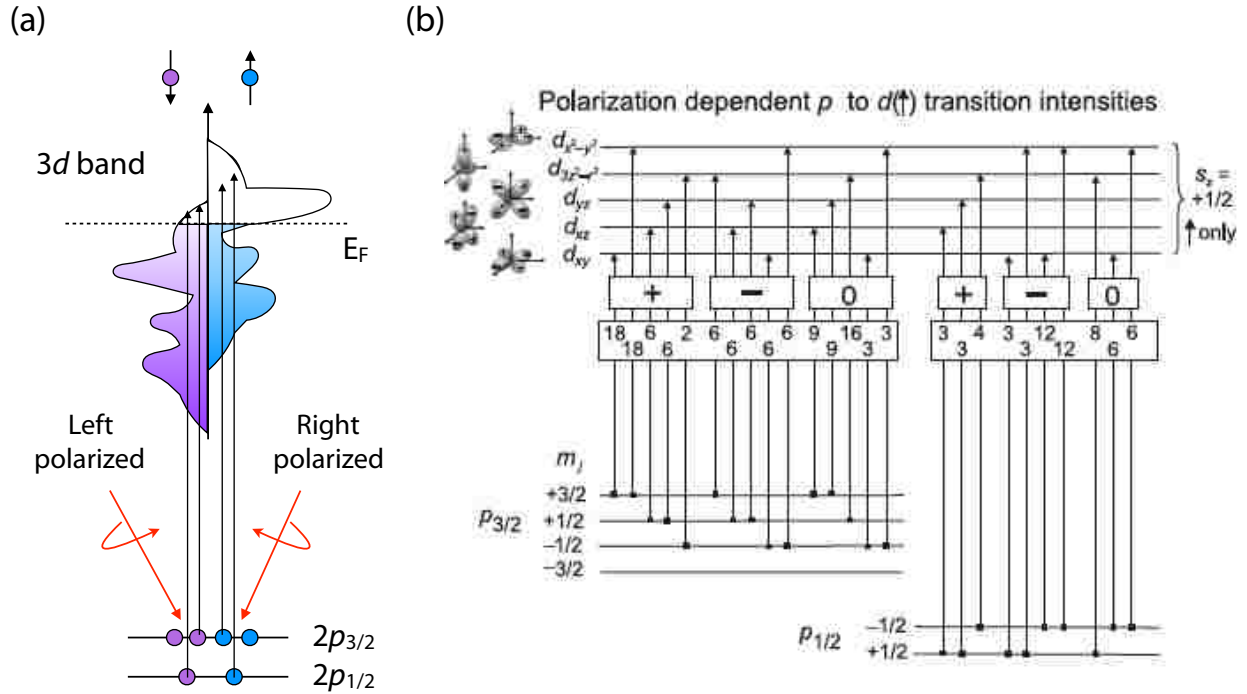
$$\begin{aligned}
 \Delta l &= l' - l = \pm 1; \\
 \Delta m_l &= m'_l - m_l = 0, \pm 1; \\
 \Delta s &= s' - s = 0; \\
 \Delta m_s &= m'_s - m_s = 0.
 \end{aligned}
 \tag{2.9}$$

For higher order approximations such as electric quadrupole term, the selection rules possess different forms. More details can be found in Ref. [68].

### 2.3.2 Polarization dependence

Another great power of XAS is that by tuning the polarization of the incident X-rays, the spectra will exhibit different features, which are microscopically related to the anisotropy of the charge or spin distribution in a material. This polarization dependent absorption is denoted as “dichroism”. For a nonmagnetic material, if there exists any anisotropic charge distribution, a distinct dichroism can be detected by using linearly polarized light. This is known as the X-ray natural linear dichroism (XNLD). In the case of a magnetic material, the anisotropic spin distribution due to magnetization gives rise to another type of important dichroism when measuring XAS with circularly polarized light — X-ray magnetic circular dichroism (XMCD). In what follows we will briefly introduce these two dichroism spectra.

For transition metal compounds, the five  $d$  orbitals under crystal field effect ( $d_{xy}$ ,  $d_{yz}$ ,  $d_{xz}$ ,  $d_{x^2-y^2}$ , and  $d_{3z^2-r^2}$ ) are all spherically asymmetric with strong anisotropy along different directions. In a XNLD measurement, the magnitude of the transition matrix element from a  $2p$  core state to individual  $d$  state is determined by the direction of the polarization vector. In general, the transition reaches the maximum when the polarization vector is along the orbital lobe and minimum if the vector falls onto the orbital nodal axis. Therefore, the direction of the polarization vector serves as a “search light” to sense the distribution of hole densities in the valence shell. For a fully empty  $3d$  shell, no XNLD is observed due to the equal integrated probability of each polarization. However, once the  $3d$  shell is partially occupied, the absorption intensity for a particular polarization can be severely

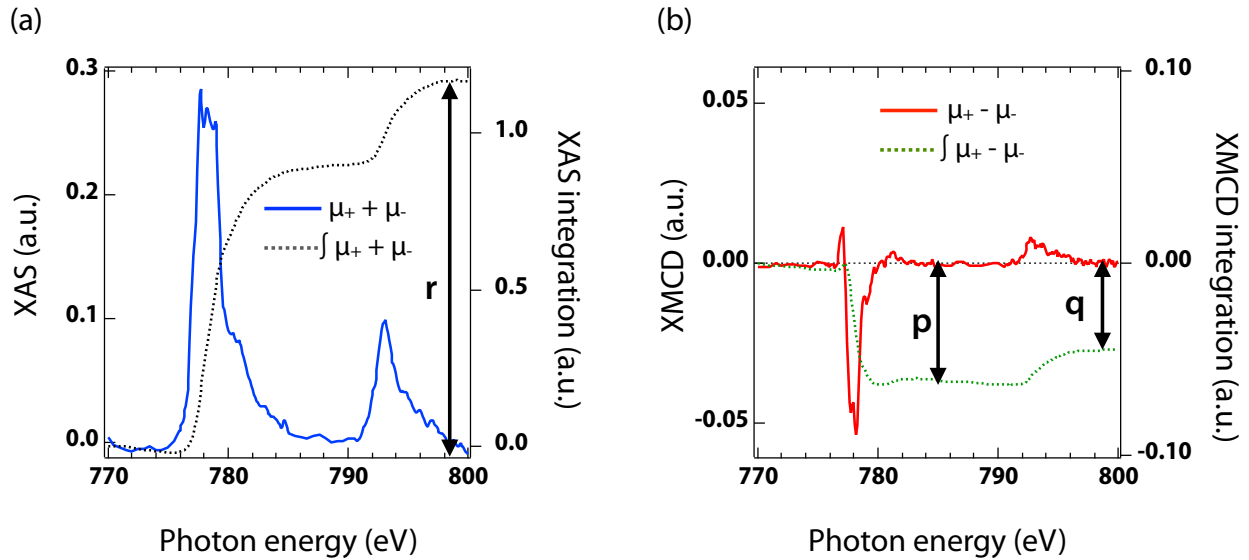


**Figure 2.7:** (a) Illustration of X-ray magnetic circular dichroism at the  $L_{2,3}$  edges of a  $3d$  transition metal compound. (b) Polarization dependence of the transition probabilities from  $2p$  core states to the spin-up  $3d$  valence states (reproduced from Ref. [4]). The + and - sign refer to the circularly polarized photon with helicity +1 and -1, whereas 0 refers to linearly polarized light.

suppressed since the hole densities along such polarization direction is quite small. In this way, XNLD uncovers essential information about orbital structure and orbital occupation of the absorption atom.

Compared with XNLD, XMCD is a more complicated phenomenon in which the angular momentum of the X-ray photons also needs to be considered. To explain the origin of XMCD, let's first consider this problem with an intuitive Stoner band model, which is depicted in Fig. 2.7 (a). In an external magnetic field, the valence band is split into a majority spin band and a minority spin band. When the left- and right-circularly polarized light interact with core-level electrons, the conservations of energy and angular momentum render that photons with a peculiar helicity can only excite electrons with the same type of spin polarization. Also, since spin-flip is not allowed under the dipole selection rules, an excited electron with spin-up only fills the holes in the spin-up band and vice versa. As a result, dichroism arises due to the imbalance between spin-up and spin-down holes in the





**Figure 2.8:** An example of (a) XAS ( $\mu_+ + \mu_-$ ) and (b) XMCD ( $\mu_+ - \mu_-$ ) spectra of the L edge of  $\text{Co}^{2+}$  ions, together with their integrated curves over energy. The symbols  $r$ ,  $p$ , and  $q$  labeled on the figures are the three definite integrals involved in the sum rule expressions.

valence band. Even though this model reveals some basic aspects of XMCD, it is not valid for any quantitative analysis. For this purpose, one must go back to study the probabilities of each transition. As shown in Fig. 2.7 (b), the polarization-dependent transition probabilities are summarized omitting the valence-shell spin-orbit interaction. Thanks to the core-level spin-orbit coupling effect, excitation probabilities are linked to both the polarization and the Clebsch-Gordon coefficients. Dichroism is calculated by summing up all possible transitions weighted by their probabilities under one polarization and subtracting the others, which reflects the imbalance in either spin or orbital angular momentum of the valence shell.

### 2.3.3 Sum rules

The net magnetic moment of an atom consists of a spin and an orbital contributions. According to theoretical derivations by Thole [69] and Carra [70], for a specific transition metal atom, these two parts can be extracted separately from XAS and XMCD spectra

using the so-called “sum rules”:

$$m_{orbital} = -\frac{4 \int_{L_3+L_2} (\mu_+ - \mu_-) d\omega}{3 \int_{L_3+L_2} (\mu_+ + \mu_-) d\omega} \times (10 - n_d) \quad (2.10a)$$

$$m_{spin} = -\frac{6 \int_{L_3} (\mu_+ - \mu_-) d\omega - 4 \int_{L_3+L_2} (\mu_+ - \mu_-) d\omega}{\int_{L_3+L_2} (\mu_+ + \mu_-) d\omega} \times (10 - n_d) \left(1 + \frac{7\langle T_z \rangle}{2\langle S_z \rangle}\right)^{-1} \quad (2.10b)$$

Where  $m_{orbital}$  and  $m_{spin}$  are the orbital and spin magnetic moments in units of  $\mu_B/\text{atom}$ . In these two equations,  $\mu_+$  and  $\mu_-$  stand for the XAS measured with right- and left-circularly polarized light, respectively.  $n_d$  is the electron occupation number of the outmost  $d$  shell.  $\langle T_z \rangle$  is the expectation value of the magnetic dipole operator. In most cases, the  $\langle T_z \rangle / \langle S_z \rangle$  term is small enough to be omitted (only few percentage correction). A more simplified expression of the sum rules have been summarized by Chen [71] using three symbols  $r$ ,  $p$ , and  $q$  to replace the three integrals, as shown in Fig. 2.8.

$$m_{orbital} = -\frac{4q}{3r} \times (10 - n_d) \quad (2.11a)$$

$$m_{spin} = -\frac{6p - 4q}{r} \times (10 - n_d) \quad (2.11b)$$

Sum rules have several advantages over other magnetometry such as SQUID or VSM. Firstly, since the XMCD measurement is element-specific, for materials with two or more magnetically active elements, it is capable of counting the net magnetic moment of individual element by applying sum rules on the corresponding spectra. Moreover, with the knowledge of these information, one can further speculate the microscopic magnetic structure, especially for antiferromagnetic and ferrimagnetic specimens. Last but not least, in the case of ultra-thin films and heterostructures, the magnetization from the sample is sometimes too weak for SQUID and VSM to detect, whereas XMCD is much more sensitive due to signal enhancement at the absorption edges.

### 2.3.4 Synchrotron radiation

It has to be noted that two requirements on the X-ray source are of the key importance for performing a successful XAS measurement. First, the energy of the X-rays should be continuously tunable in a wide range to cover the desired absorption edges. Second, the flux (number of photons per second) of the X-rays should be high enough ( $\sim 10^{19}$ ) to generate a clear spectrum in a reasonable period of time. Apparently, it is not possible to use a conventional laboratory X-ray tube (flux  $\sim 10^{10}$ ) as the source. To realize these goals,

synchrotron radiation sources have been built up and upgraded within the last forty years, which provide the most effective and reliable support these days.

In a synchrotron, electrons are generated and accelerated in a storage ring. A series of magnet devices (bending magnet and undulator) are mounted on the track of the ring. While the electrons are traveling through these devices, the direction of the beam will be changed due to the Lorentz force. Consequently a wide spectrum of radiation is formed, which contains many harmonics merging into a continuous spectrum from infrared to hard X-ray regions. In addition, with the combination of other optics including monochromator, slit, and polarization mirror, a series of beamlines can be separated and established for various purposes of usage.

After describing the synchrotron source, we switch to the detection mode. The most straightforward way of detecting the absorption spectrum is to measure the transmitted beam intensity  $I_t$  relative to the incident  $I_0$ . The absorption coefficient  $\mu$  is then proportional to  $-\ln(I_t/I_0)$ . However, this detection mode is limited to homogeneous samples only and the sample thickness has to be less than the X-ray penetration depth. In general, the transmission experiments are standard for hard X-rays and not suitable in the soft X-ray region (photon energy less than 1 keV). To solve this problem, yield methods have been discovered. During the decay of the core hole, the atom can generate either fluorescence photons or Auger electrons escaping from the sample. These secondary yields can be therefore recorded, the signals of which are proportional to the strength of absorption. By monitoring the photocurrent originating from the Auger electrons, which is referred to as total electron yield (TEY) detection mode, one can probe very close to the surface or buried interface due to the short escaping length (sensitive to a few nm beneath the surface). To probe the whole sample, one can record the fluorescence yield (FY) whose probing depth is  $\sim$  hundred nm. Furthermore, reflectivity detection mode is also available [72] as in some special situation (for example highly insulating ultrathin films), both TEY and FY signals are rather weak. However, as a scattering technique, the interference of light reflected from the surfaces of the film and the substrate would give rise to the skewed spectral lineshape, compared to those from other detection modes.

## 2.4 Polarized neutron reflectometry

Polarized neutron reflectometry (PNR) is developed as a means of probing the depth profile of magnetic thin films and multilayered structures on a nanometer scale [73, 74, 75, 76]. Up to date, PNR has been utilized to investigate phenomena as diverse as the magnetic depth profiles of thin films and heterostructures, the penetration of fluxoids in superconductors, and the emergent magnetic coupling at heteroepitaxial interfaces. In this section we will briefly describe the fundamental theory and the instrumentation of this technique.

### 2.4.1 Theory of neutron scattering in reflection geometry

Neutrons are spin-1/2 particles, and they have no net charge. Neutron reflectometry is often treated by regarding a neutron as a single particle and calculating the specular reflection amplitude based on the quantum mechanical scattering theory. For a magnetic material, the net scattering potential has two origins: the nuclear scattering potential  $V_n$ , and the magnetic scattering potential  $V_m$ .  $V_n$  is expressed as:

$$V_n = \frac{2\pi\hbar^2}{m}\rho_n(x) \quad (2.12)$$

where  $\rho_n(x)$  is the nuclear scattering length density (SLD) in unit of  $\text{\AA}^{-2}$ . If the material is composed of multiple elements,

$$\rho_n(x) = \sum_i N_i b_i \quad (2.13)$$

where the summation is over all distinct species and  $N_i$  and  $b_i$  are the number density and the scattering length for the  $i$ -th species. Moreover, within a source of magnetic field,  $V_m$  is related to the neutron magnetic moment  $\boldsymbol{\mu}$  and the magnetic induction  $\mathbf{B}$ :

$$V_m = -\boldsymbol{\mu} \cdot \mathbf{B} \quad (2.14)$$

in which  $\boldsymbol{\mu} = \mu_n \boldsymbol{\sigma} = -1.913\mu_N \boldsymbol{\sigma}$  ( $\mu_N$  is the nuclear magneton and  $\boldsymbol{\sigma}$  is the Pauli matrices). Since the observed reflectivity curve is generated only due to the scattering potential differences between materials, thus the uniform external field doesn't contribute to  $V_m$ .

The induction  $\mathbf{B}$  here is equal to the magnetization of the material  $\mathbf{M}$ .

One can expand the Pauli matrices and express the total scattering potential in the matrix notation:

$$V = V_n + V_m = \frac{2\pi\hbar^2}{m_n} \begin{bmatrix} \rho_n & 0 \\ 0 & \rho_n \end{bmatrix} - \mu_n \begin{bmatrix} M_z & M_x - iM_y \\ M_x + iM_y & -M_z \end{bmatrix} \quad (2.15)$$

It is furthermore convenient to define magnetic SLD  $\boldsymbol{\rho}_m$  so that equation 2.15 can be rewritten in a simpler way:

$$V = \frac{2\pi\hbar^2}{m_n} \begin{bmatrix} \rho_n + \rho_{mz} & \rho_{mx} - i\rho_{my} \\ \rho_{mx} + i\rho_{my} & \rho_n - \rho_{mz} \end{bmatrix} \quad (2.16)$$

where

$$\boldsymbol{\rho}_m = -\frac{m_n}{2\pi\hbar^2} \mu_n \mathbf{M} = C \sum_i N_i \boldsymbol{\mu}_i \quad (2.17)$$

$N_i$  is the number density and  $\boldsymbol{\mu}_i$  is the magnetic moment of the  $i$ -th species per formula unit of the measured sample, in unit of  $\mu_B$ .  $C = 2.645 \times 10^{-5} \text{ \AA} / \mu_B$  in this case.

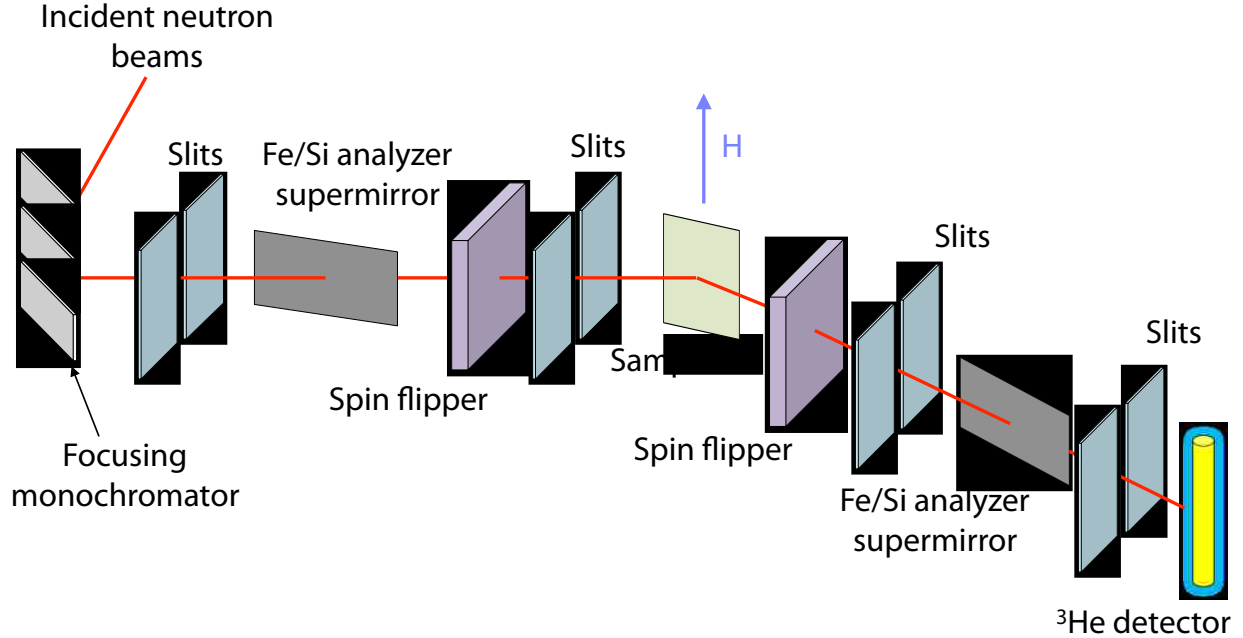
To link the theory to real experimental variables, we first rename the four SLD matrix elements:

$$\begin{aligned} \rho_{++} &= \rho_n + \rho_{mz} \\ \rho_{--} &= \rho_n - \rho_{mz} \\ \rho_{+-} &= \rho_{mx} - i\rho_{my} \\ \rho_{-+} &= \rho_{mx} + i\rho_{my} \end{aligned} \quad (2.18)$$

When a polarized neutron beam (spin-up “+” or spin-down “-”) is scattered across the sample interface, the spin of the reflected beam can be either non-flipped or flipped. As a result, there are two non-spin-flip reflectivity curves,  $R_{++}$  and  $R_{--}$ , together with two spin-flip ones,  $R_{+-}$  and  $R_{-+}$ . Each of these four quantities is determined by its corresponding SLD matrix element, respectively. While performing a PNR experiment, both the non-spin-flip and the spin-flip reflectivity curves are recorded. Then one needs to establish model fittings to simulate the data sets, using  $\rho_{++}$ ,  $\rho_{--}$ ,  $\rho_{+-}$ , and  $\rho_{-+}$  as the fitting parameters. The magnetic SLD profile (and based on equation 2.17, the associated magnetic moment of the sample) can be further obtained with the knowledge of the nuclear SLD profile.

## 2.4.2 Instrumentation

Fig. 2.9 is a sketch of a typical PNR station. The monochromator and the slits before and after the sample confine the neutron beam with a relatively narrow angular divergence in



**Figure 2.9:** Sketch of the polarized neutron reflectometry station. The incident monochromatic unpolarized beam is polarized by the first supermirror in transmission mode. The spin flippers can switch the neutron polarization from down to up and vice versa. The second supermirror is used to analyze the polarization state of neutrons after scattering.

the reflection plane, which provides good instrumental  $Q$  resolution (The vertical divergence, even though still not small, will not affect the resolution on a large scale). Similar to XRR, in a reflectivity scan, the detector position  $2\theta$  is locked twice as much as the grazing incident angle  $\omega$  and the reflected beam intensity is recorded as a function of  $\omega$ . This corresponds to a single nominal value of wave vector transfer  $Q$ . The supermirrors together with the spin flippers are inserted into both the incident and reflected paths for offering a polarized neutron beam before the sample and for analyzing the polarization state after the scattering process. By tuning each spin flipper to a specific status, those four reflectivity curves,  $R_{++}$ ,  $R_{--}$ ,  $R_{+-}$ , and  $R_{-+}$  can be measured separately. In order to explore more details about SLD features along the epitaxial growth direction, it is necessary to know the relation between the spacial resolution and the wave vector transfer  $Q$ . In general, to distinguish variations of SLD over a length  $L$ , one has to measure the reflectivity up to  $Q \sim 2\pi/L$  [76].

In this dissertation, the PNR experiments are performed at the beamline PBR of the Na-

tional Institute of Standards and Technology (NIST). The samples are mounted in a closed-cycle refrigerator, which has a temperature range of 5 K – 350 K with a tunable external magnetic field up to 0.7 T. More details about experiential results and model fittings can be found in the next few chapters.

## Chapter 3

### Metallic interface in non-SrTiO<sub>3</sub> based titanate superlattice

This chapter mainly follows the content in my first-author paper published in 2014 [77]. In this chapter, we report on the fabrication of all perovskite Mott insulator/band insulator YTiO<sub>3</sub>/CaTiO<sub>3</sub> superlattices by pulsed laser deposition. The combination of *in-situ* reflection high energy electron diffraction, X-ray diffraction and X-ray reflectivity confirms the high quality of the films grown in a layer-by-layer mode. Electrical transport measurements reveal that a non-SrTiO<sub>3</sub> based two-dimensional electron gas system has formed at the YTiO<sub>3</sub>/CaTiO<sub>3</sub> interface. These studies offer another route in the pursuit of complex oxide two-dimensional electron gas systems which allows to obtain greater insights into the exotic many-body phenomena at such interfaces.

#### 3.1 Introduction

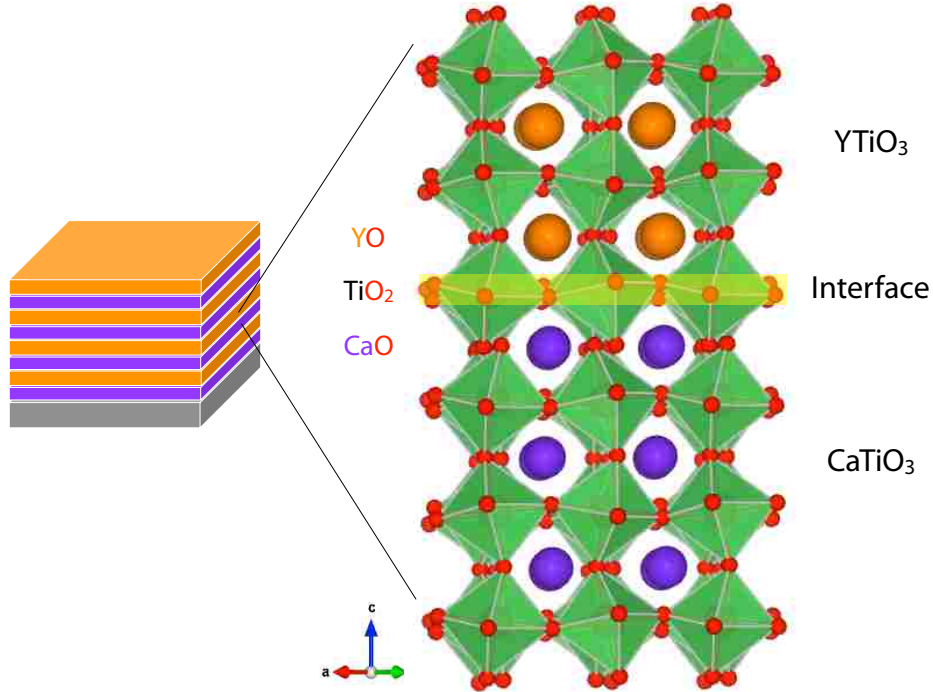
In recent years two-dimensional electron gases (2DEGs) at the interface of complex insulating oxide heterostructures have attracted tremendous research interest because of the observed emergent physical phenomena as well as the potential device applications [78, 79, 80, 81, 82, 83]. While a large number of perovskite based heterostructures have been discovered experimentally so far [84, 85, 86, 87, 88, 89, 90, 91], all of these systems contain layers of quantum paraelectric SrTiO<sub>3</sub> (STO) [92] except for the notable LaTiO<sub>3</sub>/KTaO<sub>3</sub> [91]. Among these STO-based systems, specifically for the *RTiO<sub>3</sub>/SrTiO<sub>3</sub>* (*R* represents a trivalent rare-earth ion) family, it was pointed out that the interfacial electronic properties and magnetism can be effectively tailored by the specific choose of *R* [88, 93, 94, 95]. Based on this, it can be conjectured that similar behavior can be achieved by substituting Sr with a divalent *alkaline* earth ion, *A* in *RTiO<sub>3</sub>/ATiO<sub>3</sub>* superlattices [96]. Up to date, however, there is no experimental information on whether any *RTiO<sub>3</sub>/ATiO<sub>3</sub>* interface outside of STO support metallic ground state.

Here we report on the fabrication of ultra-thin perovskite 3YTiO<sub>3</sub>/6CaTiO<sub>3</sub> (3 and 6 refers to the pseudocubic unit cell) superlattice on NdGaO<sub>3</sub> (110) substrate, which exhibits a 2DEG *without* STO. The schematic structure of the superlattice is displayed in Fig. 3.1. In the bulk, orthorhombic YTiO<sub>3</sub> (YTO) is a  $3d^1$  Mott insulator (Mott gap  $\sim 1.2$  eV [97])



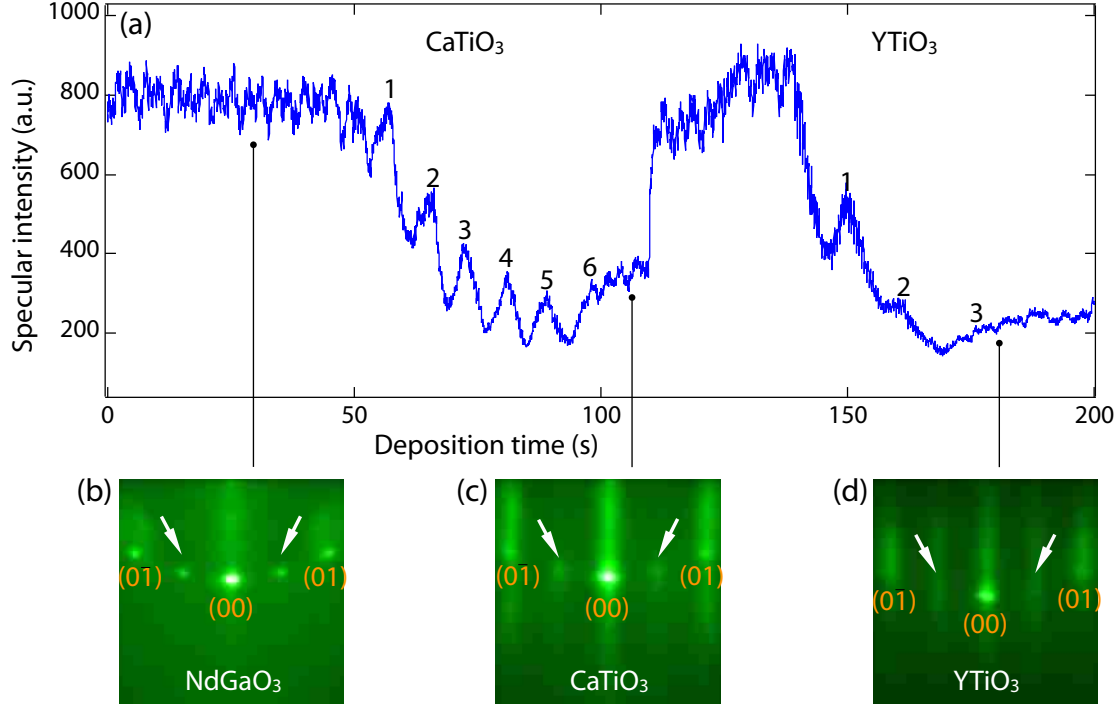
**Table 3.1:** Lattice parameters of bulk CTO, YTO and NGO. The  $a$ ,  $b$  and  $c$  represent the values of the orthorhombic unit cell while the  $a_c$ ,  $b_c$  and  $c_c$  stand for the pseudocubic unit cell.

Material	$a$ (Å)	$b$ (Å)	$c$ (Å)	$a_c = b_c = \sqrt{a^2 + b^2}/2$ (Å)	$c_c = c/2$ (Å)
CTO	5.380	5.442	7.640	3.826	3.820
YTO	5.316	5.679	7.611	3.889	3.806
NGO	5.428	5.498	7.708	3.863	3.854



**Figure 3.1:** Schematic of the YTO/CTO superlattices along the  $[001]$  pseudocubic growth direction. The crystal structure at one of the interface is highlighted.

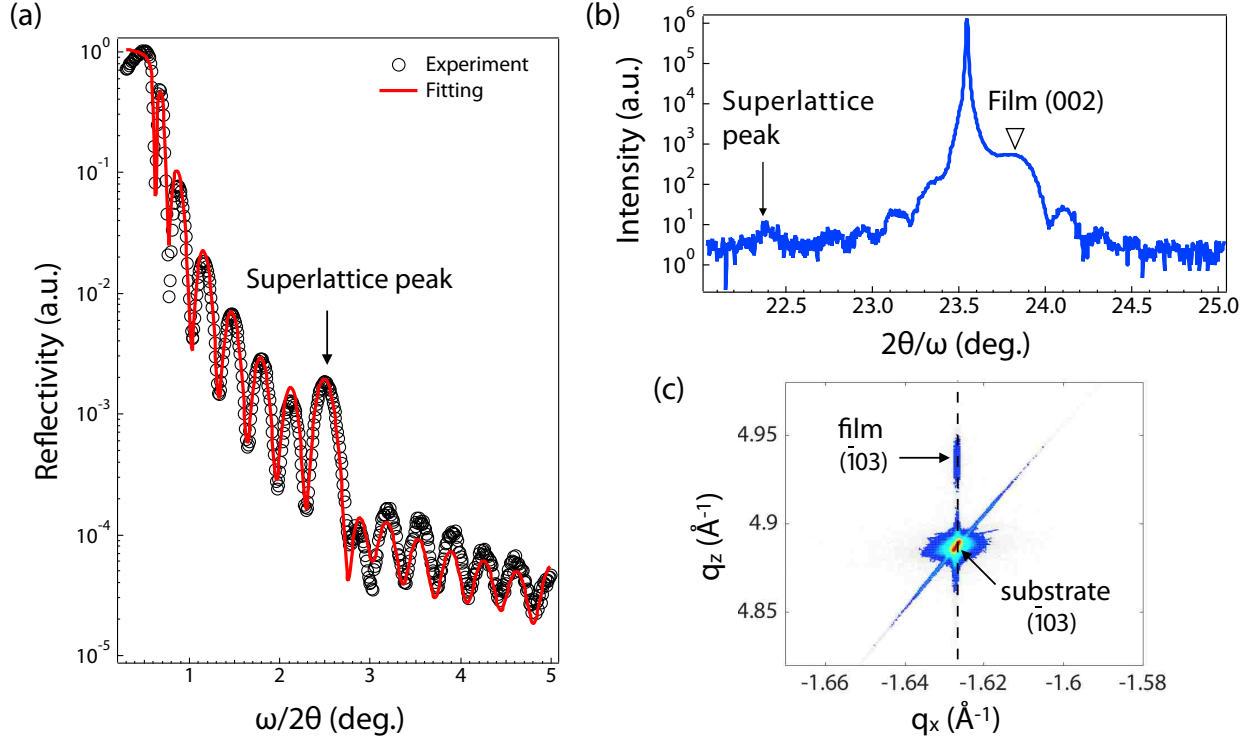
that undergoes the para- to ferro- magnetic phase transition at 30 K [98] while orthorhombic  $\text{CaTiO}_3$  (CTO) is a  $3d^0$  diamagnetic band insulator with an energy gap of  $\sim 3.5$  eV [99, 100]. (110)-oriented orthorhombic  $\text{NdGaO}_3$  (NGO) is selected as the substrate because it offers the symmetry continuity and small lattice mismatch with the film, as shown in Table 3.1. The entire growth process was monitored by *in-situ* reflection high energy electron diffraction (RHEED) demonstrating good crystallinity and smooth surface morphology. X-ray diffraction (XRD) and X-ray reflectivity (XRR) establish the epitaxial growth of the superlattice with abrupt interface. Transport measurements reveal the superlattices exhibit metallic conduction from 300 K down to 2 K with electrons as the carriers.



**Figure 3.2:** (a) RHEED intensity of the specular reflection as a function of deposition time. (b)–(d) *In-situ* RHEED patterns of (b) NGO (110) substrate, (c) CTO layers and (d) YTO layers. The observed half orders indicated by white arrows are from the orthorhombic (001) reflections.

### 3.2 Experiment

A set of 3YTO/6CTO superlattices was fabricated by pulsed laser deposition using a KrF excimer laser operating at  $\lambda = 248$  nm. During the growth, the NGO substrate was kept at 750 °C in a high-vacuum atmosphere of  $10^{-6}$  Torr to avoid the formation of  $Y_2Ti_2O_7$  impurity phase [98]. The laser fluency and pulse repetition rate were set at about  $1.4$  J/cm<sup>2</sup> and 2 Hz, respectively. After growth samples were cooled down to room temperature without annealing at a rate of 15 °C/min. Structural properties of the sample were characterized by X-ray Diffraction (XRD) and X-ray Reflectivity (XRR) measurements (Cu  $K_{\alpha 1}$  line,  $\lambda = 1.5406$  Å). The electrical transport properties were performed by a Physical Property Measurement System (PPMS, Quantum Design) using the Van der Pauw geometry. The Hall effect measurements were carried out in an external magnetic field of up to 7 T oriented normal to the sample surface.



**Figure 3.3:** (a) X-ray reflectivity data of the  $[3\text{YTO}/6\text{CTO}]_7$  superlattice. Total thickness of the superlattice calculated according to the Kiessig fringes is about 24 nm. (b) X-ray diffraction  $2\theta$ - $\omega$  scan. The film (002) peak and the superlattice satellite peak are labeled on the graph. (c) Reciprocal space mapping around the  $(\bar{1}03)$  reflection of the sample.  $q_x$  and  $q_z$  represent the in-plane and out-of-plane reciprocal lattice vectors, respectively.

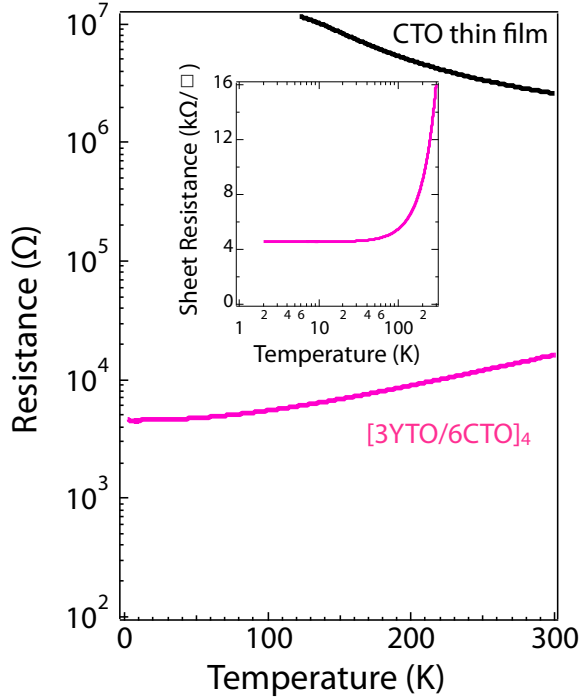
### 3.3 Results and Discussions

Fig. 3.2 (a) presents the RHEED intensity of the specular reflection as a function of deposition time fulfilling the growth of one periodicity (6CTO + 3YTO). For both components, when the laser ablation is taking place, the RHEED intensity exhibits a distinct oscillation behavior, which is the hallmark of two-dimensional (2D) layer-by-layer growth mode as discussed in the previous chapter. The completion of an oscillation indicates that one monolayer (in this case one unit cell) has been formed with full coverage of the former layer. Therefore the number of oscillations is counted to estimate the total thickness of the film. In the meanwhile, more information about the in-plane crystal structure and the lattice symmetry is reflected by the *in-situ* RHEED patterns. We show three typical images in Fig. 3.2 (b)–(d).

Fig. 3.2 (b) is the RHEED pattern of the NGO (110) substrate before growth. As seen,

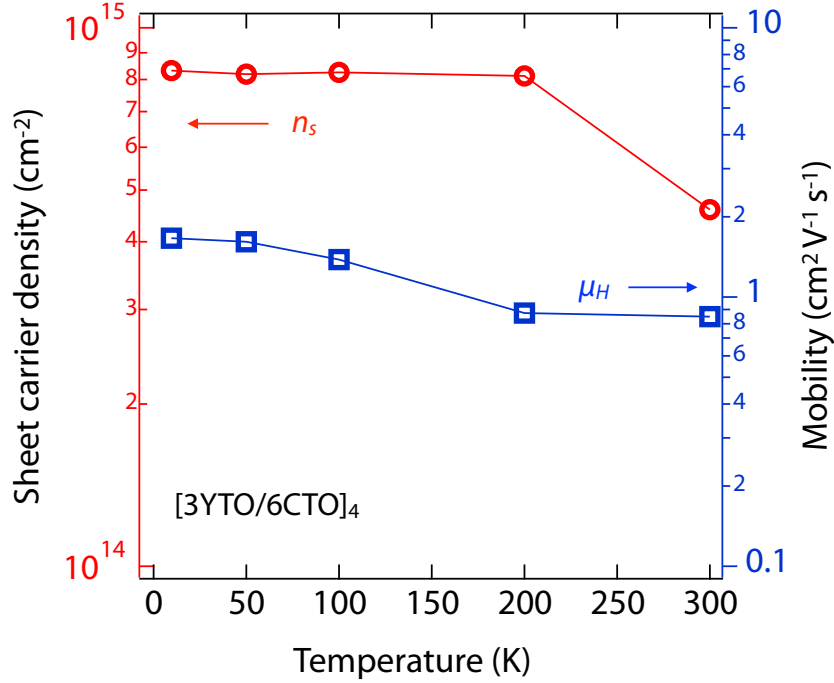
the characteristic specular (0 0) and off-specular (0  $\pm$ 1) Bragg reflections on the first Laue circle testify for the smooth morphology of the substrate. It is worth noting that for a NGO (110) substrate, the orthorhombic *c*-axis lies in the plane of the surface, about twice as much as its orthogonal axis [see Table 3.1]. These give rise to a rectangular surface unit cell instead of cubic. Therefore the half orders indicated by the white arrows are due to the orthorhombic (001) reflections [101]. During the alternating deposition of CTO and YTO layers, the distinct spots from specular and off-specular reflections with the characteristic streak pattern shown in Fig. 3.2 (c) and Fig. 3.2 (d) were observed, which confirm both good crystallinity and smooth morphology of the superlattice. Importantly, the half order reflections were still observed after cooling the sample down to room temperature, indicating that the superlattice preserves the orthorhombic symmetry.

More comprehensive information about the superlattice thickness as well as the surface and interface roughness can be extracted from XRR measurements. The best model fitting of the experimental reflectivity data, as shown in Fig. 3.3 (a) yields the total film thickness of  $\sim 25.16$  nm which is in excellent agreement with that estimated from the RHEED oscillations. The average interface and surface roughness are about 3 Å and 5 Å, respectively. Moreover, the superlattice peak as marked on the graph stands out of the other fringes clearly, offering another strong evidence that the superlattice periodicity has been well established. All of these results confirm that the resultant superlattices have perfect crystallinity with the abrupt interfaces and smooth surface. In addition to morphological quality, it is of critical importance to ensure that the superlattices contain no impurity phase. To investigate this, we performed the XRD  $2\theta$ - $\omega$  scans in the vicinity of the NGO (002) reflection on a [3YTO/6CTO]<sub>7</sub> sample. As displayed in Fig. 3.3 (b), besides the film (002) reflection at  $\omega = 23.826^\circ$  on the right side of the sharp substrate peak, the first order superlattice peak is also observed at  $\sim 22.389^\circ$ . These yield a thickness of 33.39 Å for one superlattice periodicity (3YTO + 6CTO) that is very close to the expected value of 34.35 Å. Also the total thickness of the sample estimated from the Kiessig fringes is about 25.24 nm, which agrees very well with the value from XRR fittings. Last but not least, the status of the biaxial strain effect was testified by performing reciprocal space mapping (RSM) around the off-specular ( $\bar{1}03$ ) Bragg reflection of the substrate. As seen in Fig. 3.3 (c), the relatively weak ( $\bar{1}03$ ) reflection of the film has the same in-plane reciprocal lattice vector as the substrate. This confirms that films up to  $\sim 26$  nm is coherently strained to the substrate.



**Figure 3.4:** Temperature dependence of the resistance of a 3YTO/6CTO superlattice (purple curve) and a 10 nm thick CTO film (black curve). Inset: Sheet resistance of the superlattice vs. temperature in the log scale. Note, temperature is plotted in the log scale to show the absence of any upturn behavior down to 2 K.

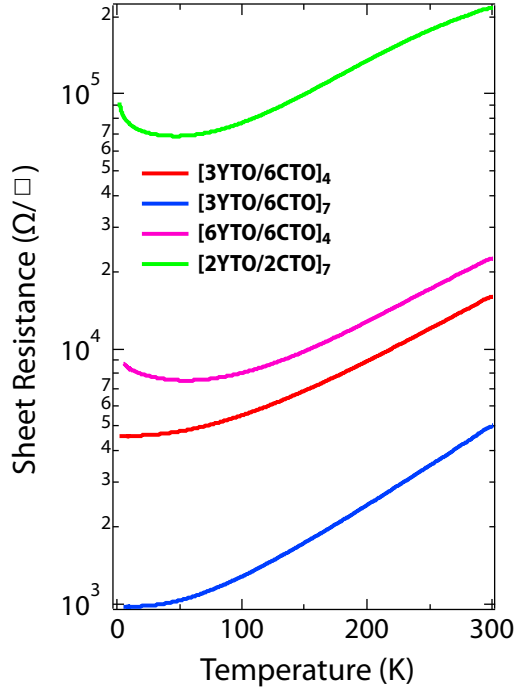
Having confirmed the high structural quality of the samples, we turn to explore the electrical transport properties of the superlattice. As seen in Fig. 3.4, the resistance of the superlattice (purple curve) exhibits distinct metallic behavior in the whole temperature range, i.e. it decreases continuously as the temperature is lowered down to the base temperature. The inset in Fig. 3.4 presents the corresponding temperature-dependent sheet resistance per YTO/CTO interface. In order to assure that the metallic behavior is due to the interface and elucidate the possible role of defect or oxygen doping, we performed the same measurements on two reference samples: 10 nm thick CTO on NGO and 10 nm thick YTO on NGO, both fabricated under the identical growth conditions as the superlattices. As immediately seen in Fig. 3.4, the 10 nm thick CTO film shows a strongly insulating behavior (black curve) until its resistance goes out of the measurable range at around 120 K; at the same time the resistance of 10 nm thick YTO film is even beyond the measurement range of our apparatus starting from the room temperature. By comparing the superlattices with these reference samples it allows to confirm that the observed metallic conduc-



**Figure 3.5:** Sheet carrier density and mobility of 3YTO/6CTO superlattices as a function of temperature.

tivity of the superlattices indeed emerges from the YTO/CTO interfaces. Furthermore, it is worth noting that YTO/STO superlattice was reported to be insulating [102] which corroborates the essence of the combination of YTO and CTO.

To investigate the type of charge carries and estimate the carrier density we performed the Hall resistivity measurements. The obtained Hall resistance data exhibits linear relationship with the applied magnetic field and shows a negative slope,  $R_H$  implying that electron is the type of charge carriers in the superlattices. This strongly indicates the existence of interfacial electron transfer from  $\text{Ti}^{3+}$  in YTO to  $\text{Ti}^{4+}$  in CTO. The conducting electrons likely reside on the CTO side, which is consistent with a recent theoretical calculation considering band alignments between various oxides including YTO and CTO [103]. The calculated sheet carrier density  $n_s$  as a function of temperature is shown in Fig. 3.5, left axis. As seen, the magnitude is  $\sim 10^{14} \text{ cm}^{-2}$  and is practically a constant with gradual increase towards lower temperatures. The obtained value is quite similar to the previously reported 2DEG systems [85, 90, 91, 89]. Furthermore, the corresponding Hall mobility  $\mu_H$  is also plotted in Fig. 3.5 as a function of temperature, right axis. As seen, at 300K  $\mu_H$  has the same magnitude as other STO-based systems but at 10 K  $\mu_H$  sharply decreases



**Figure 3.6:** Temperature dependence of the sheet resistance of  $[m\text{YTO}/n\text{CTO}]_N$  superlattices.  $m$  and  $n$  represent the pseudocubic unit cell of YTO and CTO, respectively.  $N$  stands for the total number of superlattice periodicity.

to  $\sim 2 \text{ cm}^2\text{V}^{-1}\text{s}^{-1}$ , which is about two orders of magnitude smaller than in STO-based 2DEGs [85, 90, 89]. The origin of reduced mobility could be connected to several scattering mechanisms, which dominate at different temperature: ionic impurity scattering (low temperature), electron-electron scattering (intermediate) and longitudinal optical phonon scattering (high temperature) [104, 105]. The strong suppression of  $\mu_H$  at low temperature in YTO/CTO is possibly due to the combination of scattering from defects present at the interface and large crystal field distortion at the YTO/CTO interface which should give rise to a strongly enhanced ionic impurity scattering.

It should be noted that according to Y. Nishihara et al. [106], Ca doped  $\text{Y}_{1-x}\text{Ca}_x\text{TiO}_3$  powders with Ca content  $x \sim 0.3$  can also have metallic behavior. Therefore, it is of critical importance to carefully exclude that the conductance observed in YTO/CTO doesn't originate from unwanted  $\text{Y}_{1-x}\text{Ca}_x\text{TiO}_3$  phase due to intermixing at the interface. For this purpose, apart from the XRR results which already confirm the superlattices have abrupt interfaces, electrical transport characterizations of YTO/CTO superlattices with different sequences and thicknesses are exhibited in Fig. 3.6. As mentioned by Y. Nishihara

et al., the solid solution  $Y_{1-x}Ca_xTiO_3$  in its metallic phase always have a Fermi-liquid (FL) behavior independent of the doping compositions. However, as seen in Fig. 3.6, while the  $[3YTO/6CTO]_4$  and the  $[3YTO/6CTO]_7$  superlattices do present a FL behavior, the  $[2YTO/2CTO]_7$  and the  $[6YTO/6CTO]_4$  samples show a clear non-FL behavior with a small upturn (weak localization) at low temperature. In addition, very similar phenomena, i.e. the formation of non-FL 2DEG as a function of thickness has been reported by S. Stemmer et al. in another rare-earth/alkaline-earth titanate  $SmTiO_3/SrTiO_3$  heterostructures [107] and is not attributed to intermixing effect. While the precise microscopic origin of such behavior is still under investigation, the observed non-FL metallic conduction in YTO/CTO superlattices provides strong evidence that it is not related to the formation of  $Y_{1-x}Ca_xTiO_3$  phase at the interface.

### 3.4 Summary

In summary, we have fabricated the non-STO based ultra-thin 3YTO/6CTO superlattices on NGO (110) substrate exhibiting 2DEG behavior. A combination of RHEED, XRD and XRR measurements confirms the high-quality layer-by-layer growth of the films with smooth surface morphology and sharp interfaces. Transport measurements reveal that the superlattices exhibit metallic conduction from 300 K to 2 K with electrons as the charge carriers. Our findings suggest another route to realizing complex oxide 2DEGs without hindering effects from complex behavior of STO and provides a system to investigate possible interplay between magnetism and superconductivity at the interface.



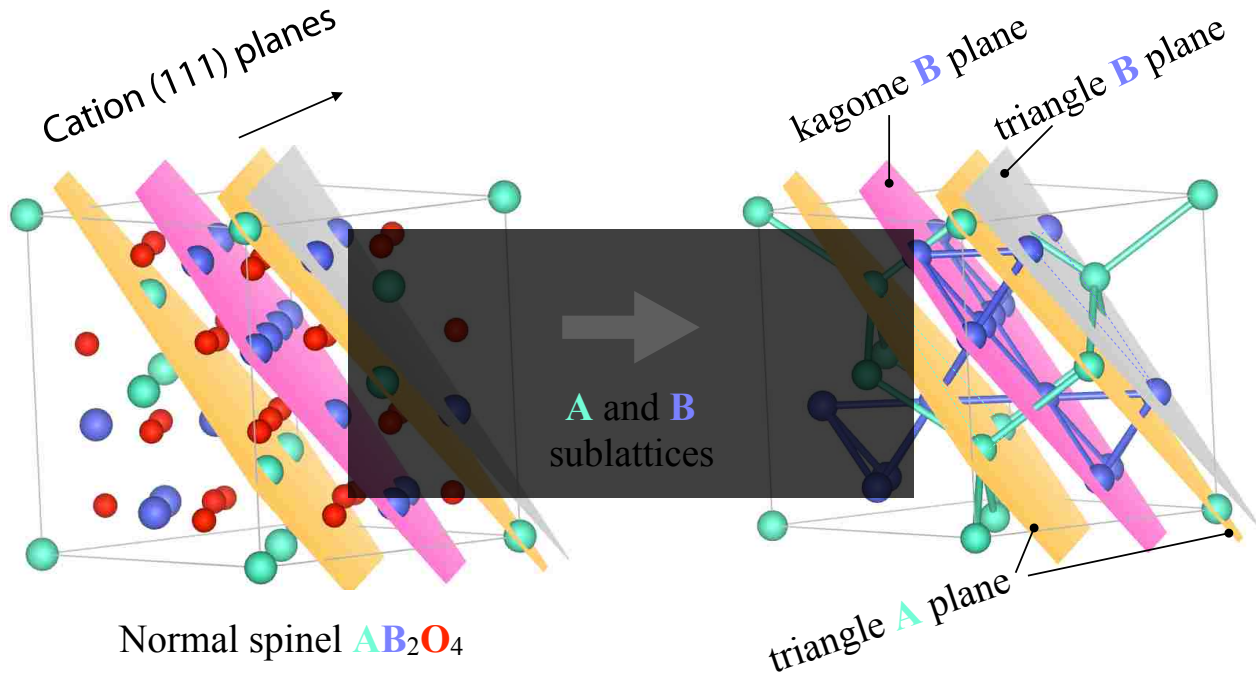
## Chapter 4

### Epitaxial growth of (111)-oriented spinel oxide thin films and heterostructures

This chapter includes the main contents published in [53] and [108], for which I am the first author. In this chapter we will discuss in details about the fabrications (111)-oriented  $\text{CoCr}_2\text{O}_4$  (CCO) thin films and heterostructures, an experimental realization of the “geometrical lattice engineering” (GLE) concept as proposed in the introduction chapter. For the first step, the growth condition of CCO is optimized by means of *in-situ* reflection-high-energy-electron-diffraction (RHEED). Structural characterizations using atomic force microscopy (AFM), X-ray diffraction (XRD) and X-ray reflectivity (XRR) demonstrate the expected (111) orientation with sharp interface and smooth surface morphology. X-ray photoemission spectroscopy (XPS) and X-ray absorption spectroscopy (XAS) reveal no disorder in the cation distribution or multivalency present in the samples. In addition, *dc* magnetization and X-ray magnetic circular dichroism (XMCD) measurements indicate a bulk-like magnetic behavior. For the second step, we show the fabrication of ultra-thin (111) CCO films using  $\text{Al}_2\text{O}_3$  (AlO) as the spacer. As a result, a set of novel quasi-two-dimensional (quasi-2D) frustrated lattices composed of alternating kagomé and triangular ionic planes is artificially established in these CCO/AlO superlattices.

#### 4.1 Introduction

Over the past several decades, a variety of geometrically frustrated magnetic systems including spin ice, spin glass and spin liquid have been studied as one of the most popular topic in condensed matter physics [109, 110, 111, 112, 113, 114]. In such systems, the exchange interaction between nearest neighbor ions is typically antiferromagnetic (for spin ice, the exchange interaction is ferromagnetic) and the peculiar geometries of the lattices (triangular and kagomé lattice for the 2D case, or pyrochlore and hyper-kagomé lattice for the 3D case) render the magnetic bonds impossible to be satisfied simultaneously. These geometrically frustrated lattices, especially the 2D ones have an excellent potential to host various exotic phenomena such as quantum spin liquid, topological phases, kinetic ferromagnetism, and chiral superconducting state to list a few [45, 115, 116, 117]. The fabrication of a 2D geometrically frustrated lattice, however, has proven to be rather challenging.



**Figure 4.1:** The conventional unit cell of a normal spinel structure. The corresponding  $(111)$  ionic planes are marked on the figure. Note, the A ionic planes only form the triangular planes, while the B ionic planes form both the triangular and the kagome planes.

For example, even though several metal-organic hybrid counterparts were synthesized by chemical methods, structural disorder and strong lattice distortions remained a persistent hindrance [118, 119]. Alternatively, the GLE approach which is generally described in the Introduction chapter offers a promising way to generating such lattices by growing ultra-thin spinels along the  $[111]$  crystallographic axis, as shown in Fig. 4.1.

First we recap that the general chemical formula of the spinel structure can be written in  $A_{1-\delta}B_\delta[A_\delta B_{2-\delta}]O_4$ . When  $\delta = 0$ , it is known as the normal spinel  $AB_2O_4$ , in which all A-site cations are tetrahedrally coordinated, while all B-site cations are octahedrally coordinated. Next we point out that the normal spinel shows a structurally unique feature if viewed along the  $[111]$  crystallographic axis. Specially, the crystal structure can be regarded as a stacking of alternate lattice planes, each of which is composed of single type of ions (see Fig. 4.1). In this stacking, the O sublattice has the cubic close packing (CCP) atomic arrangement. In the meanwhile, the A and B ionic planes show three distinct types of geometrically frustrated lattices: triangular A plane (T plane), triangular B plane (T' plane), and kagome B plane (K plane). In the bulk, totally 18 such ionic planes complete

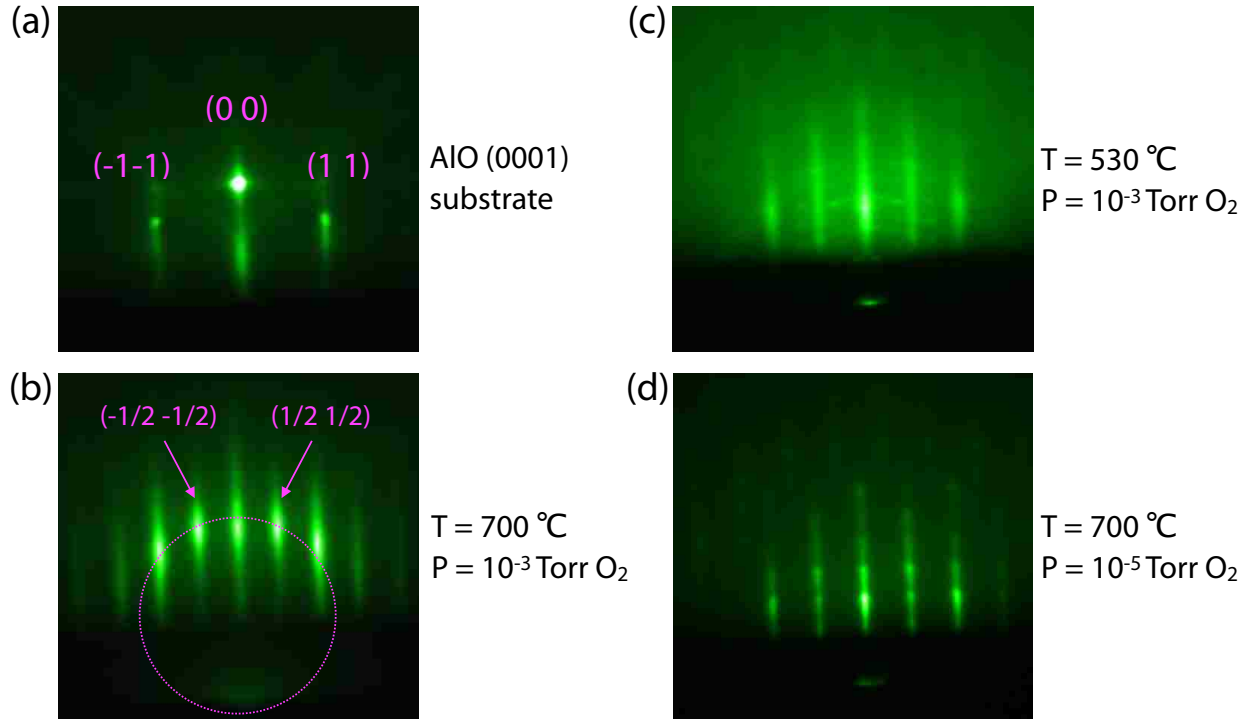
a full periodicity in the form of [O-K-O-T-T'-T]<sub>3</sub> [120] with [O-K-O-T-T'-T] as the basic repeat unit. In what follows, this basic repeat unit is referred as “1 unit cell” of the (111)-oriented normal spinel.

From the synthesis point of view, however, there are mainly three issues that one needs to overcome to obtain high-quality (111) normal spinel oxide thin films and heterostructures. First, due to the limited availability of iso-structural/iso-symmetric substrates, large lattice mismatch (> 5%) between film and substrate generally leads to incoherent or inhomogeneous growth. Second, a magnetically passive spacer in the superlattice has to be chemically stable and structurally compatible with the spinel lattice. Last but not least, mixture of multivalency of the transition metal ions and cation distribution disorder between A and B sites have been reported [121, 122, 123, 124] during the growth of spinel films, which if present will destroy the normal spinel stacking patterns and further destroy the structure of expected geometrically frustrated lattices. For these reasons, despite the conceptual attractiveness of such geometrical design, the epitaxial growth of high-quality (111)-oriented spinel oxide thin films and heterostructures still remains rarely explored.

## 4.2 Growth and characterizations of (111) CoCr<sub>2</sub>O<sub>4</sub> thin films

In this section, we report our studies on the growth and characterizations of CCO thin films along its [111] crystallographic axis by pulsed laser deposition. Among many choices of spinel oxides, CCO is selected as a prototypical candidate which has been widely studied exhibiting interesting physical phenomena in the bulk materials including conical spin states [125, 126, 127], induced multiferroic behavior at low temperature [128, 129], and an unconventional magneto-structural phase transition in high magnetic fields [11]. CCO is a normal spinel oxide in which all of the Co<sup>2+</sup> occupies the tetrahedral sites while Cr<sup>3+</sup> resides within the octahedral sites. The electronic configurations of Co<sup>2+</sup> and Cr<sup>3+</sup> are 3d<sup>7</sup> and 3d<sup>3</sup>, respectively, both having S = 3/2 [130, 125, 126, 127].

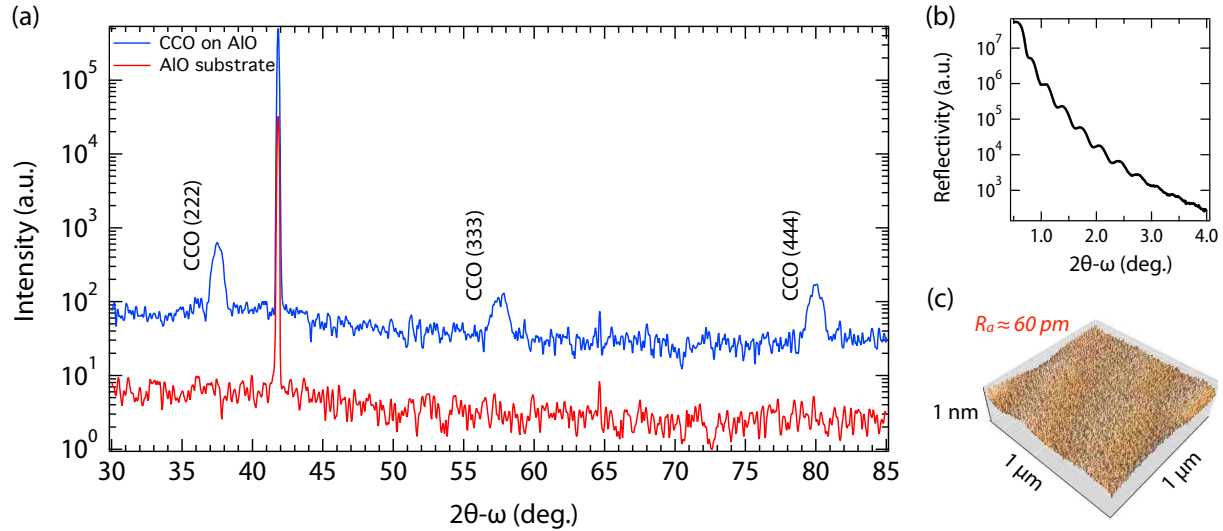
CCO thin films were fabricated by the pulsed laser interval deposition method [131] using a KrF excimer laser operating at  $\lambda = 248$  nm. The laser’s intensity and pulse rate were 2 J/cm<sup>2</sup> and 4 Hz, respectively. Other growth parameters (the substrate temperature T and the oxygen partial pressure P) were optimized according to *in-situ* RHEED patterns. For the first step, it is necessary to investigate the quality of the substrate. As seen on Fig. 4.2 (a), the specular reflection spot (0 0) together with ( $\bar{1}$   $\bar{1}$ ) and (1 1) spots on the



**Figure 4.2:** *In-situ* RHEED patterns. (a) AIO (0001) substrate. (b)-(d) CCO films grown at different conditions. Note, the incident electron beam of RHEED is fixed along the  $[1\bar{1}00]$  direction of the substrate.

Laue circle, and the strongly developed Kikuchi lines testify the smooth morphology of the AIO (0001) substrate [132]. After CCO was deposited on the substrate surface, two additional half order reflections occurred on the RHEED images [Fig. 4.2 (b)] due to the double expanding of CCO unit cell compared to AIO in the real space. Moreover, with the optimized growth parameters ( $T = 700\text{ }^{\circ}\text{C}$  and  $P = 10^{-3}\text{ Torr O}_2$ ) the distinct spots from both specular and off-specular reflections with the streak patterns indicate excellent film crystallinity and flat surface morphology. These observations further confirm a well defined 2D growth mode. It is also worth noting that lowering either the growth temperature or the oxygen partial pressure would render a quasi-2D growth mode [Fig. 4.2 (c)] or even a 3D island mode [Fig. 4.2 (d)]. When the deposition process was completed, the film was annealed at the growth condition for 15 min to compensate any oxygen vacancy and then cooled down to room temperature.

It is of critical importance to ensuring the (111) growth direction is maintained after the deposition and determining the total film thickness. Thus we performed the XRD  $2\theta$ - $\omega$  scans (Cu  $K_{\alpha}$  radiation,  $\lambda = 1.5406\text{ \AA}$ ) on resultant CCO thin films as well as on a pure



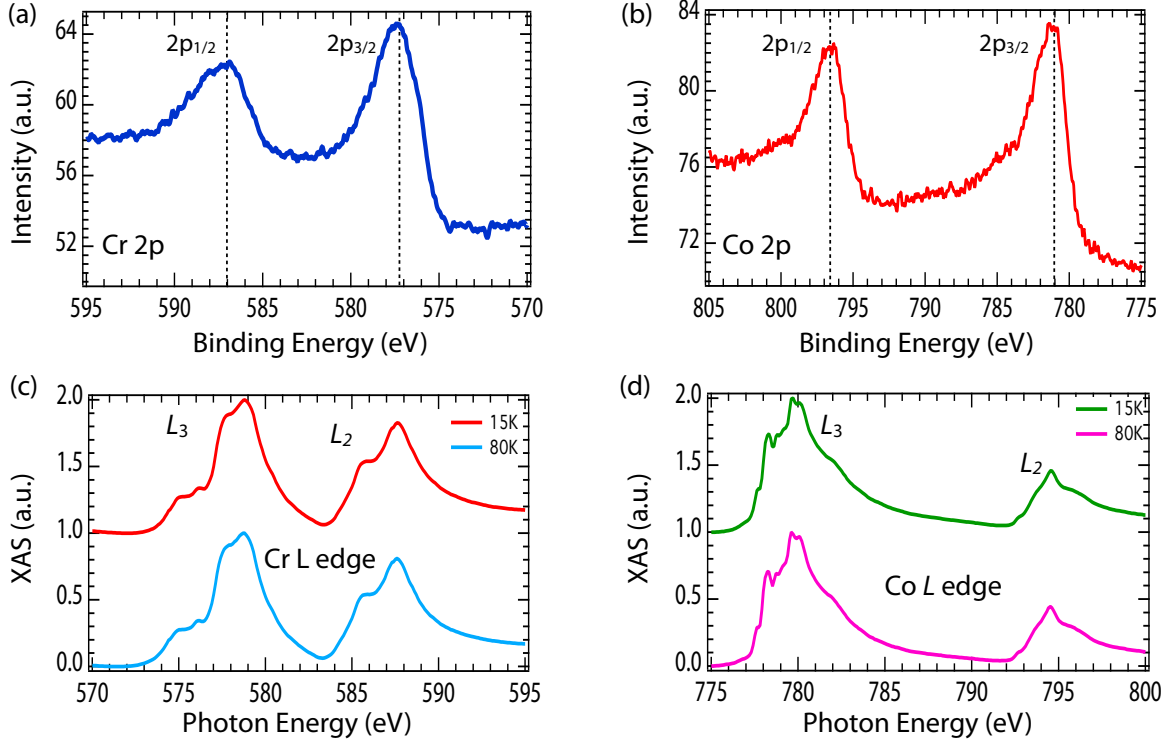
**Figure 4.3:** (a) X-ray diffraction of CCO thin films and the AlO substrate. Film peaks are labeled on the graph. The sharp peaks belong to the AlO (0001) substrate. Note, the lattice constant obtained is  $8.34 \text{ \AA}$ , which equals the bulk value. (b) X-ray reflectivity data of the same sample. Film thickness calculated according to the Kiessig fringes is about 25 nm. (c) Atomic force microscopy scan of the film surface.

AlO substrate, together with a XRR scan on the film. As shown in Fig. 4.3 (a), the expected CCO (222), (333) and (444) Bragg reflections are clearly seen, which testify that the sample has the (111) out-of-plane orientation. The lattice constant calculated from the peak position is  $\sim 8.33 \text{ \AA}$ , which is in excellent agreement with the bulk value [125]. Based on the XRD pattern, no impurity phases are detected. Fig. 4.3 (b) displays the XRR curve of CCO, yielding a total film thickness of about 25 nm extracted from the period of the thickness fringes, which provides additional evidence for the sample flatness. In addition, smooth surface morphology is corroborated by the AFM imaging shown in Fig. 4.3 (c).

The obtained average surface roughness is below 60 pm for a  $1 \mu\text{m}$  by  $1 \mu\text{m}$  scan.

Due to the well-known persistent multivalency problem in the thin film growth of spinel oxides, the proper valency of the Cr and Co ions must be confirmed. Fig. 4.4 (a)–(b) show XPS measurements taken on Cr and Co 2p core levels. As seen, Cr has two peaks at about 577 eV and 587 eV which correspond to the  $2p_{3/2}$  and  $2p_{1/2}$  peaks indicating Cr is in the trivalent state [133, 134]. The  $2p_{3/2}$  and  $2p_{1/2}$  peaks of Co are at 781 eV and 797 eV indicating Co is in the divalent state [133, 134]. In addition, no extra peaks from  $\text{Cr}^{2+}$ ,  $\text{Cr}^{4+}$  or  $\text{Co}^{3+}$  are observed, which excludes the possibility of a multivalent charge state.

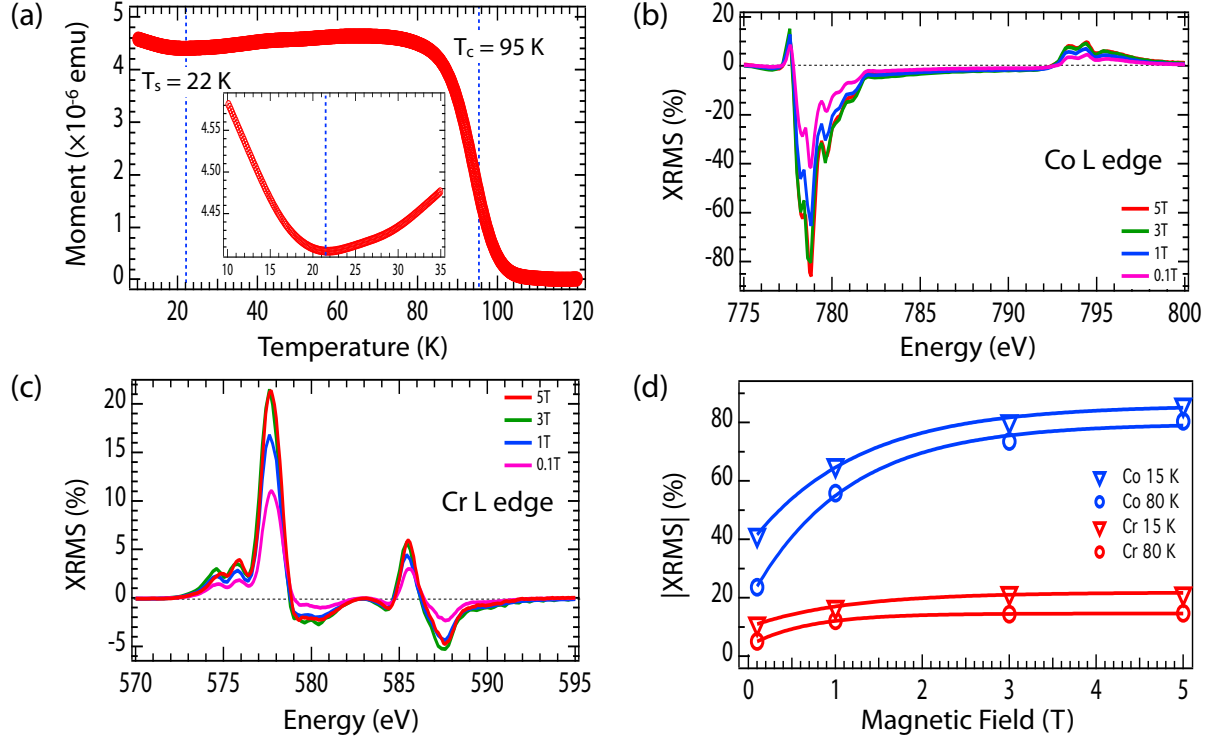
To further elucidate that the CCO thin film maintains the normal spinel structure with-



**Figure 4.4:** (a)-(b) Core level XPS data (Mg anode) of (a) Cr 2p and (b) Co 2p. (c)-(d) X-ray scattering spectra measured at 15 K and 80 K on the L edge of (c) Cr and (d) Co.

out cation disorder, XMCD experiments were carried out at beamline 4-ID-C of the Advanced Photon Source (APS) in Argonne National Laboratory. Left ( $I^+$ ) and right ( $I^-$ ) polarized soft x-rays with an incident angle of  $15^\circ$  were tuned to the  $L$  edges of Cr and Co and recorded in scattering mode [72]. In the XRMS mode, the difference between  $I^+$  and  $I^-$  near the absorption edge represents the contribution to the scattering amplitude from uncompensated magnetic moments of a specific chemical element [135], while the sum  $I^+ + I^-$  is connected to the charge state [136]. Fig. 4.4 (c)–(d) show the total reflectivity intensity ( $I^+ + I^-$ ) of both Cr and Co as a function of incident photon energy. As seen, the lineshapes of each element measured at 15 K and 80 K are almost unchanged. The positions of the main absorption edges  $L_3$  and  $L_2$  together with the satellite peaks are almost identical to the previous reported study [5], which implies all of the  $\text{Cr}^{3+}$  are in the octahedral sites while all the  $\text{Co}^{2+}$  sit in the tetrahedral sites. The slightly different lineshapes from the references are due to the specific detector mode used in the experiment.

Next we discuss the magnetic properties of the CCO thin film. To this end, temperature dependent magnetization was measured while cooling in an applied magnetic field of 0.2



**Figure 4.5:** Temperature-dependent magnetization curves of CCO in an applied field of 0.2 T along the  $[1\bar{1}00]$  direction of the substrate. The inset is a magnified plot in the vicinity of the second transition point. (b)-(c) XRMS data on the L edge of (b) Co and (c) Cr measured with different applied magnetic fields at 15 K. The color series of red, green, blue and pink stands for field strength of 5 T, 3 T, 1 T and 0.1 T, respectively. (d) Absolute values of Co and Cr XRMS main peaks as a function of applied field and temperature.

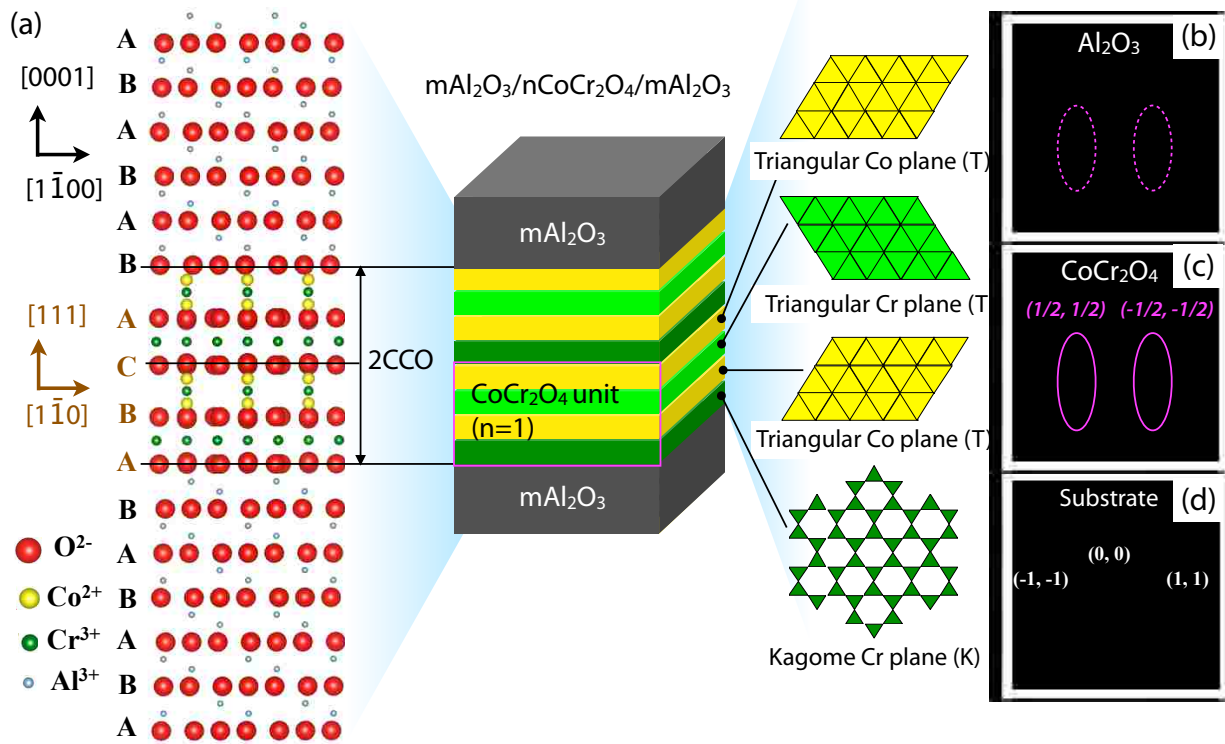
T by SQUID. As seen in Fig. 4.5 (a), the ferrimagnetic phase transition occurs at a  $T_c$  around 95 K. As the temperature further decreases, the collinear to incommensurate spiral ferrimagnetic phase transition [127] takes place at  $T_s \approx 22$  K. Element-specific spin alignments were further investigated by XRMS spectra on Cr and Co  $L_{2,3}$  absorption edges at 15 K and 80 K in different applied fields from 5 T to 0.1 T. All of the XRMS data have been normalized by using the corresponding total reflectivity intensity. As presented in Fig. 4.5 (b)–(c), both Cr and Co exhibit significant XRMS signals in the vicinity of their absorption edges. The maximal XRMS signal at Cr  $L_3$  edge is about +20% while that of Co is around -80%, which indicate strong ferromagnetic ordering of the moments on each type of metal ions, respectively. Note, the sign of the maximal XRMS signal is opposite for Cr and Co due to the ferrimagnetic nature of this material, which implies the overall spin orientation of Cr is antiparallel to those of the Co ions. In Fig. 4.5 (d), the

magnitudes of the maximal XRMS values of Cr and Co at 15 K and 80 K are plotted as a function of applied magnetic field showing a saturation field of approximately 3 T. This is much larger than the reported bulk values [127, 128, 134] which are typically less than 0.6 T. This difference is attributed to the fact that in the bulk the magnetic field is commonly applied along the CCO [001] direction which is the spin easy axis.

### 4.3 Establishment of (111) $\text{CoCr}_2\text{O}_4/\text{Al}_2\text{O}_3$ superlattices

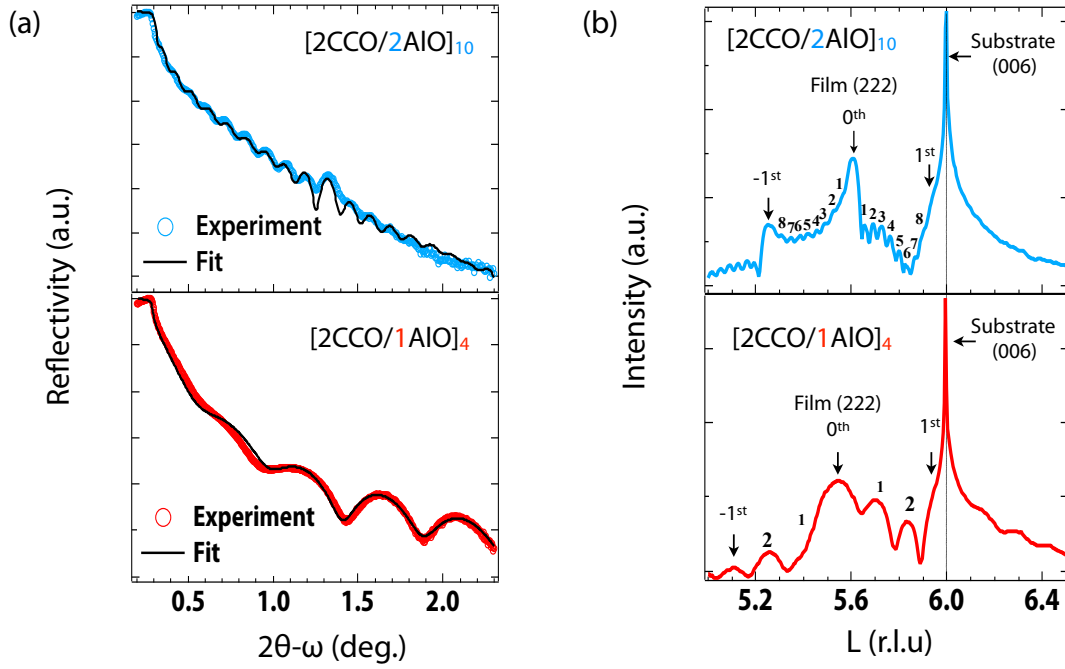
After discovering the proper growth condition of CCO, we turn our attention to the next step: manipulating the thickness of (111)-oriented CCO towards the 2D ultrathin limit. As it is proposed in many artificial superlattice systems [137, 41, 42, 138, 139, 43], there exists a common material design strategy in the GLE theme, namely growing the 2D “active layer” sandwiched by some wide band-gap insulating spacer because in such a way, the spacer can entirely terminate the 3D lattice geometries, chemical environments, electron hopping routes, and magnetic exchange couplings along the growth direction. Also from the experimental point of view, establishing a superlattice structure will be beneficial to obtaining more distinct signals from the “active layer”. Therefore, it is of great importance to determine the spacer material which is structurally compatible, chemically stable, and able to be grown under the growth condition of the active material. In our case, AlO was selected as the spacer because: (1) AlO is a non-magnetic insulator with a large band gap of about 9 eV. (2) Since along the (0001)-direction, its oxygen sublattice consists of the hexagonal close packing (HCP) arrangement in the form of AB, which has an in-plane lattice geometry almost perfectly matching the CCP arrangement of oxygen sublattice of CCO in the form of ABC [see Fig. 4.6 (a)]. In addition, a fairly small lattice mismatch of  $\sim 3\%$  can be obtained when we compare the respective in-plane O-O distances (AlO: 2.74 Å; CCO: 2.82 Å). (3) It has been reported when atomic layers along the growth direction are not charge neutral planes, the polarity mismatch between different components may lead to interfacial reconstruction, defect and impurity phase formation [140, 141, 54]. The compatibility of CCP and HCP lattices offers the perfect structural and chemical continuity between CCO and AlO layers, which effectively eliminates the polar mismatch issue. A series of  $2\text{CCO}/m\text{AlO}$  ( $m = 1$  and  $2$  unit cells) superlattices were fabricated using a KrF excimer laser operating at  $\lambda = 248$  nm. The substrate was maintained at  $700$  °C under a partial pressure of  $1 - 5$  mTorr of oxygen during the deposition with the laser’s inten-





**Figure 4.6:** (111)-oriented CCO/AIO heterostructures. (a) Epitaxial relationship between CCO and AIO. The hexagonal close packing of AIO oxygen sublattice is labeled as AB in black, while the cubic close packing of CCO oxygen sublattice is labeled as ABC in brown. (b)-(d) RHEED images during the growth of each component. The half-order reflections (marked by pink solid circles) observed on CCO layer is due to the double expansion of the in-plane unit cell.

sity  $\sim 2 \text{ J/cm}^2$  at the target. The ablation frequencies for CCO and AIO were 4 Hz and 2 Hz, respectively. Samples were annealed at the growth condition for 15 min and then cooled down to room temperature. The entire growth process was monitored by *in-situ* RHEED with the incident electron beam along the  $[1\bar{1}00]$  direction of the substrate.  $1 \mu\text{m}$  by  $1 \mu\text{m}$  AFM images were scanned over several different areas of the sample surface after the post-annealing process to check the surface morphology and flatness. Detailed information about the thickness of each layer and interfacial roughness was obtained from the fittings of the X-ray reflectivity (Cu  $K_{\alpha 1}$  line ( $\lambda = 1.5406 \text{ \AA}$ )) data. Synchrotron-based X-ray diffraction measurement was performed at the beamline 6-ID-B of Argonne National Laboratory. The chemical valences and proper stoichiometry of the samples was investigated by core-level XPS measurements with monochromatic Al  $K_{\alpha}$  source.



**Figure 4.7:** (a) XRR and (b) XRD curves of 2CCO/*n*AlO (*n* = 1 and 2) superlattices with distinct repeat periodicity. Both the thickness fringes and the superlattice satellite peaks are clearly seen on the graphs. The incident wavelength for XRR is  $\lambda = 1.5406 \text{ \AA}$  whereas for XRD,  $\lambda = 1.4932 \text{ \AA}$ .

First we discuss the structural properties of the heterostructures. Fig. 4.6 (b)–(d) RHEED patterns present a detailed overlook of the deposition process. The clear specular and off-specular reflections on the zero-order Laue circle together with the Kikuchi lines in Fig. 4.6 (d) demonstrate a flat and good crystalline substrate surface. Once the CCO layer is formed on the substrate, two additional streaks occur in the middle of the specular and off-specular spots as shown in Fig. 4.6 (c). These half order reflections are the characteristic signature of spinel thin films grown on sapphire substrate and have also been observed in other works [142, 143, 123]. The evolution of these RHEED images confirms that the epitaxial growth relation is CCO (111)[1 $\bar{1}$ 0] ||  $\alpha$ -AlO (0001)[1 $\bar{1}$ 00]. When the first AlO is deposited onto the CCO layers, the typical spinel half orders become weaker and as the second AlO layer is deposited, the half order streaks vanish and the RHEED pattern looks closer to the substrate pattern, as displayed in Fig. 4.6 (b). These observations demonstrate the formation of the  $\alpha$ -AlO spacer as designed on top of the CCO layers. Further AlO deposition produces the same RHEED patterns as Fig. 4.6 (b) which reveals the  $\alpha$ -

**Table 4.1:** Fitting parameters of the reflectivity curves of CCO/AlO superlattices.

Sample	Items	Top AlO (Å)	Superlattice (Å)	Bottom CCO (Å)
[2CCO/1AlO] <sub>4</sub>	thickness	14.6	9.9/13.6	11.0
	roughness	3.5	2.6	1.0
[2CCO/2AlO] <sub>10</sub>	thickness	30.8	9.8/27.0	12.9
	roughness	5.0	3.4	0.7

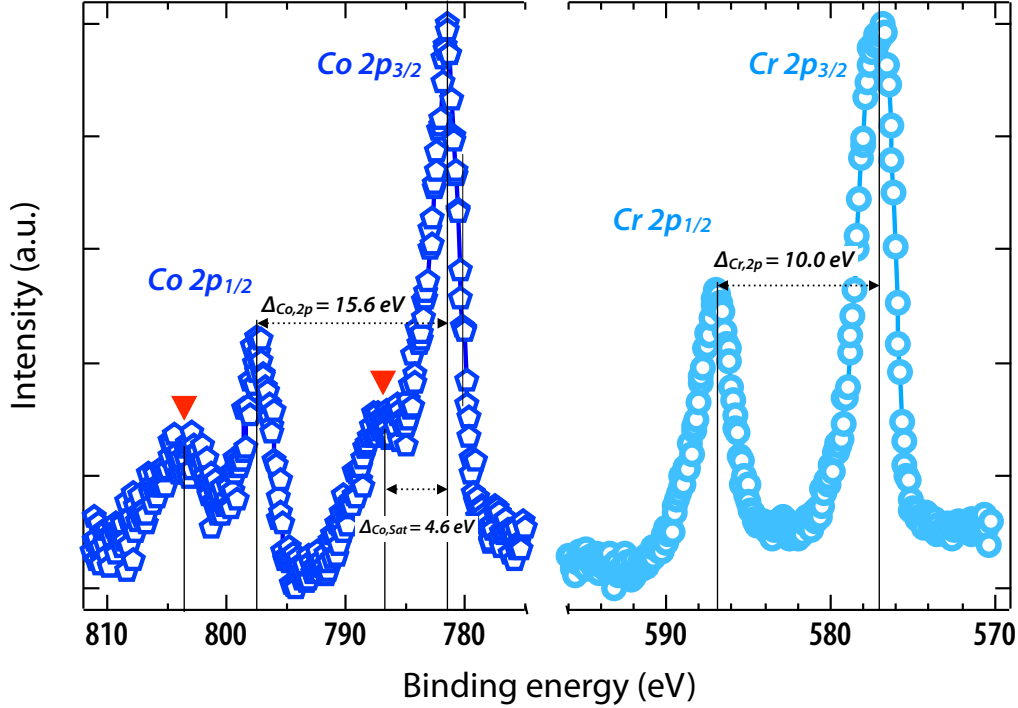
AlO phase maintains 2D stability. During the whole deposition process, the RHEED intensity oscillations of the specular spot indicate a layer-by-layer growth of the superlattices. The distinct reflection streaks are maintained throughout the deposition implying the well developed crystallinity. To further examine the surface lattice symmetry, the samples were rotated by 60° steps relative to the original position exhibiting the same pattern as Fig. 4.6 (b), which confirms that the surface lattice has indeed a six-fold symmetry. In addition, the average rms surface roughness of the resultant samples is about 2 Å, which provides another strong evidence of the smooth surface morphology.

More detailed information about the thickness, the surface and interface roughness of these sets of superlattices was investigated by XRR. Two typical reflectivity curves with simulations for a thin sample [2CCO/1AlO]<sub>4</sub> and a thick [2CCO/2AlO]<sub>10</sub> sample are shown in Fig. 4.7 (a). The distinct intensity oscillations (Kiessig fringes) over the whole scan range indicate abrupt interfaces and flat surface crystallinity of the samples. All of the fitting parameters and the corresponding values are given in Table 4.1. As seen, the fitted thickness of each layer is in excellent agreement with the values estimated from the specific number of laser pulses and RHEED oscillations of the reflected intensity. Furthermore, both superlattices maintain low roughness throughout the whole sample which corroborates the layer-by-layer stacking of each part also monitored by RHEED. The overall structural quality of the films have been investigated by synchrotron-based XRD. The diffraction scan in the vicinity of sapphire (006) reflection on the superlattices are shown in Fig. 4.7 (b). As seen, besides the sharp substrate (006) peak, the broad film peak surrounded by thickness fringes on both sides which correspond to the (222) reflection of the superlattice is also clearly observed. Based on the XRD data, good crystallinity and proper (111) orientation of the heterostructures have been confirmed. Besides that, both the superlattice satellite peaks ( $\pm 1^{st}$ ) and the thickness fringes of [2CCO/2AlO]<sub>10</sub> are

clearly distinguishable and labeled out on the figure. There are 8 fringes between two superlattice peaks, which is consistent with the superlattice repeat unit 10 (N repeat unit, N-2 fringes between superlattice peaks). The total thickness of this sample is about 37.1 nm which is in good agreement with the XRR simulation value  $\sim 37.5$  nm. The thickness of the superlattice unit cell, [2CCO+2AlO]  $\sim 3.71$  nm, is determined by using the positions of the  $0^{th}$  main peak the  $\pm 1^{st}$  superlattice satellites. This is also very close to the XRR simulated data  $\sim 3.68$  nm. The superlattice satellite is not quite clear on the [2CCO/1AlO]<sub>4</sub> XRD scan. The reason is probably due to the fact that the number of repeat units are so small that the superlattice satellite and thickness fringes are of similar width and amplitude. Without simulation, it is difficult to distinguish. This is consistent with the XRR results, for the [2CCO/1AlO]<sub>4</sub> sample, neither the experimental nor the simulated data exhibits very obvious superlattice satellites.

Next we turn our attention to the electronic properties of these samples. In order to investigate the valences and chemical stoichiometry of the sandwiched CCO layers, core-level XPS measurements were performed on the superlattices. Fig. 4.8 shows the core-level Co 2p and Cr 2p spectra collected on the representative 2CCO/1AlO sample. As seen on the left panel, the Co 2p spectrum consists of the spin-orbit split peaks corresponding to Co 2p<sub>3/2</sub> and Co 2p<sub>1/2</sub> at binding energies of 781.66 eV and 797.25 eV, respectively, and has an energy separation denoted as  $\Delta_{Co,2p} \sim 15.6$  eV between them. The observed binding energy separation of 15.6 eV is characteristic for compounds containing Co<sup>2+</sup> ions in a tetrahedral oxide environment [144, 145]. We also note that the binding energy separation in case of Co<sup>3+</sup> containing compounds is usually smaller ( $\sim 15.1$  eV) [146].

Apart from the spin-orbit split main peaks, the Co 2p spectrum also consists of two intense shake-up satellite peaks located on the higher energy sides of the Co 2p<sub>3/2</sub> and Co 2p<sub>1/2</sub> peaks, which are highlighted by the red arrows. It is well known [146, 147] that while Co<sup>2+</sup> compounds show intense shake-up satellite peaks in Co 2p spectrum, the same features are much weaker in case of Co<sup>3+</sup> containing compounds. In case of Co oxide samples, the shake-up satellite corresponds to the charge transfer excitation from a ligand oxygen 2p level to empty Co 3d states, and hence the relative energy separation from the shake-up satellite to its corresponding main peak is a distinct signature of the Co charge state. As seen in Fig. 4.8, the separation between the Co 2p<sub>3/2</sub> peak and the corresponding shake-up satellite is 4.6 eV and is very close to that observed in other Co<sup>2+</sup> compounds [144]. On the right panel, the Cr 2p spectrum similarly consists of the spin-orbit split Cr 2p<sub>3/2</sub> and



**Figure 4.8:** Core-level XPS data of the Co and the Cr 2p levels of the samples. The red arrows represent the  $\text{Co}^{2+}$  shake-up satellites. The binding-energy separations of the Co 2p peaks, Cr 2p peaks and the energy difference between Co  $2p_{3/2}$  and its corresponding satellite peak, are denoted as  $\Delta_{\text{Co},2p}$ ,  $\Delta_{\text{Cr},2p}$ , and  $\Delta_{\text{Co},\text{Sat}}$ , respectively on the graph.

Cr  $2p_{1/2}$  peaks at the binding energies of 577.15 eV and 587.20 eV, respectively. The binding energy difference of  $\sim 10.0$  eV between the Cr  $2p_{3/2}$  and Cr  $2p_{1/2}$  peaks agrees very well with other  $\text{Cr}^{3+}$  containing compounds [145]. Based on these XPS results, the valences of Co and Cr in our superlattice samples are assured to be 2+ and 3+, respectively. Furthermore, the binding energy of the Al 2p level obtained from the XPS measurement is  $\sim 74.3$  eV, which confirms Al has a valency of 3+ in these systems [148].

#### 4.4 Summary

In summary, we have fabricated (111)-oriented CCO thin films and CCO/AlO heterostructures with geometrically frustrated lattices on sapphire (0001) substrate. The comprehensive structural, electronic and magnetic characterizations demonstrate the high quality of the samples with expected epitaxial orientation, proper chemical valence and stoichiometry. Both the CCO and the AlO thickness can be digitally controlled. These results offers strong evidences on experimental realization of the GLE concept using state-of-the-art

thin film deposition technique, and pave a way for building artificial quasi-2D transition metal heterostructures on which a plethora of intriguing quantum phenomena can be expected.

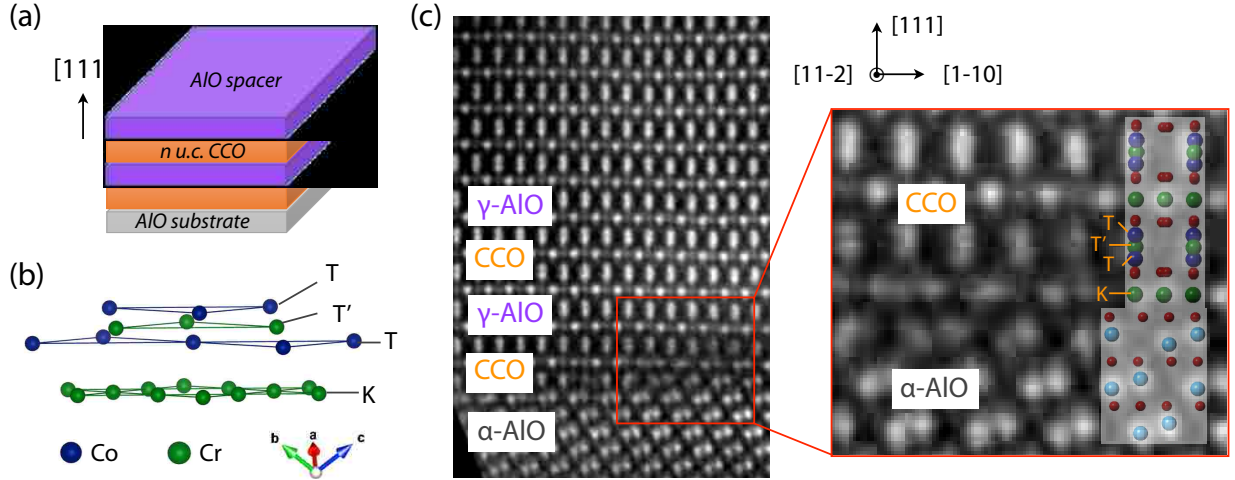
## Chapter 5

### Emergent magnetism of quasi-two-dimensional frustrated lattices by geometric design

In the previous chapter, we have described in details about the initial step of geometrical lattice engineering (GLE) in the pursuit of magnetically frustrated systems – fabrications of high quality (111)-oriented ultrathin  $\text{CoCr}_2\text{O}_4/\text{Al}_2\text{O}_3$  (CCO/AlO) superlattices. In this chapter, we switch our attentions to the electronic and magnetic properties of this system using a combination of state-of-the-art characterization techniques. It is found that as the thickness of CCO is narrowed towards the two-dimensional (2D) limit, unlike the bulk whose ground state has a spiral ferrimagnetic configuration, an emergent collinear ferrimagnetic phase becomes robust for the superlattices. And eventually for the ultrathin case, no long range magnetically ordered state is observed and the system presents a significant increase in the frustration parameter, indicating the realization of a novel strongly frustrated system. Further explanation of these phenomena is proposed by linking the underlying mechanism to the effective tuning of electronic bandwidth  $W$ , Hubbard  $U$  and exchange coupling  $J$  by GLE. After carefully excluding the other probabilities, we propose that this artificial frustrated system might be a candidate of quantum spin liquid.

#### 5.1 Introduction

When antiferromagnetic exchange interactions between localized spins cannot be satisfied simultaneously on triangle-related lattices, the systems become geometrically frustrated with magnetically disordered phases significantly different from simple paramagnets [149]. From theory, spin liquid belongs to one of these exotic states, in which a macroscopic degeneracy of the ground state coexist, giving rise to remarkable collective phenomena [150]. So far, very few candidate materials have been achieved experimentally due to the challenges in fabricating the peculiar lattices with networks of triangles. Here, we report the discovery of emergent magnetic states on artificial heterostructures composed of ultrathin (111)-oriented  $\text{CoCr}_2\text{O}_4$  sandwiched by nonmagnetic  $\text{Al}_2\text{O}_3$  spacer. We reveal the degree of frustration is remarkably enhanced at the two-dimensional limit, where the slab of  $\text{CoCr}_2\text{O}_4$  contains four alternating layers of triangle and kagome planes. The system



**Figure 5.1:** Overview of the structural and electronic properties of the superlattices. (a) Schematic of the  $(\text{CCO})_n/(\text{AlO})_3$  superlattices. (b) The basic repeating unit ( $n = 1$ ) of the (111)-oriented CCO, which includes four geometrically frustrated planes: kagome Cr plane (K), triangle Co plane (T), triangle Cr plane (T'), and triangle Co plane (T). Oxygen ions are omitted for clarity. (c) High-angle annular dark-field scanning transmission electron micrograph of a  $n = 2$  sample. The substrate AIO has the  $\alpha$  phase whereas the AIO forms the  $\gamma$  phase in the film. The enlarged image (right panel) exhibits the interface between the substrate and the film. The relative positions of the oxygen (red dot) layers with respect to the cation layers are shown on the figure.

sustains a spin disordered state down to 2 K without observations of any magnetic phase transition, indicating possible realization of a spin liquid phase.

## 5.2 Experimental methods

### 5.2.1 Sample fabrication

The superlattices were grown on  $5 \times 5 \text{ mm}^2$   $\text{Al}_2\text{O}_3$  (0001) substrates by pulsed laser deposition. Stoichiometric CCO and AIO targets were ablated using a KrF excimer laser ( $\lambda = 248 \text{ nm}$ , energy density  $\sim 2 \text{ Jcm}^{-2}$ ) with a repetition rate of 4 Hz and 2 Hz, respectively. The deposition were carried out at a substrate temperature of  $700 \text{ }^\circ\text{C}$ , under an oxygen partial pressure of 5 mTorr. The films were annealed *in situ* at the growth condition for 15 minutes and then cooled down to room temperature. The layer-by-layer growth was monitored by *in situ* high pressure reflection high energy electron diffraction (RHEED). Detailed structural characterizations have been reported elsewhere [53].



### 5.2.2 Polarized X-ray absorption and scattering characterizations

The temperature-dependent XMCD experiments were performed on beamline 4-ID-C at Advanced Photon Source of Argonne National Laboratory. The L-edge X-ray absorption spectra of both Co and Cr were scanned with left- and right- polarized X-rays at grazing incidence. Samples were first field cooled down to 10 K and then measured during the warming up process. To exclude any artifact, all the measurements were conducted in both positive and negative external field. Data were recorded simultaneously with total electron yield (TEY), fluorescence yield (FY), and X-ray magnetic reflectivity (XRMS) detection modes. The XMCD hysteresis loops were measured on beamline 4.0.2 at Advance Light Source of Lawrence Berkeley National Laboratory. Samples were cooled with zero field and maintained at 15 K. The circularly polarized soft X-rays were incident with an angle of  $35^\circ$  relative to the sample surface. The luminescence detection mode was used to record the data.

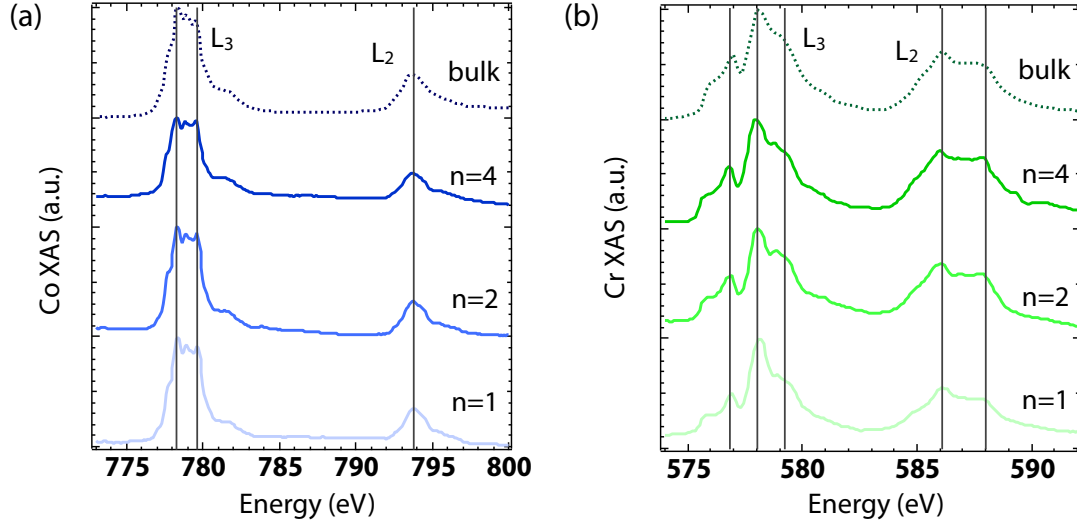
### 5.2.3 Polarized neutron reflectometry

Polarized neutron reflectometry (PNR) data with model fitting. The experiments were carried out on the PBR beamline of NIST Center for Neutron Research. The measurements were performed at 10 K after field cooling the samples in a 0.7 T magnetic field. The non-spin-flip data was fitted using the NIST Refl1D [151] software routines.

## 5.3 Results and discussions

### 5.3.1 Structure and local environment

CCO belongs to the normal spinel ( $AB_2O_4$ ) chromite  $M\text{Cr}_2O_4$  ( $M = \text{Mn}, \text{Fe}, \text{and Co}$ ), in which the  $M^{2+}$  ions occupy the tetrahedral A sites and the  $\text{Cr}^{3+}$  ions occupy the octahedral B sites [127]. The family exhibit complex magnetic ground state, determined by the ratio of the antiferromagnetic nearest-neighbor exchange coupling  $J_{AB}$  and  $J_{BB}$  [152]. In the bulk form of CCO, a collinear ferrimagnetic state first forms with a Curie temperature of 93 K and further transforms into a spiral ferrimagnetic state at  $T_S \sim 26$  K. When viewing along the (111) direction, the unit cell is composed of stacking of four geometrically frustrated planes from the two sub-lattices (Fig. 5.1 (a) and (b), oxygen ions are not shown). In the meanwhile,  $\gamma$ -AlO, which is an A-site deficient spinel is selected as the non-



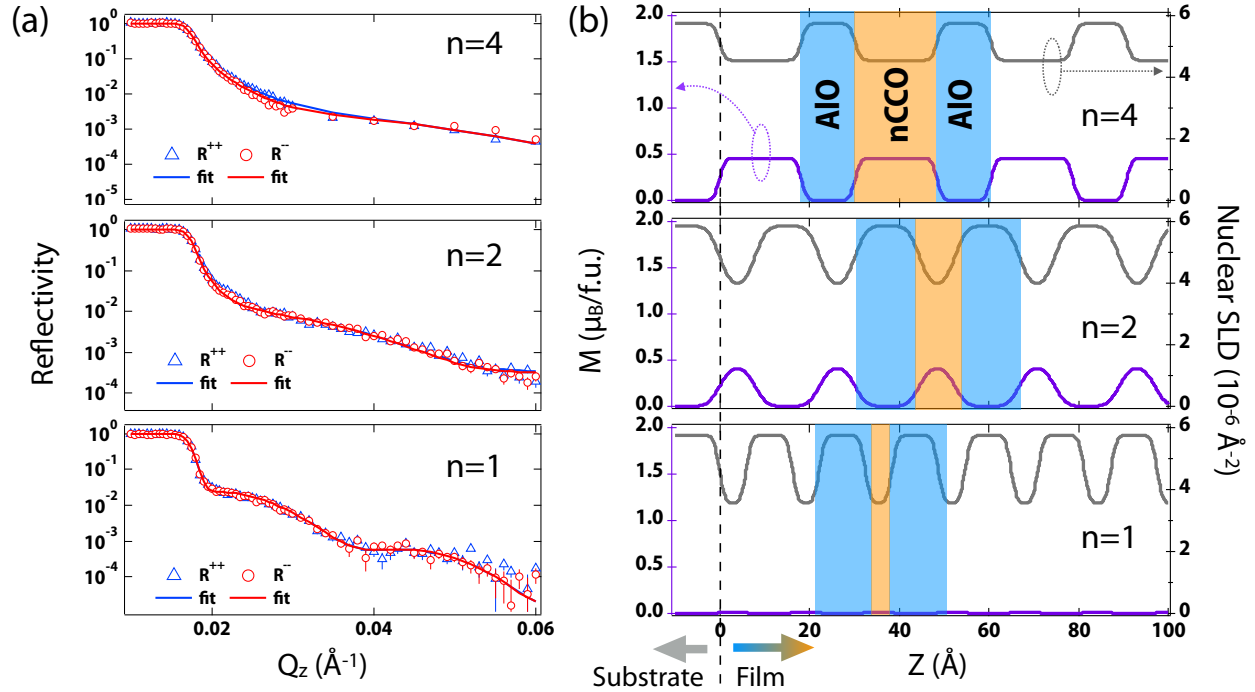
**Figure 5.2:** Co (a) and Cr (b) L edge X-ray absorption spectra of the superlattices with  $n = 1, 2,$  and  $4$ . The bulk spectra are plotted as references taken from measurements on CCO powders [5] with normal spinel structure.

magnetic spacer because of the structural compatibility with CCO.

A series of (111)-oriented  $[(\text{CCO})_n/(\text{AlO})_3]_4$  superlattices ( $n = 1, 2$  and  $4$ ) were fabricated by pulsed laser deposition on sapphire (0001) substrate, as described in details elsewhere [142, 53]. Moreover, the degree of cation distribution disorder is investigated by X-ray absorption spectroscopy (XAS) measurement, an element-specific technique that is sensitive to probe the chemical state and local environment. No clear signature of cation distribution disorder is observed for all of the superlattices due to the fact that the lineshapes as well as the peak positions at the  $L_{2,3}$  absorption edge ( $2p \rightarrow 3d$  transition) are almost identical to the bulk results (Fig. 5.2 (c) and (d)). This information corroborates the formation of the expected ionic layers out of normal spinel structure.

### 5.3.2 Overall magnetization characterizations

PNR measurements with model fittings on the superlattices, as shown in Fig. 5.3 not only confirm the high quality of the superlattice structure once again, but also clarify the net magnetic moment per chemical formula with different CCO thickness. The in-plane magnetization per formula unit decreases slightly from  $0.48 \mu_B/f.u.$  at  $n = 4$ , to  $0.42 \mu_B/f.u.$  at  $n = 2$ , which demonstrate the formation of long-range magnetic orderings in these two samples. However, the value drops dramatically down to  $\sim 0$ , indicating the absence of



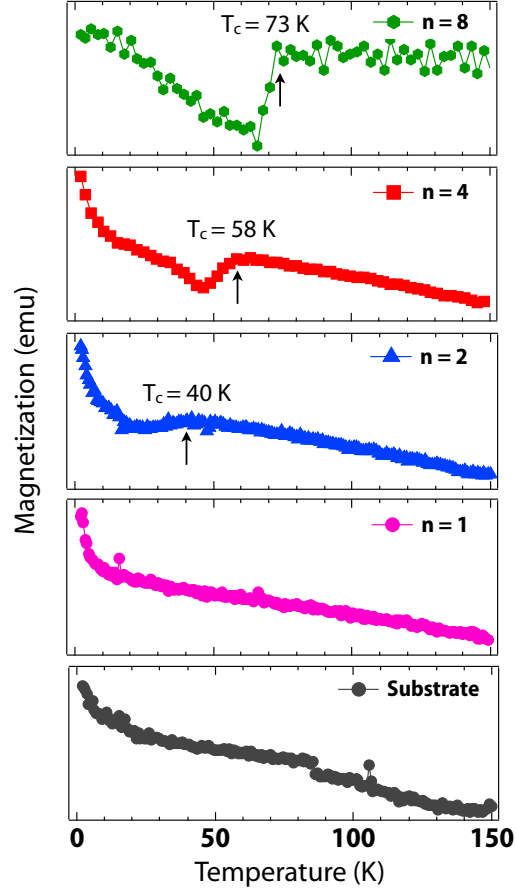
**Figure 5.3:** (a) PNR data with model fitting on the nCCO/3AlO superlattices. (b) Net magnetization and the nuclear scattering length density (SLD) depth profiles of the superlattices. Data was recored at 10 K with 0.7 T in-plane external field.

any long-range magnetic orderings at  $n = 1$ .

In order to make sure of the magnetic phase transition temperature, temperature dependence of the *dc* magnetization was scanned on each sample, which are plotted in Fig. 5.4. The signals were recorded during the zero field cooling process from 300 K down to 2 K. The bare substrate in this experiment was treated exactly the same as growing a superlattice with full cycles of heating, annealing and cooling, to elucidate any artifacts. As seen, the ferrimagnetic transition occurs on the  $n = 8, 4,$  and  $2$  samples at  $T_c = 73$  K,  $58$  K, and  $40$  K, respectively, whereas no clear signature of any transition was observed on the  $n = 1$  sample down to the base temperature as its signal is almost identical to that of a bare substrate. Including the bulk transition temperature at  $T_c = 95$  K, a clear monotonic decrease of  $T_c$  is observed as the CCO thickness is suppressed towards the 2D limit.

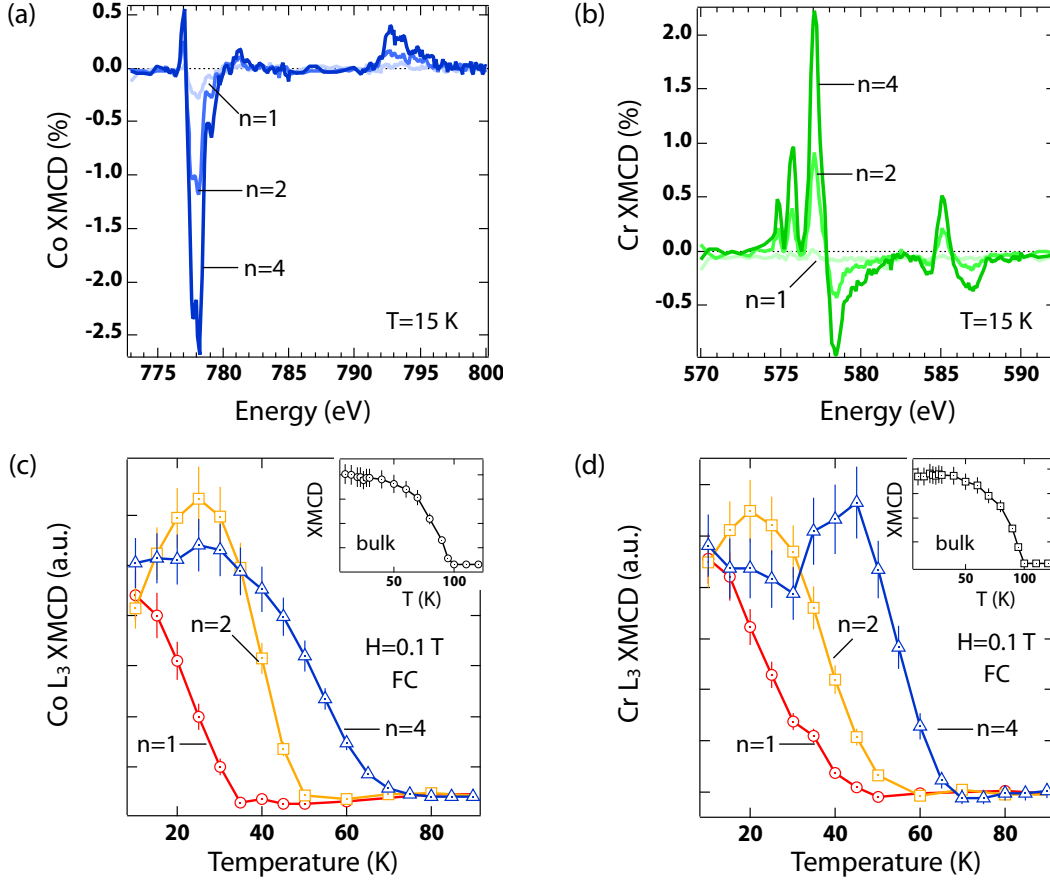
### 5.3.3 Temperature-dependent XMCD and hysteresis loops

To further investigate the magnetic properties of each sublattice of CCO, XAS were recored simultaneously with both left- and right-polarized incident X-rays. The difference between



**Figure 5.4:** Temperature dependence of magnetization of both the  $n\text{CCO}/3\text{AlO}$  superlattices and the substrate. The measurements were performed using the Superconducting Quantum Interference Devices (SQUID) from quantum design.

two spectra, X-ray magnetic circular dichroism (XMCD) originates from the net magnetization of a specific probing element (Fig. 5.5 (a) and (b)). The sign of the strong  $L_3$  peaks indicate the magnetic moment of Co is along the external field while the moment of Cr is against the field. Temperature-dependent XMCD spectra on the  $L_3$  edge (Fig. 5.5 (c) and (d)) demonstrate that for  $n = 4$  and  $n = 2$  samples, an onset of the magnetization was seen at 70 K and 50 K, respectively. Below this temperature, ferromagnetic long-range orderings occur on both the Co and the Cr sublattices. However, it is not clear whether the upturn behavior for  $n = 1$  sample corresponds to the formation of any long-range ordering. To clarify this, XMCD hysteresis loops of each element were scanned up to 0.5 T (Fig. 5.6 (a) and (b)). As is consistent with the temperature-dependent results, narrow loops were observed for  $n = 4$  and  $n = 2$  samples with the net magnetization of individual element opposite to each other. Therefore, the magnetic ground state for  $n = 4$  and  $n = 2$  sam-

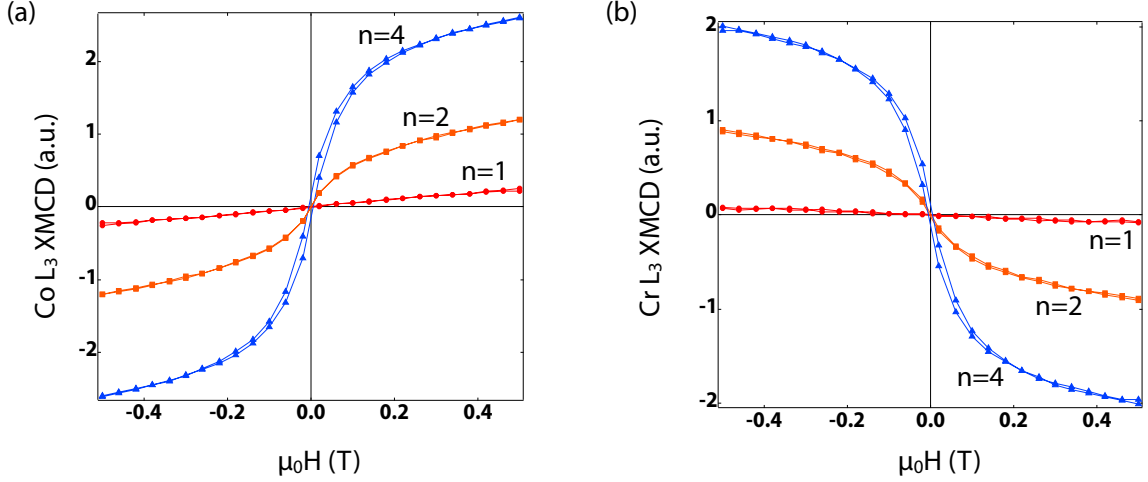


**Figure 5.5:** (a) and (b) XMCD spectra on the L edge of Co and Cr at 15 K, respectively. (c) and (d) Temperature dependence of the XMCD  $L_3$  intensity for Co and Cr, respectively. Measurements were recorded during the warming up process, after field-cooling the samples in a 0.1 T field from room temperature to 10 K. The onset of the para- to ferromagnetic transition temperature is  $\sim 70$  K for  $n = 4$  and  $\sim 50$  K for  $n = 2$  samples. The insets show the results of a 50 nm thick CCO films with (111) orientation, indicating bulk-like behaviors with an onset of the transition temperature at  $\sim 97$  K.

ples is *ferrimagnetic*. However, instead of a loop behavior, a linear relationship between the XMCD and the field was observed on both elements for the  $n = 1$  sample, indicating the absence of any long-range ordering down to 15 K. Moreover, SQUID data of the same sample (Fig. 5.4) reveals that there is no long-range ordering phases existing down to 2 K. As a result, the magnetic state of  $n = 1$  sample is a spin disordered phase.

### 5.3.4 XMCD fitting

In order to achieve deeper insights into the magnetic structure of the superlattices, we performed fittings on the XMCD results, which are shown in Fig. 5.7 and Fig. 5.8. Details



**Figure 5.6:** Magnetic hysteresis loops of the XMCD L<sub>3</sub> intensity for Co (a) and Cr (b), respectively. For all the superlattices, the scans were performed by sweeping the external magnetic field up to 0.5 T after zero-field-cooling from room temperature to 15 K.

about the fitting methods are shown below.

### Field-dependent XMCD

In the following, we show that for  $n = 4$  and 2 samples, the XMCD data can be described consistently using a two-sublattice *collinear* ferrimagnetic model [6, 7]. In this model, the net magnetic moments of each sublattice  $i$  ( $i = \text{Co}, \text{Cr}$ ) below the Curie temperature are antiparallel. Within the nearest neighbor approximation, the Weiss molecular field on each site is contributed by both the inter-sublattice and the intra-sublattice exchange interactions.

For each sublattice below the transition, the net magnetization per site is given by the modified Brillouin function:

$$y_i = B_{S_i}(x_i) = \frac{2S_i + 1}{2S_i} \coth\left(\frac{2S_i + 1}{2S_i} x_i\right) - \frac{1}{2S_i} \coth\left(\frac{1}{2S_i} x_i\right) \quad (5.1)$$

with

$$\begin{aligned} y_i &= M_i/M_{i0} \\ x_i &= \frac{g_i \mu_B S_i}{k_B T} [H + w(-a_i M_i - M_j)], i \neq j \end{aligned} \quad (5.2)$$

In which  $M_i$  is the magnetization per site of the  $i$ th sublattice and  $M_{i0}$  is the saturated magnetization. Therefore  $y_i$  is the reduced magnetization.  $S_i$  is the spin magnetic moment of the  $i$ th sublattice. In this case,  $\text{Co}^{2+}$  and  $\text{Cr}^{3+}$  ions have equal values,  $S_{\text{Co}} = S_{\text{Cr}} = 3/2$ .  $g_i$  is the gyromagnetic ratio and we took  $g_{\text{Co}} = 2.2$  and  $g_{\text{Cr}} = 2.0$  [153].  $w$  in  $x_i$  represents

the inter-sublattice Weiss constant, which is linearly promotional to the exchange interaction  $J_{AB}$ . And  $a_i$  is the factor expressing the intensity of the intra-sublattice exchange interaction with respect to the inter-sublattice value.

In order to relate the variables to our XMCD results, we rewrite  $x_i$  into the normalized form:

$$\begin{aligned} x_i &= \frac{g_i \mu_B S_i H}{k_B T} + \theta \cdot \frac{3S}{S+1} \left( -a_i \frac{M_i}{M_{i0}} - \frac{M_j}{M_{j0}} \right), i \neq j \\ \theta &= \frac{g_i^2 \mu_B^2 S(S+1)}{3k_B T} w \end{aligned} \quad (5.3)$$

Now  $M_i$  is the field-dependent XMCD intensity. Taking the non-saturation effect into consideration, we denote a ratio  $C_i \equiv M_{i0}/M_{i,H=0.5T}$  where  $M_{i,H=0.5T}$  is the XMCD intensity measured under 0.5 T external field. Finally, the ferrimagnetic Brillouin function has the form:

$$\begin{aligned} y_i &= \frac{M_i}{C_i \cdot M_{i,H=0.5T}} B_{S_i}(x_i) \\ x_i &= \frac{g_i \mu_B S_i H}{k_B T} + \theta \cdot \frac{3S}{S+1} \cdot \frac{1}{C_i} \left( -a_i \frac{M_i}{M_{i,H=0.5T}} - \frac{M_j}{M_{j,H=0.5T}} \right), i \neq j \end{aligned} \quad (5.4)$$

The fitting parameters are the dimensionless  $C_i$ ,  $\theta$ , and  $a_i$ . Especially, in our case,  $a_{i=C_o}$  is negligible due to the weak exchange interaction  $J_{AA}$  between nearest neighbor Co sites [152].

For  $n = 4$ , we obtained  $C_{C_o} = 2.54 \pm 0.10$ ,  $C_{C_r} = -2.11 \pm 0.01$ ;  $\theta = 1.28 \pm 0.01$ , and  $a_{C_r} = 0.49 \pm 0.01$ . For  $n = 2$ ,  $C_{C_o} = 4.03 \pm 0.28$ ,  $C_{C_r} = -1.67 \pm 0.07$ ;  $\theta = 1.17 \pm 0.01$ , and  $a_{C_r} = 0.37 \pm 0.01$ .

The frustration parameter,  $f$ , defined as  $f = |\Theta_{CW}|/T_c$  is related to  $a_{C_r}$  [6]:

$$f = \frac{2 + a_{C_r}}{\sqrt{a_{C_r}^2 + 4 - a_{C_r}}} \quad (5.5)$$

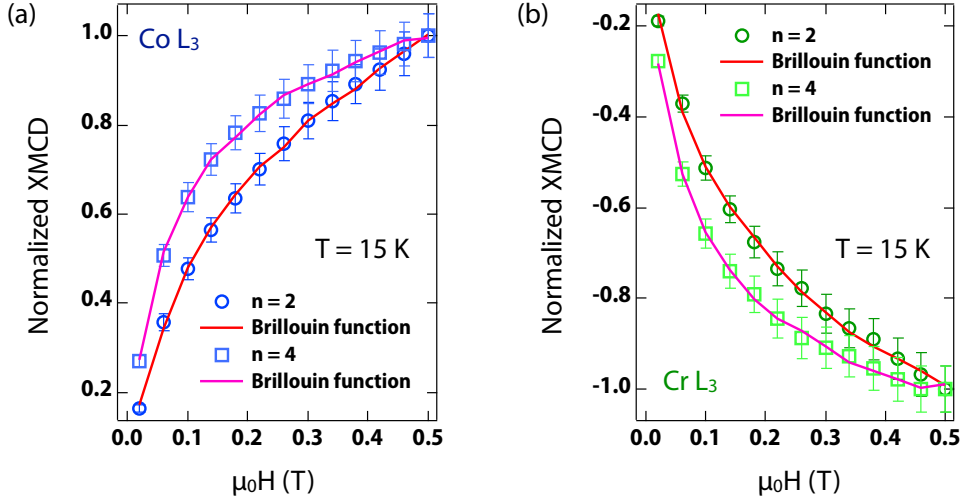
Accordingly, the frustration parameter is  $f = 1.59$  for  $n = 4$  and  $f = 1.42$  for  $n = 2$ .

### Temperature-dependent XMCD

For the  $n = 1$  sample, we applied the conventional Curie-Weiss fitting on the temperature-dependent XMCD data. The net magnetization is the sum of the signals from both elements,  $M(T) = M_{C_o}(T) + M_{C_r}(T)$ . And the net susceptibility is given by

$$\frac{1}{\chi} = \frac{C}{T + \Theta_{CW}} \quad (5.6)$$

The obtained fitted Curie-Weiss temperature  $\Theta_{CW}$  is  $\sim -480$  K. Since no clear signature on formation of long range magnetic ordering is seen down to 2 K, the frustration parameter for  $n = 1$  is  $f > 240$ .

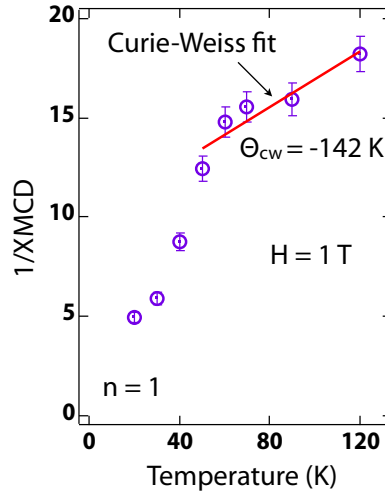


**Figure 5.7:** Brillouin function fittings on the field-dependent XMCD data of (a) Co and (b) Cr at 15 K (below their corresponding transition temperatures) for  $n = 2$  (circle) and  $n = 4$  (square) samples. The Brillouin function is modified based on a two-sublattice collinear ferrimagnetic model [6, 7].

In this model, it is proposed that the structure below the Curie temperature is a collinear ferrimagnet. The magnetic behavior of each sublattice is described using the modified Brillouin function which takes the Weiss molecular field generated from exchange coupling  $J_{AB}$  and  $J_{BB}$  into consideration. Fitting the field-dependent XMCD of each element can give rise to the ratio of  $J_{BB}/J_{AB}$ , which is the microscopic origin of the magnetic frustration in these materials. It turns out that for  $n = 4$  the ratio is  $\sim 0.48$  and  $\sim 0.35$  for  $n = 2$ . These values relates closely to the degree of frustration is judged by the frustration parameter  $f$ , defined as  $f = |\Theta_a|/T_c$  [149]. These correspond to the frustration parameter In comparison to the bulk value  $\sim 1.50$  [127], the frustration effect is suppressed monotonically when the thickness of CCO decreases from bulk to  $n = 2$ .

For the  $n = 1$  sample, we performed the Curie-Weiss Law fitting to obtain the asymptotic Curie-Weiss temperature  $\Theta_{CW}$  (Fig. 5.8). The total magnetization is obtained by summing the XMCD from Co and Cr together. It was reported the value of  $f$  is  $\sim 6$  in bulk  $\text{CoCr}_2\text{O}_4$  [11] but surprisingly for the  $n = 1$  sample, we got  $\Theta_{CW} \sim -142$  K and  $T_c < 2$  K (Temperature dependence of magnetization was measured down to 2 K and no distinct signature of any transition was observed, as shown in Fig. 5.4.), giving rise to  $f > 71$ .





**Figure 5.8:** Curie-Weiss fitting on the temperature-dependent net XMCD for  $n = 1$  sample. The net XMCD data is obtained by summing the individual signal of Co and Cr XMCD together. When adding the signals, the sign of Co is denoted as positive (along the external field) whereas it is negative for Cr (opposite to the external field). The fitted Curie-Weiss temperature  $\Theta_{CW}$  is  $\sim -142$  K. Fitting was performed using data in the higher temperature region to avoid deviation induced by the formation of short-range orderings at lower temperature.

### 5.3.5 Discussion on the magnetic ground state

A large frustration parameter,  $f \sim 100-1000$ , is a strong indication of quantum spin liquid [150]. Therefore, the magnetically disordered state of the  $n = 1$  sample can be a possible candidate. Here, we have to notify that identifying in laboratories a quantum spin liquid state is still circumstantial owing to the lack of a standard experimental definition. However, the probability of being a quantum spin liquid can be enhanced by excluding other counterparts. First, it is not a simple paramagnet due to the very intensive magnetic frustration. Moreover, according to the XMCD measurements, the linear  $M-H$  relationship of both Co and Cr elements persists up to 5 T with no saturation (Fig. needs added!). As a result, it is unlikely a superparamagnet. In fact, this can be further verified by calculating the ratio of remanence  $H_r$  to coercivity  $H_c$ . A superparamagnet typically has this value  $> 10$ , whereas it is only  $\sim 2$  for the  $n = 1$  sample as shown in the supplementary, referring to the high improbability of being a superparamagnetic phase.

As for other spin-disordered phases such as spin glass, when the thermal fluctuations become considerably small at low temperature, the localized spins will end up freezing in

random directions at a transition temperature  $T_f$ , with a distinct “cusp” exhibiting on the  $M - T$  curves [154]. This can be eliminated by the absence of any “cusp” behavior observed on the temperature-dependent XMCD of the  $n = 1$  sample. Last but not least, we can further rule out spin ice, an exotic state of matter which is the other type of geometrically frustrated magnet since the exchange interaction in this situation is usually ferromagnetic.

### 5.3.6 Phase diagram

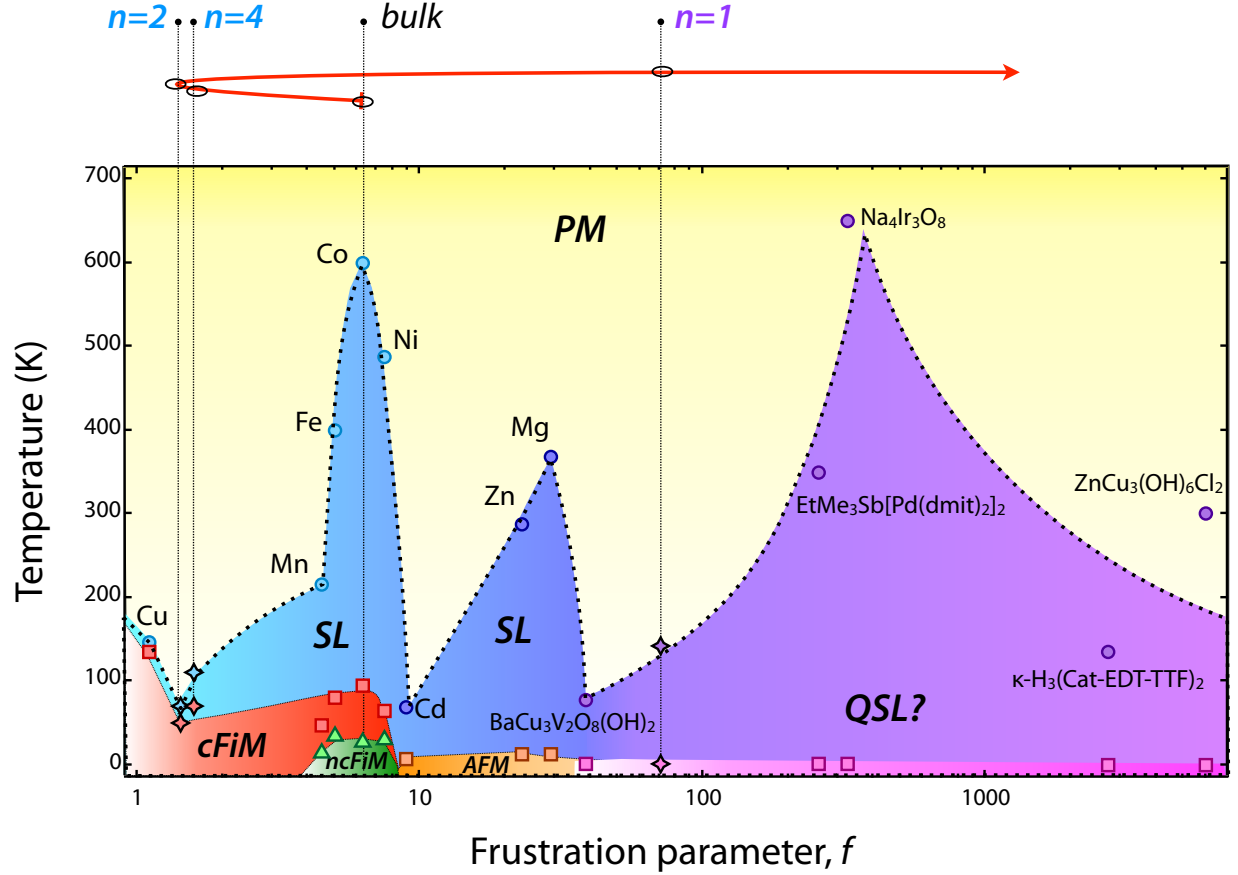
Finally, to elucidate the underlying mechanism of the observed evolution of magnetic ground state with CCO thickness, we established the “temperature – frustration parameter” phase diagram (Fig. 5.9) including our samples, other  $\text{ACr}_2\text{O}_4$  members [8, 9, 10, 11, 12, 13] and probable candidates of quantum spin liquid [14, 15, 16, 17, 18]. When the A site is a magnetic ion ( $A = \text{Cu, Mn, Fe, Co}$  and  $\text{Ni}$ ), the dominant inter-sublattice antiferromagnetic superexchange coupling  $J_{AB}$  favors the Neel-type ferrimagnetic configuration but still competes with the antiferromagnetic interaction within the pyrochlore B sublattice,  $J_{BB}$ , which induces weak geometrical frustration [127, 152]. The resultant magnetic ground state can be either collinear or non-collinear ferrimagnetic depending on the magnitude of frustration. On the other hand, when the A site is non-magnetic ( $A = \text{Cd, Zn}$  and  $\text{Mg}$ ), the purely antiferromagnetic coupled moments on the pyrochlore Cr sublattice are inherently with relatively strong geometrical frustration, maintaining the spin liquid state over a wide temperature range. However, since the quantum fluctuations are not strong enough, long-range antiferromagnetic orderings with complicated configurations can still occur at low temperature. Further increasing the quantum fluctuations could drive a system into the region with extremely high frustration, where the spin liquid state persists down to  $T = 0$  K (quantum spin liquid). It has been suggested this can be realized on lattices with reduced dimensionality or coordination [109]. So far, only a few systems have been reported as possible candidates belonging to this region (the right panel of Fig. 5.9 from  $\text{BaCu}_3\text{V}_2\text{O}_8(\text{OH})_2$  to  $\text{ZnCu}_3(\text{OH})_6\text{Cl}_2$ ). [14, 15, 16, 17, 18]

In our experiments, starting from the bulk-like  $\text{CoCr}_2\text{O}_4$ , the effect of reduced dimensionality could drive the electrons to be more localized, giving rise to an enhancement of the Hubbard repulsion  $U$ . It has been suggested by LSDA +  $U$  calculation in this compound that increasing Hubbard  $U$  could lead to a decrease in strength of all coupling constants

[155], which is directly related to the Curie-Weiss temperature  $\Theta_{CW}$  by mean-field theory. Moreover, it was also noticed that the decrease of  $J_{BB}$  is faster compared to  $J_{AB}$  [155], which would suppress the competing effect and lower the magnetic frustration. Results of the  $n = 4$  and  $2$  samples are consistent with this scenario, where we observe markedly smaller  $\Theta_{CW}$  and frustration parameters  $f$ . As a result, the magnetic behavior is shifted to the left side with a collinear ferrimagnetic configuration as the ground state. Surprisingly, however, the extremely large  $f$  of the  $n = 1$  sample indicates its behavior bypasses the whole  $\text{ACr}_2\text{O}_4$  regions with no bulk-like imprint. Such a sharp increase of  $f$  may have several contributions. First, since  $n = 1$  is on the verge of the two-dimensional limit leaving only four geometrically frustrated cation planes as shown in Fig. 1b, quantum fluctuations are expected to have a large increase. Second, we note that due to the entirely breaking of the translational symmetry along the (111) direction, the exchange coupling within each planes tends to be more dominant, which can also increase  $f$  to a profound scale. Therefore, despite  $\Theta_{CW}$  is still with close magnitude, no long-range magnetic ordering presents down to 2 K for the  $n = 1$  sample.

#### 5.4 Summary

In conclusion, we have provided detailed insights into the evolution of magnetic ground state of (111)-oriented  $n\text{CCO}/3\text{AlO}$  superlattices. The significantly large frustration parameter at the ultrathin limit ( $n = 1$ ) reveals the crossover from bulk-like behavior to the creation of a novel quasi-two-dimensional geometrically frustrated lattice. Our results highlight the opportunities towards the realization of exotic quantum many-body state such as quantum spin liquid and also demonstrate the potential of geometrical lattice engineering for manipulating properties and functionalities of complex oxides.



**Figure 5.9:** Phase diagram as a function of frustration parameter. Definition of the symbols: PM — paramagnet, SL — spin liquid, cFiM — collinear ferrimagnet, ncFiM — non-collinear ferrimagnet, AFM — antiferromagnet, QSL — quantum spin liquid. The dotted line crossing the circle points represents the fitted Curie-Weiss temperature  $\Theta_{CW}$ . Data for  $M\text{Cr}_2\text{O}_4$  with different A sites are taken from literatures (M = Cu [8], Mn [9], Fe [10], Co [11], Ni [8, 12], Cd [13], Zn [13], Mg [13]). Data for the superlattices with  $n = 1, 2$  and  $4$  are displayed in diamond. The red arrow on the top represents the evolution of the frustration effect in (111)-oriented CCO towards the two-dimensional limit. Experimental results of possible QSL candidates with various types of lattice are plotted for comparison. ( $\text{EtMe}_3\text{Sb}[\text{Pd}(\text{admit})_2]_2$  [14] and  $\kappa - \text{H}_3(\text{Cat-EDT-TTF})_2$  [15] with triangle lattice;  $\text{Na}_4\text{Ir}_3\text{O}_8$  [16] with hyperkagome lattice;  $\text{BaCu}_3\text{V}_2\text{O}_8(\text{OH})_2$  [17] and  $\text{ZnCu}_3(\text{OH})_6\text{Cl}_2$  [18] with kagome lattice)

## Chapter 6

### Conclusions and future prospects

#### 6.1 Conclusions

The main purpose of this dissertation is to design and discover artificial systems with emergent phenomena by means of heteroepitaxial engineering, which in turn corroborates our understanding about the fundamental physics of strongly correlated electrons. By applying the strategy of interface engineering, a novel two-dimensional electron gases (2DEGs) system is realized in ultrathin  $\text{YTiO}_3/\text{CaTiO}_3$  superlattices growth on  $\text{NdGaO}_3$  substrate with pulsed laser deposition. This system is one of the very few non- $\text{SrTiO}_3$ -based 2DEGs. A combination of reflection-high-energy-electron-diffraction, X-ray diffraction and reflectivity characterizations confirm the layer-by-layer growth of the films with exceptionally smooth surface morphology and sharp interfaces. Transport measurements reveal that the superlattices exhibit metallic conduction from 300 K to 2 K with electrons as the charge carriers. These findings suggest another route to realizing complex oxide 2DEGs without hindering effects from complex behavior of  $\text{SrTiO}_3$  and provides a new playground to investigate possible interplay between magnetism and superconductivity at such interfaces. In order to investigate the magnetic frustration phenomena, unconventional (111)-oriented  $\text{CoCr}_2\text{O}_4$  (CCO) thin films and  $\text{CoCr}_2\text{O}_4/\text{Al}_2\text{O}_3$  (CCO/AIO) heterostructures have been fabricated on sapphire (0001) substrate for the first time. In this case, geometrically frustrated lattices are formed intrinsically. The comprehensive structural, electronic and magnetic characterizations demonstrate the high quality of the samples with expected epitaxial orientation, proper chemical valence and stoichiometry. Both the CCO and the AIO layer thickness can be digitally controlled. These results provide solid evidences on experimental realization of the geometrical lattice engineering (GLE) concept using state-of-the-art thin film deposition technique. Also, it paves a way for building artificial quasi-2D transition metal heterostructures on which a plethora of intriguing quantum phenomena can be expected.

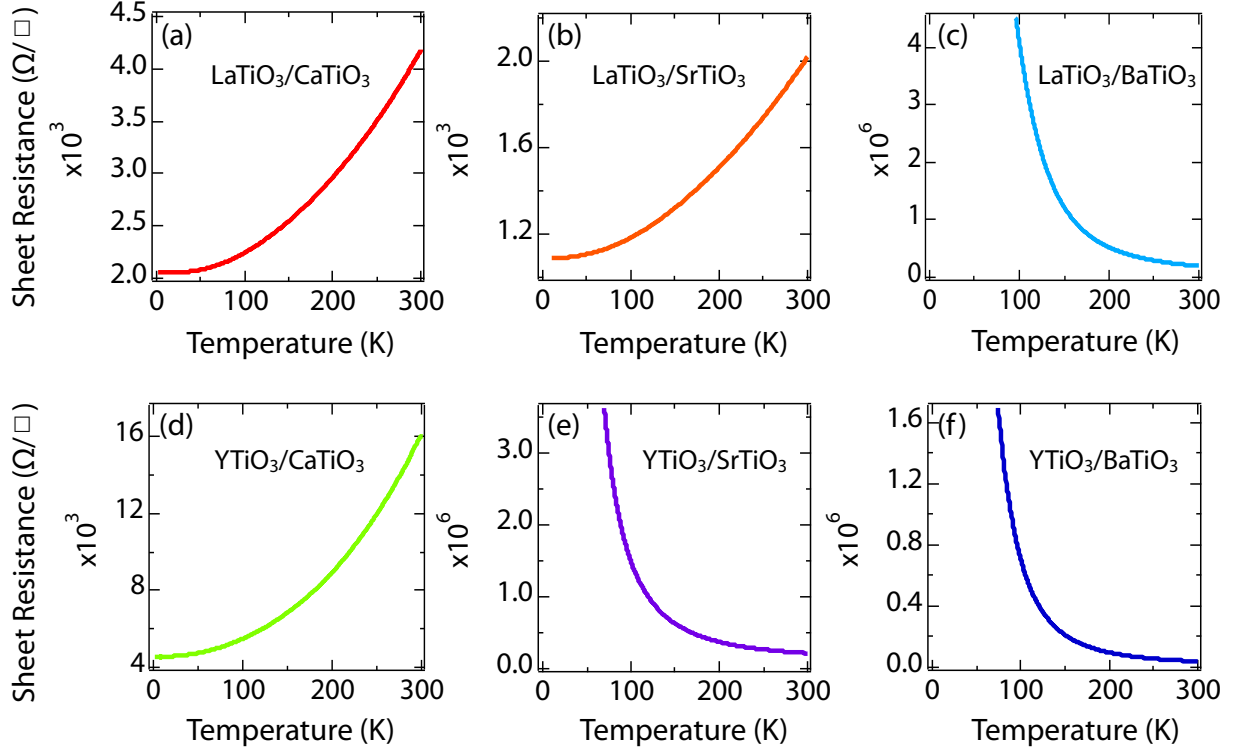
Advanced electronic and magnetic characterizations of the CCO/AIO superlattices provide detailed insights into the evolution of the magnetic ground state. As the thickness of CCO is decreased towards the 2D limit, the non-collinear ferrimagnetic state in the bulk trans-

forms into a collinear ferrimagnetic state. Finally, at the ultrathin limit with only one unit cell of CCO, a drastically large frustration parameter is observed, revealing the crossover from a magnetically ordered state to the creation of a novel quasi-2D geometrically frustrated state, which is a possible candidate of quantum spin liquid. These results highlight the opportunities on realization of exotic quantum many-body states and also demonstrate the potential of GLE for manipulating properties and functionalities of complex oxides.

## 6.2 Future prospects

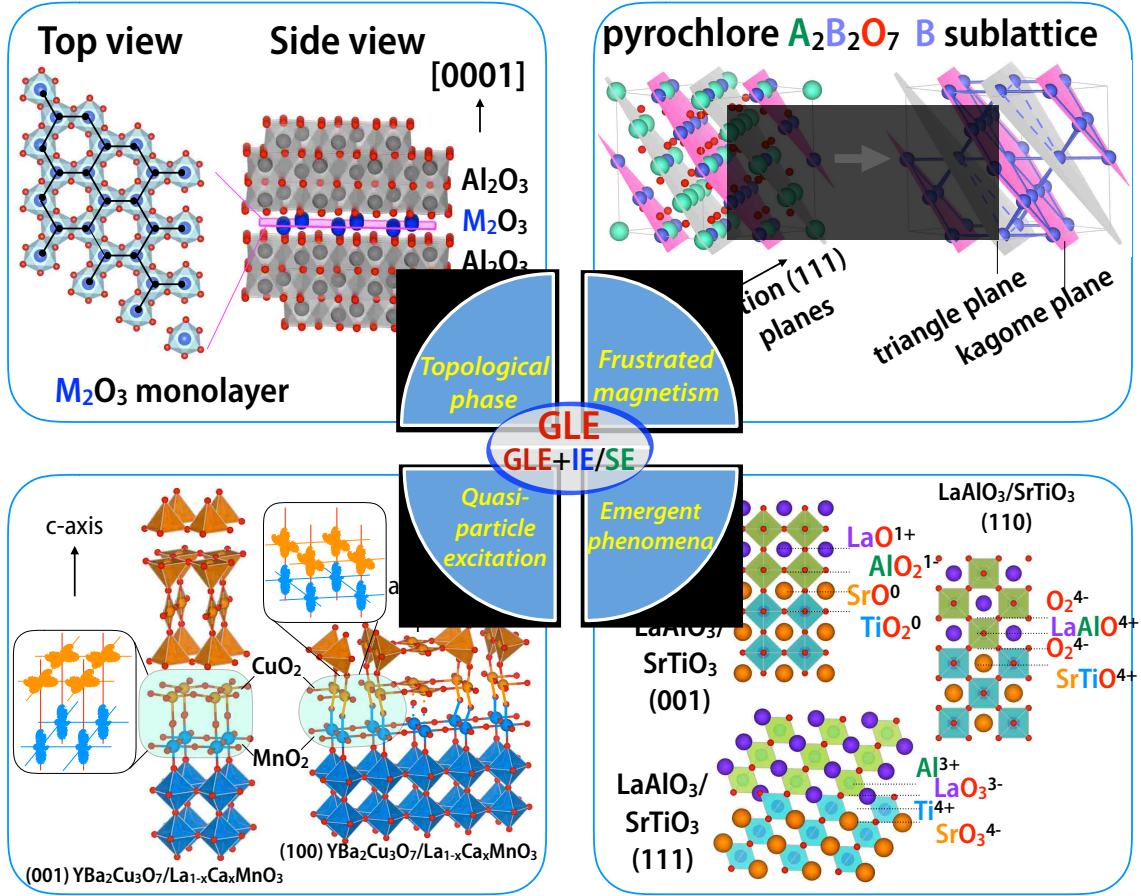
There are several promising directions which may follow from the work discussed in this dissertation. With respect to the CTO/YTO project, a rather fundamental and essential question is raised if one summarizing the transport behaviors of other members belonging to the  $ATO/RTO$  ( $A$  is a alkaline-earth element and  $R$  is a rare-earth element) family: Is the “polar discontinuity” model [80] rigorously true for every of the 2DEG systems? Specifically as shown in Fig. 6.1, any of these combination will give rise the same polar mismatch pattern at the interface. However, some of the systems are metallic [Fig. 6.1 (a), (b) and (d)] while others are insulating [(c), (e), and (f)]. These observations immediately indicate that some important factors are missing, which seem to play a significant role in determining the conductivity of such interfaces. One possible suspect is the specific  $TiO_6$  octahedral distortions and the  $A-O-R$  bond angles at the interface, which will effectively vary the Ti  $d$  bandwidth. In order to fully elucidate this question, theoretically doing *ab initio* calculations on the Ti  $d$  and O  $p$  subband structures should be a meaningful way to clarify whether and what is the true conduction band. Also it can help to predict their magnetic properties. On the experimental side, high-resolution transmission electron microscopy images will be very helpful to shed light on detailed structural information at the interface such as the distortions, octahedral rotations and symmetries, and the  $A-O-R$  bond angles.

With respect to the GLE, currently researches have been done mainly with emphasis on systems layered along the cubic (or pseudo-cubic) (111)-orientation of perovskites and spinels. However, the GLE concept is certainly not restricted to those systems and its realization opens wide opportunities for experimentalists to fabricate other interesting lattices in the heterostructure form. For instance, apart from spinel-type compounds, 2D frustrated lattices also appear in ultra-thin (111)-oriented pyrochlore (chemical formula:



**Figure 6.1:** (a) - (f) Temperature dependence of sheet resistance of *ATO/RTO* interfaces ( $A = \text{Ca, Sr, Ba}$ ;  $R = \text{La, Y}$ ).

$\text{A}_2\text{B}_2\text{O}_7$ ) structures (Fig. 6.2, right top panel). This can be easily understood since the B sublattice in the pyrochlore structure is identical to that of spinel. Several theoretical works [41, 46, 156, 157] have predicted the emergence of topological states with different B cations, while the experimental work on fabricating (111) pyrochlore films have been recently initiated [158, 159, 160]. Additionally, it was theoretically proposed that a monolayer of corundum-type (chemical formula:  $\text{M}_2\text{O}_3$ ) structure grown along the (0001) direction could also form the graphene-like honeycomb lattice geometry [161] analogous to the perovskite (111) bilayers (Fig. 6.2, left panel on the top). To push this field further, one can envision that a combination of GLE with other designing approaches should allow for even more exotic phases. A fusion of GLE and interface engineering (IE) may enable new tailor-made phenomena since for heterostructures the mismatches at the interface should be profoundly altered by the epitaxial orientation. For instance, assuming the “polar discontinuity” model is right, the polar mismatch patterns then vary with the orientation of the heterostructure. This can be utilized to tune the carrier density and mobility of the 2DEGs. Toward experimental realization of this idea a pioneering work has been reported



**Figure 6.2:** Summary and outlook on GLE. The upper panel displays other possible routes to topological phase and frustrated magnetism by applying pure GLE. The bottom panel presents the combination of GLE with IE or SE to establish new systems with intriguing physics such as quasi-particle excitation and emergent phenomena.

on the growth of the prototypical  $LaAlO_3/SrTiO_3$  system with (001), (110), and (111) interfaces (Fig. 6.2, right panel on the bottom) [162]. Another interesting theory proposal is the study on the interface between (100)-oriented high-temperature superconducting cuprate  $YBa_2Cu_3O_7$  (YBCO) and colossal magnetoresistance manganite  $La_xCa_{1-x}MnO_3$  (LCMO). Compared to the extensively investigated (001) YBCO/LCMO interface where the nodes of Cu  $d_{x^2-y^2}$  orbital are in the  $ab$  plane, the (100)-oriented YBCO has nodes of the  $d_{x^2-y^2}$  orbital out of the  $CuO_2$  plane (see Fig. 6.2, left panel on the bottom). This unique orbital coupling pattern is crucial for the emergence of the exotic Majorana state [163]. Furthermore, the combination of GLE and strain engineering (IE) may open another interesting dimension for controlled modifications of the bond-length and bond-angle in structural units by epitaxial strain along the unconventional crystallographic axes.



All in all, with the modern state-of-the-art thin-film fabrication methods, the notion of GLE can be experimentally realized and used as another important control knob. Despite the challenges of layering with atomic precision along unconventional crystallographic directions, GLE has excellent potential for the discovery of novel electronic, magnetic, and topological phases with complex functional materials.

## Bibliography

- [1] P. A. Cox, *Transition metal oxides*. Oxford University Press, 1992.
- [2] D. Khomskii, *Transition metal compounds*. Cambridge University Press, 2014.
- [3] J. Chakhalian, J. W. Freeland, A. J. Millis, C. Panagopoulos, and J. M. Rondinelli, “Colloquium: Emergent properties in plane view: strong correlations at oxide interfaces,” *Reviews of Modern Physics*, vol. 86, p. 1189, 2014.
- [4] J. Stöhr and H. C. Siegmann, *Magnetism: from fundamental to nanoscale dynamics*. Berlin : Springer, 2006.
- [5] R. V. Chopdekar, M. Liberati, Y. Takamura, L. F. Kourkoutis, J. S. Bettinger, B. B. Nelson-cheeseman, E. Arenholz, A. Doran, A. Scholl, D. A. Muller, and Y. Suzuki, “Magnetism at spinel thin film interfaces probed through soft X-ray spectroscopy techniques,” *Journal of Magnetism and Magnetic Materials.*, vol. 322, pp. 2915–2921, 2010.
- [6] J. B. Goodenough, *Magnetism and the Chemical Bond*. Interscience, New York, 1974, 1974.
- [7] S. V. Vonsovskii, *Magnetism Volume Two*. Wiley, New York, 1963, 1963.
- [8] M. R. Suchomel, D. P. Shoemaker, L. Ribaud, M. C. Kemei, and R. Seshadri, “Spin-induced symmetry breaking in orbitally ordered  $\text{NiCr}_2\text{O}_4$  and  $\text{CuCr}_2\text{O}_4$ ,” *Physical Review B*, vol. 86, p. 054406, 2012.
- [9] K. Dey, S. Majumdar, and S. Giri, “Ferroelectricity in spiral short-range-ordered magnetic state of spinel  $\text{MnCr}_2\text{O}_4$ : Significance of topological frustration and magneto elastic coupling,” *Physical Review B*, vol. 90, p. 184424, 2014.
- [10] G. Shirane, D. E. Cox, and S. J. Pickart, “Magnetic structures in  $\text{FeCr}_2\text{S}_4$  and  $\text{FeCr}_2\text{O}_4$ ,” *Journal of Applied Physics*, vol. 35, p. 954, 1964.
- [11] V. Tsurkan, S. Zherlitsyn, S. Yasin, V. Felea, Y. Skourski, J. Deisenhofer, H. A. K. von Nidda, J. Wosnitza, and A. Loidl, “Unconventional magnetostructural transition in  $\text{CoCr}_2\text{O}_4$  at high magnetic fields,” *Physical Review Letters*, vol. 110, p. 115502, 2013.
- [12] K. Tomiyasu and I. Kagomiya, “Magnetic structure of  $\text{NiCr}_2\text{O}_4$  studied by neutron scattering and magnetization measurements,” *Journal of the Physical Society of Japan*, vol. 73, pp. 2539–2542, 2004.
- [13] Kemei, M. C. *et al.*, “Crystal structures of spin-Jahn-Teller-ordered  $\text{MgCr}_2\text{O}_4$  and  $\text{ZnCr}_2\text{O}_4$ ,” *Journal of Physics: Condensed Matter*, vol. 25, p. 326001, 2013.

- [14] T. Itou, A. Oyamada, S. Maegawa, M. Tamura, and R. Kato, “Quantum spin liquid in the spin-1/2 triangular antiferromagnet  $\text{EtMe}_3\text{Sb}[\text{Pd}(\text{dmit})_2]_2$ ,” *Physical Review B*, vol. 77, p. 104413, 2008.
- [15] T. t. Isono, “Gapless quantum spin liquid in an organic spin-1/2 triangular-lattice  $\kappa - \text{H}_3(\text{Cat-EDT-TTF})_2$ ,” *Physical Review Letters*, vol. 112, p. 177201, 2014.
- [16] Y. Okamoto, M. Nohara, H. Aruga-Katori, and H. Takagi, “Spin-liquid state in the  $S = 1/2$  hyperkagome antiferromagnet  $\text{Na}_4\text{Ir}_3\text{O}_8$ ,” *Physical Review Letters*, vol. 99, p. 137207, 2007.
- [17] Y. Okamoto, H. Yoshida, and Z. Hiroi, “Vesignieite  $\text{BaCu}_3\text{V}_2\text{O}_8(\text{OH})_2$  as a candidate spin-1/2 kagome antiferromagnet,” *Journal of the Physical Society of Japan*, vol. 78, p. 033701, 2009.
- [18] J. S. t. Helton, “Spin dynamics of the spin-1/2 kagome lattice antiferromagnet  $\text{ZnCu}_3(\text{OH})_6\text{Cl}_2$ ,” *Physical Review Letters*, vol. 98, p. 107204, 2007.
- [19] P. Fazekas, *Lecture notes on electron correlation and magnetism*. World Scientific, 1999.
- [20] D. Khomskii, *Basic aspects of the quantum theory of solids*. Cambridge University Press, 2010.
- [21] L. Pauling, “The principles determining the structure of complex ionic crystals,” *Journal of the American Chemical Society*, vol. 51, pp. 1010–1026, 1929.
- [22] L. Pauling, *The nature of the chemical bond and the structure of molecules and crystals: an introduction to modern structural chemistry*. Ithaca (NY): Cornell University Press., 1960.
- [23] V. Goldschmidt, “Die Gesetze der Krystallochemie,” *Naturwissenschaften*, vol. 14, pp. 477–485, 1926.
- [24] H. A. Jahn and E. Teller, “Stability of polyatomic molecules in degenerate electronic states. I. Orbital degeneracy,” *Proceedings of the Royal Society*, vol. 161, p. 220, 1937.
- [25] N. W. Ashcroft and N. D. Mermin, *Solid state physics*. New York : Holt, Rinehart and Winston, 1976.
- [26] C. Kittel, *Introduction to solid state physics*, 8th ed. Wiley, 2004.
- [27] J. Zaanen, G. A. Sawatzky, and J. W. Allen, “Band gaps and electronic structure of transition-metal compounds,” *Physical Review Letters*, vol. 55, p. 418, 1985.
- [28] H. Y. Hwang, Y. Iwasa, M. Kawasaki, B. Keimer, N. Nagaosa, and Y. Tokura, “Emergent phenomena at oxide interfaces,” *Nature materials*, vol. 11, no. 2, pp. 103–113, 2012.

- [29] J. Chakhalian, A. J. Millis, and J. Rondinelli, “Whither the oxide interface,” *Nature Materials*, vol. 11, p. 92, 2012.
- [30] P. Zubko, S. Gariglio, M. Gabay, P. Ghosez, and J.-M. Triscone, “Interface physics in complex oxide heterostructures,” *Annual Review of Condensed Matter Physics*, vol. 2, p. 141, 2011.
- [31] S. Stemmer and S. J. Allen, “Two-dimensional electron gases at complex oxide interfaces,” *Annual Review of Condensed Matter Physics*, vol. 44, p. 151, 2014.
- [32] K. R. Poeppelmeier and J. M. Rondinelli, “Oxide interfaces: mismatched lattices patched up,” *Nature Chemistry*, vol. 8, p. 292, 2016.
- [33] J. Liu, M. Kargarian, M. Kareev, B. Gray, P. Ryan, A. Cruz, N. Tahir, Y.-D. Chuang, J. Guo, J. Rondinelli, J. Freeland, G. Fiete, and J. Chakhalian, “Heterointerface engineered electronic and magnetic phases of NdNiO<sub>3</sub> thin films,” *Nature Communications*, vol. 4, p. 2714, 2013.
- [34] K. Choi, M. Biegalski, Y. Li, A. Sharan, J. Schubert, R. Uecker, P. Reiche, Y. Chen, X. Pan, V. Gopalan, L.-Q. Chen, D. Schlom, and C. Eom, “Enhancement of ferroelectricity in strained BaTiO<sub>3</sub> thin films,” *Science*, vol. 306, p. 1005, 2004.
- [35] J. Chakhalian, J. Rondinelli, J. Liu, B. Gray, M. Kareev, E. Moon, N. Prasai, J. Cohn, M. Varela, I. Tung, M. Bedzyk, S. Altendorf, F. Strigari, B. Dabrowski, L. Tjeng, P. Ryan, and J. Freeland, “Asymmetric orbital?lattice interactions in ultrathin correlated oxide films,” *Physical Review Letters*, vol. 107, p. 116805, 2011.
- [36] Y. Cao, X. Liu, P. Shafer, S. Middey, D. Meyers, M. Kareev, Z. Zhong, J.-W. Kim, P. Ryan, E. Arenholz, and J. Chakhalian, “Anomalous orbital structure in a spinel-perovskite interface,” *Npj Quantum Materials*, vol. 1, p. 16009, 2016.
- [37] E. B. *et al*, “Orbital reflectometry of oxide heterostructures,” *Nature Materials*, vol. 10, pp. 189–193, 2011.
- [38] J. Chakhalian, J. W. Freeland, G. Srajer, J. Stremper, G. Khaliullin, J. C. Cezar, T. Charlton, R. Dalgliesh, C. Bernhard, G. Cristiani, H.-U. Habermeier, and B. Keimer, “Magnetism at the interface between ferromagnetic and superconducting oxides,” *Nature Physics*, vol. 2, pp. 244–248, 2006.
- [39] D. Xiao, W. Zhu, Y. Ran, N. Nagaosa, and S. Okamoto, “Asymmetric orbital?lattice interactions in ultrathin correlated oxide films,” *Nature Communications*, vol. 2, p. 596, 2011.
- [40] K. Yang, W. Zhu, D. Xiao, S. Okamoto, Z. Wang, and Y. Ran, “Possible interaction-driven topological phases in (111) bilayers of LaNiO<sub>3</sub>,” *Physical Review B*, vol. 84, p. 201104(R), 2011.

- [41] A. Rüegg and G. A. Fiete, “Topological insulators from complex orbital order in transition-metal oxides heterostructures,” *Physical Review B*, vol. 84, p. 201103(R), 2011.
- [42] X. Hu, A. Rüegg, and G. A. Fiete, “Topological phases in layered pyrochlore oxide thin films along the [111] direction,” *Physical Review B*, vol. 86, p. 235141, 2012.
- [43] Y. Wang, Z. Wang, Z. Fang, and X. Dai, “Interaction-induced quantum anomalous Hall phase in (111) bilayer of  $\text{LaCoO}_3$ ,” *Physical Review B*, vol. 91, p. 125139, 2015.
- [44] H. Guo and M. Franz, “Topological insulator on the kagome lattice,” *Physical Review B*, vol. 80, p. 113102, 2009.
- [45] T. Han, J. S. Helton, S. Chu, D. G. Nocera, J. A. Rodriguez-Rivera, C. Broholm, and Y. S. Lee, “Fractionalized excitations in the spin-liquid state of a kagome-lattice antiferromagnet,” *Nature*, vol. 492, p. 406, 2012.
- [46] H. Guo and M. Franz, “Three-dimensional topological insulators on the pyrochlore lattice,” *Physical Review Letters*, vol. 103, p. 206805, 2009.
- [47] X. Hu, Z. Zhong, and G. Fiete, “First principles prediction of topological phases in thin films of pyrochlore iridates,” *Scientific Reports*, vol. 5, p. 11072, 2015.
- [48] S. Okamoto, “Doped Mott insulators in (111) bilayers of perovskite transition-metal oxides with a strong spin-orbit coupling,” *Physical Review Letters*, vol. 110, p. 066403, 2013.
- [49] A. Cook and A. Paramakanti, “Double perovskite heterostructures: magnetism, Chern bands and Chern insulators,” *Physical Review Letters*, vol. 113, p. 077203, 2014.
- [50] J. Lado, V. Pardo, and D. Baldomir, “*Ab initio* study of  $\mathbb{Z}_2$  topological phases in perovskite (111)  $(\text{SrTiO}_3)_7/(\text{SrIrO}_3)_2$  and  $(\text{KTaO}_3)_7/(\text{KPtO}_3)_2$  multilayers,” *Physical Review B*, vol. 88, p. 155119, 2013.
- [51] T. Cai, F. W. X. Li, S. Ju, J. Feng, and C. Gong, “Single-spin Dirac fermion and Chern insulator based on simple oxides,” *Nano Letters*, vol. 15, p. 6434, 2015.
- [52] S. Middey, D. Meyers, M. Kareev, E. J. Moon, B. A. Gray, X. Liu, J. W. Freeland, and J. Chakhalian, “Epitaxial growth of (111)-oriented  $\text{LaAlO}_3/\text{LaNiO}_3$  ultra-thin superlattices,” *Applied Physics Letters*, vol. 101, p. 261602, 2012.
- [53] X. Liu, D. Choudhury, Y. Cao, S. Middey, M. Kareev, D. Meyers, J.-W. Kim, P. Ryan, and J. Chakhalian, “Epitaxial growth of (111)-oriented spinel  $\text{CoCr}_2\text{O}_4/\text{Al}_2\text{O}_3$  heterostructures,” *Applied Physics Letters*, vol. 106, no. 7, p. 071603, 2015.

- [54] S. Middry, D. Meyers, D. Doennig, M. Kareev, X. Liu, Y. Cao, Z. Yang, J. Shi, L. Gu, P. J. Ryan, R. Pentcheva, J. W. Freeland, and J. Chakhalian, “Mott electrons in an artificial graphenelike crystal of rare-earth nickelate,” *Physical Review Letters*, vol. 116, p. 056801, 2016.
- [55] D. Hirai, J. Matsuno, and H. Takagi, “Fabrication of (111)-oriented  $\text{Ca}_{0.5}\text{Sr}_{0.5}\text{IrO}_3/\text{SrTiO}_3$  superlattices — a designed playground for honeycomb physics,” *APL materials*, vol. 3, p. 041508, 2015.
- [56] T. Anderson, S. Ryu, H. Zhou, L. Xie, J. Podkaminer, Y. Ma, J. Irwin, X. Pan, M. Rzchowski, and C. Eom, “Metastable honeycomb  $\text{SrTiO}_3/\text{SrIrO}_3$  heterostructures,” *Applied Physics Letters*, vol. 108, p. 151604, 2016.
- [57] G. Panomsuwan, O. Takai, and N. Saito, “Metastable honeycomb  $\text{SrTiO}_3/\text{SrIrO}_3$  heterostructures,” *Applied Physics Letters*, vol. 103, p. 112902, 2013.
- [58] B. Gray, H. Lee, J. Liu, J. Chakhalian, and J. W. Freeland, “Local electronic and magnetic studies of an artificial  $\text{La}_2\text{FeCrO}_6$  double perovskite,” *Applied Physics Letters*, vol. 97, p. 013105, 2010.
- [59] X. Liu, S. Middey, Y. Cao, M. Kareev, and J. Chakhalian, “Geometrical lattice engineering of complex oxide heterostructures: a designer approach to emergent quantum states,” *MRS Communications*, vol. 6, pp. 133–144, 2016.
- [60] R. Eason, Ed., *Pulsed laser deposition of thin films*. Hoboken, N. J. : Wiley-Interscience, 2007.
- [61] G. Koster, M. Huijben, and G. Rijnders, Eds., *Epitaxial growth of complex metal oxides*. Woodhead Publishing, 2015.
- [62] G. Koster and G. Rijnders, Eds., *In-situ characterization of thin film growth*. Woodhead Publishing, 2011.
- [63] D. Blank, G. Koster, G. Rijnders, E. Setten, P. Slycke, and H. Rogalla, “Epitaxial growth of oxides with pulsed laser interval deposition,” *Journal of Crystal Growth*, vol. 211, pp. 98–105, 2000.
- [64] W. Braun, *Applied RHEED: reflection high-energy electron diffraction during crystal growth*. Springer, 1999.
- [65] A. Ichimiya and P. I. Cohen, *Reflection high-energy electron diffraction*. Cambridge University Press, 2004.
- [66] D. Bowen and B. Tanner, *High resolution X-ray diffractometry and topography*. Taylor & Francis, 1998.
- [67] F. de Groot and A. Kotani, *Core level spectroscopy of solids*. Taylor & Francis, 2008.

- [68] E. Beaurepaire, H. Bulou, F. Scheurer, and K. Jean-Paul, Eds., *Magnetism and synchrotron radiation*. Springer-Verlag Berlin Heidelberg, 2010.
- [69] B. T. Thole, P. Carra, F. Sette, and G. van der Laan, “X-ray circular dichroism as a probe of orbital magnetization,” *Physical Review Letters*, vol. 68, pp. 1943–1946, 1992.
- [70] P. Carra, B. T. Thole, M. Altarelli, and X. Wang, “X-ray circular dichroism and local magnetic fields,” *Physical Review Letters*, vol. 70, pp. 694–697, 1993.
- [71] C. T. Chen, Y. U. Idzerda, H.-J. Lin, N. V. Smith, G. Meigs, E. Chaban, G. H. Ho, E. Pellegrin, and F. Sette, “Experimental confirmation of the X-ray magnetic circular dichroism sum rules for iron and cobalt,” *Physical Review Letters*, vol. 75, pp. 152–155, 1995.
- [72] J. W. Freeland, J. J. Kavich, K. E. Gray, L. Ozyuzer, H. Zheng, J. F. Mitchell, M. P. Warusawithana, P. Ryan, X. Zhai, R. H. Kodama, and J. N. Eckstein, “Suppressed magnetization at the surfaces and interfaces of ferromagnetic metallic manganites,” *Journal of Physics: Condensed Matter*, vol. 19, p. 315210, 2007.
- [73] Y. Zhu, Ed., *Modern techniques for characterizing magnetic materials*. Springer Science & Business Media, 2005.
- [74] J. F. Ankner and G. P. Felcher, “Polarized neutron reflectometry,” *Journal of Magnetism and Magnetic Materials*, vol. 200, pp. 741–754, 1999.
- [75] H. Zabel and K. Theis-Bröhl, “Polarized neutron reflectivity and scattering studies of magnetic heterostructures,” *Journal of Physics: Condensed Matter*, vol. 15, p. S505, 2003.
- [76] C. Majkrzak, “Neutron reflectometry studies of thin films and multilayered materials,” *Acta Physica Polonica A*, vol. 96, pp. 81–99, 1999.
- [77] X. Liu, D. Choudhury, Y. Cao, M. Kareev, S. Middey, and J. Chakhalian, “Metallic interface in non-SrTiO<sub>3</sub> based titanate superlattice,” *Applied Physics Letters*, vol. 107, p. 191602, 2015.
- [78] S. Stemmer and S. J. Allen, “Two-dimensional electron gases at complex oxide interfaces,” *Annual Review of Materials Research*, vol. 44, p. 151, 2014.
- [79] N. C. Bristowe, P. Ghosez, P. B. Littlewood, and E. Artacho, “The origin of two-dimensional electron gases at oxide interfaces: insights from theory,” *Journal of Physics: Condensed Matter*, vol. 26, p. 143201, 2014.
- [80] N. Nakagawa, H. Y. Hwang, and D. A. Muller, “Why some interfaces cannot be sharp,” *Nature Materials*, vol. 5, p. 204, 2006.
- [81] P. Zubko, S. Gariglio, M. Gabay, P. Ghosez, and J.-M. Triscone, “Interface physics in complex oxide heterostructures,” *Annual Review of Condensed Matter Physics*, vol. 2, p. 141, 2011.

- [82] I. Žutić, J. Fabian, and S. D. Sarma, “Spintronics: fundamentals and applications,” *Reviews of Modern Physics*, vol. 76, p. 323, 2004.
- [83] J. Mannhart and D. G. Schlom, “Oxide interfaces — an opportunity for electronics,” *Science*, vol. 327, p. 1607, 2004.
- [84] A. Ohtomo and H. Y. Hwang, “A high-mobility electron gas at the LaAlO<sub>3</sub>/SrTiO<sub>3</sub> heterointerface,” *Nature*, vol. 427, p. 423, 2004.
- [85] P. Perna, D. Maccariello, M. Radovic, U. S. di Uccio, I. Pallecchi, M. Codda, D. Marré, C. Cantoni, J. Gazquez, M. Varela, S. J. Pennycook, and F. M. Granoz, “Conducting interfaces between band insulating oxides: The LaGaO<sub>3</sub>/SrTiO<sub>3</sub> heterostructure,” *Applied Physics Letters*, vol. 97, p. 152111, 2010.
- [86] Y. Hotta, T. Susaki, and H. Y. Hwang, “Polar discontinuity doping of the LaVO<sub>3</sub>/SrTiO<sub>3</sub> interface,” *Physical Review Letters*, vol. 99, p. 236805, 2007.
- [87] A. Ohtomo, D. A. Muller, J. L. Grazul, and H. Y. Hwang, “Artificial charge-modulation in atomic-scale perovskite titanate superlattices,” *Nature*, vol. 419, p. 378, 2002.
- [88] S. Raghavan, J. Y. Zhang, and S. Stemmer, “Two-dimensional electron liquid at the (111) SmTiO<sub>3</sub>/SrTiO<sub>3</sub> interface,” *Applied Physics Letters*, vol. 106, p. 132104, 2015.
- [89] P. Moetakef, Y. A. Cain, D. G. Ouellette, J. Y. Zhang, D. O. Klenov, A. Janotti, C. G. V. de Walle, S. Rajan, S. J. Allen, and S. Stemmer, “Electrostatic carrier doping of GdTiO<sub>3</sub>/SrTiO<sub>3</sub> interfaces,” *Applied Physics Letters*, vol. 99, p. 232116, 2011.
- [90] D. F. Li, Y. Wang, and J. Y. Dai, “Tunable electronic transport properties of DyScO<sub>3</sub>/SrTiO<sub>3</sub> polar heterointerface,” *Applied Physics Letters*, vol. 98, p. 122108, 2011.
- [91] K. Zou, S. Ismail-Beigi, K. Kisslinger, X. Shen, D. Su, F. J. Walker, and C. H. Ahn, “LaTiO<sub>3</sub>/KTaO<sub>3</sub> interfaces: A new two-dimensional electron gas system,” *APL materials*, vol. 3, p. 036104, 2015.
- [92] K. A. Muller and H. Burkard, “SrTiO<sub>3</sub>: An intrinsic quantum paraelectric below 4 K,” *Physical Review B*, vol. 19, p. 3593, 1979.
- [93] P. Moetakef, J. R. Williams, D. G. Ouellette, A. P. Kajdos, D. Goldhaber-Gordon, S. J. Allen, and S. Stemmer, “Carrier-controlled ferromagnetism in SrTiO<sub>3</sub>,” *Physical Review X*, vol. 2, p. 021014, 2012.
- [94] C. A. Jackson and S. Stemmer, “Interface-induced magnetism in perovskite quantum wells,” *Physical Review B*, vol. 88, p. 180403(R), 2013.
- [95] H. W. Jang, D. A. Felker, C. W. Bark, Y. Wang, M. K. Niranjan, C. T. Nelson, Y. Zhang, D. Su, C. M. Folkman, S. H. Baek, S. Lee, K. Janicka, Y. Zhu, X. Q. Pan,



- D. D. Fong, E. Y. Tsymbal, M. S. Rzchowski, and C. B. Eom, "Metallic and insulating oxide interfaces controlled by electronic correlations," *Science*, vol. 331, p. 886, 2011.
- [96] N. Ganguli and P. J. Kelly, "Tuning ferromagnetism at interfaces between insulating perovskite oxides," *Physical Review Letters*, vol. 113, p. 127201, 2014.
- [97] Y. Okimoto, T. Katsufuji, Y. Okada, T. Arima, and Y. Tokura, "Optical spectra in (La,Y)TiO<sub>3</sub>: Variation of Mott-Hubbard gap features with change of electron correlation and band filling," *Physical Review B*, vol. 51, p. 9581, 1995.
- [98] S. C. Chae, Y. J. Chang, S. S. Seo, T. W. Noh, D.-W. Kim, and C. U. Jung, "Epitaxial growth and the magnetic properties of orthorhombic YTiO<sub>3</sub> thin films," *Applied Physics Letters*, vol. 89, p. 182512, 2006.
- [99] R. Ali and M. Yashima, "Space group and crystal structure of the perovskite CaTiO<sub>3</sub> from 296 to 1720 K," *Journal of Solid State Chemistry*, vol. 178, p. 2867, 2005.
- [100] K. Ueda, H. Yanagi, H. Hosono, and H. Kawazoe, "Study on electronic structure of CaTiO<sub>3</sub> by spectroscopic measurements and energy band calculations," *Journal of Physics: Condensed Matter*, vol. 11, p. 3535, 1999.
- [101] D. L. Proffit, H. W. Jang, S. Lee, C. T. Nelson, X. Q. Pan, M. S. Rzchowski, and C. B. Eom, "Influence of symmetry mismatch on heteroepitaxial growth of perovskite thin films," *Applied Physics Letters*, vol. 93, p. 111912, 2008.
- [102] M. Kareev, Y. Cao, X. Liu, S. Middey, D. Meyers, and J. Chakhalian, "Metallic conductance at the interface of tri-color titanate superlattices," *Applied Physics Letters*, vol. 103, p. 231605, 2013.
- [103] L. Bjaalie, B. Himmetoglu, L. Weston, A. Janotti, and C. G. V. de Walle, "Oxide interfaces for novel electronic applications," *New Journal of Physics*, vol. 16, p. 025005, 2014.
- [104] E. Mikheev, B. Himmetoglu, A. P. Kajdos, P. Moetakef, T. A. Cain, C. G. V. de Walle, and S. Stemmer, "Limitations to the room temperature mobility of two- and three-dimensional electron liquids in SrTiO<sub>3</sub>," *Applied Physics Letters*, vol. 106, p. 062102, 2015.
- [105] A. Verma, A. P. Kajdos, T. A. Cain, and S. Stemmer, "Intrinsic mobility limiting mechanisms in lanthanum-doped strontium titanate," *Physical Review Letters*, vol. 112, p. 216601, 2014.
- [106] F. Iga, H. Fukuchi, I. H. Inoue, and Y. Nishihara, "Magnetism and electrical properties in the perovskite-type Y<sub>1-x</sub>Ca<sub>x</sub>TiO<sub>3</sub>," *Japanese Journal of Applied Physics*, vol. 32, pp. 332-333, 1993.

- [107] C. A. Jackson, J. Y. Zhang, C. R. Freeze, and S. Stemmer, “Quantum critical behavior in confined SrTiO<sub>3</sub> quantum wells embedded in antiferromagnetic SmTiO<sub>3</sub>,” *Nature Communications*, vol. 5, p. 4258, 2014.
- [108] X. Liu, M. Kareev, Y. Cao, J. Liu, S. Middey, D. Meyers, J. W. Freeland, and J. Chakhalian, “Electronic and magnetic properties of (111)-oriented CoCr<sub>2</sub>O<sub>4</sub> epitaxial thin film,” *Applied Physics Letters*, vol. 105, no. 7, p. 042401, 2014.
- [109] F. Mila, “Quantum spin liquids,” *European Journal of Physics*, vol. 21, p. 499, 2000.
- [110] S. T. Bramwell and M. Gingras, “Spin ice state in frustrated magnetic pyrochlore materials,” *Science*, vol. 294, p. 1495, 2001.
- [111] S. Lee, H. Takagi, D. Louca, M. Matsuda, S. Ji, H. Ueda, Y. Ueda, T. Katsufuji, J. Chung, S. Park, S. Cheong, and C. Broholm, “Frustrated magnetism and cooperative phase transition in spinels,” *Journal of the Physical Society of Japan*, vol. 79, p. 011004, 2010.
- [112] A. P. Ramirez, “Strongly geometrically frustrated magnets,” *Annual Review of Materials Science*, vol. 24, p. 453, 1994.
- [113] J. S. Gardner, M. Gingras, and J. E. Greedan, “Magnetic pyrochlore oxides,” *Reviews of Modern Physics*, vol. 82, p. 53, 2010.
- [114] K. Binder and A. P. Young, “Spin glass: experimental facts, theoretical concepts, and open questions,” *Reviews of Modern Physics*, vol. 58, p. 801, 1986.
- [115] M. Punk, D. Chowdhury, and S. Sachdev, “Topological excitations and the dynamic structure factor of spin liquids on the kagome lattice,” *Nature Physics*, vol. 10, p. 289, 2014.
- [116] F. Pollmann, P. Fulde, and K. Shtengel, “Kinetic ferromagnetism on a kagome lattice,” *Physical Review Letters*, vol. 100, p. 136404, 2008.
- [117] S. Yu and J. Li, “Chiral superconducting phase and chiral spin-density-wave phase in a Hubbard model on the kagome lattice,” *Physical Review B*, vol. 85, p. 144402, 2012.
- [118] Y. Liu, V. C. Kravtsoc, D. A. Beauchamp, J. F. Eubank, and M. Eddaoudi, “4-connected metal-organic assemblies mediated via heterochelation and bridging of single metal ions: kagome lattice and the M<sub>6</sub>L<sub>12</sub> octahedron,” *Journal of the American Chemical Society*, vol. 127, p. 7266, 2005.
- [119] E. A. Nytko, J. S. Helton, P. Müller, and D. G. Nocera, “A structurally perfect S = 1/2 metal-organic hybrid kagome antiferromagnet,” *Journal of the American Chemical Society*, vol. 130, p. 2922, 2008.
- [120] C. Vaz, V. E. Henrich, C. H. Ann, and E. I. Altman, “Growth and characterization of thin epitaxial Co<sub>3</sub>O<sub>4</sub> (111) films,” *Journal of Crystal Growth*, vol. 311, p. 2648, 2009.

- [121] A. Yang, Z. Chen, X. Zuo, J. Kirkland, C. Vittoria, and V. G. Harris, “Cation-disorder-enhanced magnetization in pulsed-laser-deposition  $\text{CuFe}_2\text{O}_4$  films,” *Applied Physics Letters*, vol. 86, p. 252510, 2005.
- [122] J. X. Ma, D. Mazumdar, G. Kim, H. Sato, N. Z. Bao, and A. Gupta, “A robust approach for the growth of epitaxial spinel ferrite films,” *Journal of Applied Physics*, vol. 108, p. 063917, 2010.
- [123] S. Matzen, J.-B. Moussy, R. Mattana, K. Bouzehouane, C. Deranlot, F. Petroff, J. C. Cezar, M.-A. Arrio, P. Sainctavit, C. Gatel, B. Warot-Fonrose, and Y. Zheng, “Epitaxial growth and ferrimagnetic behavior of  $\text{MnFe}_2\text{O}_4$  (111) ultrathin layers for room-temperature spin filtering,” *Physical Review B*, vol. 83, p. 184402, 2011.
- [124] U. Lüders, M. Bibes, J. Bobo, M. Cantoni, R. Bertacco, and J. Fontcuberta, “Enhanced magnetic moment and conductive behavior in  $\text{NiFe}_2\text{O}_4$  spinel ultrathin films,” *Physical Review B*, vol. 71, p. 134419, 2005.
- [125] N. Menyuk, K. Dwight, and A. Wold, “Ferrimagnetic spiral configurations in cobalt chromite,” *Journal de Physique*, vol. 25, pp. 528–536, 1964.
- [126] Y. J. Choi, J. Okamoto, D. J. Huang, K. S. Chao, H. J. Lin, C. T. Chen, M. van Veenendaal, T. A. Kaplan, and S.-W. Cheong, “Thermally or magnetically induced polarization reversal in the multiferroic  $\text{CoCr}_2\text{O}_4$ ,” *Physical Review Letters*, vol. 102, p. 067601, 2009.
- [127] K. Tomiyasu, J. Fukunaga, and H. Suzuki, “Magnetic short-range order and reentrant-spin-glass-like behavior in  $\text{CoCr}_2\text{O}_4$  and  $\text{MnCr}_2\text{O}_4$  by means of neutron scattering and magnetization measurements,” *Physical Review B*, vol. 70, p. 214434, 2004.
- [128] Y. Yamasaki, S. Miyasaka, Y. Kaneko, J. P. He, T. Arima, and Y. Tokura, “Magnetic reversal of the ferroelectric polarization in a multiferroic spinel oxide,” *Physical Review Letters*, vol. 96, p. 207204, 2006.
- [129] K. Singh, A. Maignan, C. Simon, and C. Martin, “ $\text{FeCr}_2\text{O}_4$  and  $\text{CoCr}_2\text{O}_4$  spinels: Multiferroicity in the collinear magnetic state?” *Applied Physics Letters*, vol. 99, p. 172903, 2011.
- [130] T. A. Kaplan and N. Menyuk, “Spin ordering in three-dimensional crystals with strong competing exchange interactions,” *Philosophical Magazine*, vol. 87, pp. 3711–3785, 2007.
- [131] M. Kareev, S. Prosandeev, B. Gray, J. Liu, P. Ryan, A. Kareev, E. J. Moon, and J. Chakhalian, “Sub-monolayer nucleation and growth of complex oxides at high supersaturation and rapid flux modulation,” *Journal of Applied Physics*, vol. 109, p. 114303, 2011.
- [132] J. Moussy, “From epitaxial growth of ferrite thin films to spin-polarized tunnelling,” *Journal of Physics D: Applied Physics*, vol. 46, p. 143001, 2013.

- [133] C. D. Wagner, W. M. Riggs, L. E. Davis, J. F. Moulder, and G. E. Muilenberg, *Handbook of X-ray photoelectron spectroscopy*. Perkin-Elmer, Eden Prairie, 1979.
- [134] S. Lei, L. Liu, C. Wang, X. Shen, C. Wang, D. Guo, S. Zeng, B. Cheng, Y. Xiao, and L. Zhou, "A facile in situ reduction route for preparation of spinel  $\text{CoCr}_2\text{O}_4$  polycrystalline nanosheets and their magnetic properties," *CrystEngComm*, vol. 16, p. 277, 2014.
- [135] C. Kao, J. B. Hastings, E. D. Johnson, D. P. Siddons, G. C. Smith, and G. A. Prinz, "Magnetic-resonance exchange scattering at the iron LII and LIII edges," *Physical Review Letters*, vol. 65, p. 373, 1990.
- [136] D. R. Lee and S. K. Sinha, "X-ray resonant magnetic scattering from structurally and magnetically rough interfaces in multilayered systems. I. Specular reflectivity," *Physical Review B*, vol. 68, p. 224409, 2003.
- [137] D. Xiao, W. Zhu, Y. Ran, N. Nagaosa, and S. Okamoto, "Interface engineering of quantum Hall effects in digital transition metal oxide heterostructures," *Nature Communications*, vol. 2, p. 596, 2011.
- [138] M. Kargarian, A. Langair, and G. A. Fiete, "Unusual magnetic phases in the strong interaction limit of two dimensional topological band insulators in transition metal oxides," *Physical Review B*, vol. 86, p. 205124, 2012.
- [139] A. Rüegg, C. Mitra, A. A. Demkov, and G. A. Fiete, "Electronic structure of  $(\text{LaNiO}_3)_2/(\text{LaAlO}_3)_N$  heterostructures grown along [111]," *Physical Review B*, vol. 85, p. 245131, 2012.
- [140] N. Nakagawa, H. Y. Hwang, and D. A. Muller, "Why some interfaces cannot be sharp," *Nature Materials*, vol. 5, p. 204, 2006.
- [141] J. L. Blok, X. Wan, G. Koster, D. H. A. Blank, and G. Rijnders, "Epitaxial oxide growth on polar (111) surfaces," *Applied Physics Letters*, vol. 99, p. 151917, 2011.
- [142] X. Liu, M. Kareev, Y. Cao, J. Liu, S. Middey, D. Meyers, J. W. Freeland, and J. Chakhalian, "Electronic and magnetic properties of (111)-oriented  $\text{CoCr}_2\text{O}_4$  epitaxial thin films," *Applied Physics Letters*, vol. 105, p. 042401, 2014.
- [143] Y. Gao, Y. J. Kim, S. A. Chambers, and G. Bai, "Synthesis of epitaxial films of  $\text{Fe}_3\text{O}_4$  and  $\alpha\text{-Fe}_2\text{O}_3$  with various low-index orientations by oxygen-plasma-assisted molecular beam epitaxy," *Journal of Vacuum Science and Technology A*, vol. 15, p. 332, 1997.
- [144] J. G. Dillard, C. V. Schenck, and M. H. Koppelman, "Surface chemistry of cobalt in calcined cobalt-kaolinite materials," *Clays and Clay Minerals*, vol. 31, p. 69, 1983.
- [145] D. Kumar, P. Mohanty, V. P. Singh, J. K. Galivarapu, A. Banerjee, V. Ganesan, and C. Rath, "Tuning of magnetic transition temperatures in nanoparticles of  $\text{CoCr}_2\text{O}_4$  multiferroic by B-site mixing," *Materials Research Bulletin*, vol. 54, p. 78, 2014.

- [146] Y. Okamoto, H. Nakano, T. Imanaka, and S. Teranishi, “X-Ray Photoelectron Spectroscopic Studies of Catalysts,” *Bulletin of the Chemical Society of Japan*, vol. 48, p. 1163, 1975.
- [147] A. E. Bocquet and A. Fujimori, “Predictions for core-level X-ray photoemission spectra of divalent and trivalent 3d transition-metal compounds,” *Journal of Electron Spectroscopy and Related Phenomena*, vol. 82, p. 87, 1996.
- [148] J. A. Rotole and P. M. A. Sherwood, “Corrundum ( $\alpha$ -Al<sub>2</sub>O<sub>3</sub>) by XPS,” *Surface Science Spectra*, vol. 5, p. 11, 1998.
- [149] A. P. Ramirez, “Strongly geometrically frustrated magnets,” *Annual Review of Materials Science*, vol. 24, pp. 453–480, 1994.
- [150] L. Balents, “Spin liquids in frustrated magnets,” *Nature*, vol. 464, pp. 199–208, 2010.
- [151] B. J. Kirby, P. A. Kuenzle, B. B. Maranville, N. F. Berk, J. Krycka, F. Heinrich, and C. F. Majkrzak, “Phase-sensitive specular neutron reflectometry for imaging the nanometer scale composition depth profile of thin-film materials,” *Current Opinion in Colloid and Interface Science*, vol. 17, p. 44, 2012.
- [152] D. H. Lyons, T. A. Kaplan, K. Dwight, and N. Menyuk, “Classical theory of the ground spin-state in cubic spinels,” *Physical Review*, vol. 126, p. 540, 1962.
- [153] B. M. Altshuler, S. A. & Kozyrev, *Electron Paramagnetic Resonance in Compounds of Transition Elements*. Wiley, New York, 1974, 1974.
- [154] K. Binder and A. P. Young, “Spin glasses: experimental facts, theoretical concepts and open questions,” *Reviews of Modern Physics*, vol. 58, pp. 801–976, 1986.
- [155] C. Ederer and M. Komelj, “Magnetic coupling in CoCr<sub>2</sub>O<sub>4</sub> and MnCr<sub>2</sub>O<sub>4</sub>: An LSDA + U study,” *Physical Review B*, vol. 76, p. 064409, 2007.
- [156] X. Hu, Z. Zhong, and G. A. Fiete, “First principles prediction of topological phases in thin films of pyrochlore iridates,” *Scientific Reports*, vol. 5, p. 11072, 2015.
- [157] B. Yang and N. Nagaosa, “Emergent topological phenomena in thin films of pyrochlore iridates,” *Physical Review Letters*, vol. 112, p. 246402, 2014.
- [158] T. Fujita, Y. Kozuka, M. Uchida, A. Tsukazaki, T. Arima, and M. Kawasaki, “Odd-parity magnetoresistance in pyrochlore iridate thin films with broken time-reversal symmetry,” *Scientific Reports*, vol. 5, p. 9711, 2015.
- [159] L. Bovo, X. Moya, D. Prabhakaran, Y. Soh, A. Boothroyd, N. Mathur, G. Aeppli, and S. Bramwell, “Restoration of the third law in spin ice thin films,” *Nature Communications*, vol. 5, p. 3439, 2014.
- [160] T. Fujita, M. Uchida, Y. Kozuka, W. Sano, A. Tsukazaki, T. Arima, and M. Kawasaki, “All-in-all-out magnetic domain wall conduction in a pyrochlore iridate heterointerface,” *Physical Review B*, vol. 93, p. 064419, 2016.

- [161] J. Afonso and V. Pardo, “*Ab initio* study of nontrivial topological phases in corundum-structured  $(M_2O_3)/(Al_2O_3)_5$  multilayers,” *Physical Review B*, vol. 92, p. 235102, 2015.
- [162] G. Herranz, F. Sánchez, N. Dix, M. Scigaj, and J. Fontcuberta, “High mobility conduction at (110) and (111)  $LaAlO_3/SrTiO_3$  interfaces,” *Scientific Reports*, vol. 2, p. 758, 2012.
- [163] S. Takei, B. Fregoso, V. Galitski, and S. Sarma, “Topological superconductivity and Majorana fermions in hybrid structures involving cuprate high-Tc superconductors,” *Physical Review B*, vol. 87, p. 014504, 2013.